HIGHER ORDER NUMERICAL SCHEMES FOR PROPAGATION OF WIND WAVE SPECTRA

by

Younsang Won

Dissertation submitted to the Faculty of the

Virginia Polytechnic Institute and State University

in partial fulfillment of the requirements for the degree of

DOCTOR OF PHILOSOPHY

in

Aerospace Engineering

APPROVED:

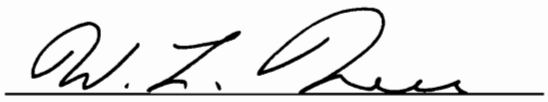

W. L. Neu, Chairman

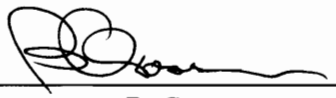

B. Grossman

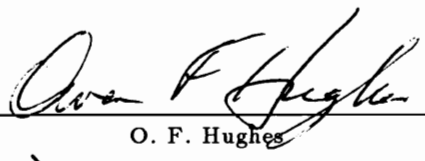

O. F. Hughes

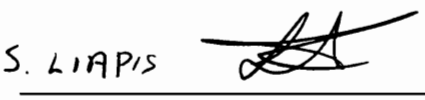

S. I. Liapis

J. A. Schetz

July, 1991

Blacksburg, Virginia

HIGHER ORDER NUMERICAL SCHEMES FOR PROPAGATION OF WIND WAVE SPECTRA

by

Younsang Won

Committee Chairman: Wayne L. Neu

Aerospace Engineering

(ABSTRACT)

Spectral wind wave models seek to solve a four-dimensional energy (or action) balance equation for values of the spectrum discretized in frequency and direction of propagation at fixed positions in space. When modeling an ocean area of any appreciable size, computational time and storage capacity limit resolution to relatively coarse grids in all four dimensions. Propagation schemes used in these models, typically the 1st order upwind scheme, encounter difficulty arising from the poor directional resolution (typically 30 degrees) in regions of varying depth and current where wave energy is refracted and concentrated into a small number of directional bins. Since the widely used 1st order upwind scheme is not appropriate for such a rapid bin to bin variation, higher order numerical schemes are investigated to identify one which will produce better results for this wind wave propagation problem. After evaluating the characteristics and performance of the 2nd-order upwind scheme, Lax-Wendroff scheme, and modified Lax-Wendroff scheme suggested by Gadd, for both steady and transient cases, a new propagation scheme is proposed using a time-splitting method and a limiter which combines the modified Lax-Wendroff scheme with the 1st order upwind scheme. For varying depth and current fields, it is shown that the new scheme gives results superior to the ordinary 1st order upwind scheme without any increase of storage capacity at an increased cost in computing time which is minor to the overall wind wave model.

ACKNOWLEDGEMENTS

I am very pleased to have this opportunity to express my gratitude to all the people around me.

My first thanks go to Dr. Wayne L. Neu, who introduced me to the field of wind wave modeling and has taken care of me as my advisor. His insightful comments and invaluable guidance have brought this dissertation into existence. I would also like to thank my committee members, Dr. Bernard Grossman, Dr. Owen F. Hughes, Dr. Stergaos I. Liapis and Dr. Joseph A. Schetz. I am greatly indebted to Dr. Bernard Grossman for his excellent teaching on numerical methods as well as for his precise and knowledgeable advice.

I always thank Professor Jong-Heul Hwang and Professor Hang-Shoon Choi at the Seoul National University for their continuous concern about me. The research experience at the Hyundai Maritime Research Institute was of great help in pursuing my Ph.D. degree and I am very grateful to the staff of the HMRI.

My deepest gratitude is for my parents who love me so much and sacrifice themselves for their children. I am happy to thank my brother and sisters for their support of me. For my lovely wife, Hyesook, I cannot express my thanks too much. She has always encouraged me and prayed for me. Our life in Blacksburg has been so precious thanks to the families of Dr. Young-Seock Shin, Dr. Joon-Kyung Kim, Dr. Bo-Hyung Cho, Dr. Dong-Sam Ha and many other good friends.

Thanks be to God.

Finally, I would like to thank the National Science Foundation and Nova University for their financial support for this work.

TABLE OF CONTENTS

NOMENCLATURE

$A(\omega, \theta; \mathbf{x}, t)$	spectral action density function in (ω, θ) space
a	wave amplitude
$\mathbf{c}$	phase velocity
$\mathbf{c_o}$	phase velocity measured in a moving coordinate
$\mathbf{c_g}$	group velocity
$\mathbf{c_{g_o}}$	group velocity measured in a moving coordinate
E	total wave energy per unit area
$F(\omega, \theta)$	spectral energy density function in (ω, θ) space
f	frequency in Hz
G	amplification factor
g	acceleration of gravity
H_s	significant wave height
h	water depth
k	wave number
$\mathbf{k}$	wave number vector
$\dot{\mathbf{k}}$	group velocity in wave number space ($\mathbf{k}$)
$L(\Delta t)$	differencing operator
l	wave length of a Fourier component
$M(\mathbf{k})$	spectral energy density function in wave number space ($\mathbf{k}$)
$N(\mathbf{k}; \mathbf{x}, t)$	spectral action density function in wave number space ($\mathbf{k}$)
$P(\mathbf{k}, \omega)$	spectral energy density function in $(\mathbf{k}, \omega)$ space
q	$= \mathbf{U} \cdot \mathbf{k}/k$
r	ratio between two consecutive gradients of A
S	source function term

s	$= \|2r\|/(1+r^2)$, limiter
$\mathbf{U}$	current velocity
$\mathbf{x}$	spatial vector
$\dot{\mathbf{x}}$	$= \mathbf{c_g}$, group velocity in a spatial coordinate ($\mathbf{x}$)
β	$= 2\pi\Delta x/l_x$
ε	phase lag
ϕ	phase lag of amplification factor, G
γ	$= 2\pi\Delta y/l_y$
ξ	variation of a medium
κ	parameter for a modified Lax-Wendroff scheme
λ	Courant number in x dimension
μ	Courant number in y dimension
θ	direction of propagation
$\dot{\theta}$	rate of change of the direction of propagation, θ
ρ	water density
$\psi(\mathbf{x},t)$	phase function
ω	wave frequency in rad/sec
$\dot{\omega}$	rate of change of the absolute frequency, ω
ω_o	intrinsic frequency
$\eta(\mathbf{x},t)$	free surface elevation
Δt	time increment
Δx	spatial increment
$\nabla_{\mathbf{k}}$	partial derivative in wave number space ($\mathbf{k}$)
$\nabla_{\mathbf{x}}$	partial derivative in a spatial coordinate ($\mathbf{x}$)
$\frac{\partial}{\partial t}$	partial derivative in time
$\frac{d}{dt}$	total derivative in a spatial coordinate ($\mathbf{x}$)
$\frac{D}{Dt}$	total derivative in four-dimensional space ($\mathbf{x},\mathbf{k}$)

LIST OF FIGURES

LIST OF TABLES

1. INTRODUCTION

The ocean is always moving. Its movement on the surface can be classified into several groups, depending on the source of its motion. In a large scale, the rotation of the earth (the Coriolis force) induces geostrophic flows and the interaction force between the earth and the moon gives rise to tidal flows. The most familiar motion of the ocean is a rather short wind-generated gravity wave (in short, the wind wave) which is excited by the wind and of which restoring force is obtained from gravity. In the following, the wind wave will be implied when ocean wave is referred to, and a current will represent the large scale motion such as the geostrophic flow and the tide.

The ocean wave is basically one type of energy propagation at the interface between two different media (air and water), and its information plays an important role in several fields of application. Since the ocean wave transports a significant amount of energy, it is often very hazardous to offshore and coastal structures. Knowledge of the ocean wave environment is therefore essential information in designing those structures. Another application is for underwater acoustic transmission. The ocean wave, a free surface disturbance, creates noise for the transmission at the surface zone and the information of the ocean wave is used to determine its noise level. Under the surface of the ocean waves, active processes of exchanging momentum, heat and gases are taking place in the "upper ocean". These processes are one of the most important factors to affect the world-wide climate. In modeling the upper ocean, the distribution of ocean waves should be given as the boundary condition.

Extensive studies have endeavored to understand the physics of the wind wave and to develop numerical models for wave forecasting. Important progress has

been made in recent years, such as the resonant turbulent air-pressure interaction (Phillips, 1957; Miles, 1957) and the resonant non-linear wave-wave interaction (Hasselmann, 1962). The action conservation equation (Whitham, 1965; Bretherton and Garrett, 1969) provides a general governing equation of wave propagation in a varying depth and/or current field. Numerical modeling of the wind wave problem has progressed rapidly in the past decade despite a less than complete knowledge of the physics. Although compared to the energy source and dissipation terms of the wind wave model, the propagation mechanism of the wind wave models are very well established. Most operating models, however, use a simple propagation scheme (the 1st order upwind scheme) and do not include the effects of varying depth and current. The purpose of this paper is to develop a propagation module of a wind wave model which can take into account the effects of varying depth and current, at the same time implementing higher order numerical schemes.

Most numerical wind wave models use discrete frequency and direction bands to represent the ocean wave spectrum. They are faced with the problem that when using the desired degree of spectral resolution, in a model of any appreciable size (i.e. number of grid points), a very large number of values is required to define the wave spectrum field. This implies enormous storage requirements and prohibitive computation time to process each of these values. The resolution problem, particularly in the directional bands, is magnified by the extension of these models into regions of varying depth and current. Trouble arises in the propagation module of these models. They seek to propagate a directional energy (or action) spectrum across a fixed grid with reasonable accuracy. In these situations, the commonly used 1st order upwind differencing scheme is simply not adequate with the coarse directional resolution of 15° or 30° which must be used in these models.

One of the early numerical solutions of this type for depth refraction is given by Karlsson (1969). Golding (1983) incorporated depth refraction into an operational wave model. He used the modified Lax-Wendroff scheme for propagation through (x, y) space but used the conservative 1st order upwind scheme (explained later) for the refraction (θ direction) term. One of the early numerical solutions to include current as well as depth refraction is that of Sakai et al. (1983). They used 1st order upwind schemes in all directions. Recently, Tolman (1989) has incorporated depth and current refraction in a wind wave model using a Crank-Nicolson scheme in (ω, θ) space and a combination of Crank-Nicolson and 1st order upwind schemes in (x, y) space. In this paper, we investigate the behavior of several higher order numerical schemes incorporating depth and current refraction with an objective of identifying and developing a scheme which will perform with reasonable accuracy at a 15° or 30° directional resolution.

With the concept of a slowly varying wave train, the action conservation equation is explained in chapter 2. It governs the wave energy propagation in varying depth and current. The characteristics of several numerical schemes are investigated in chapter 3 for one and two-dimensional linear advection equations. Tests for square wave and unit pulse propagation are presented. In chapter 4, numerical solutions incorporating depth and current refraction are compared with an analytic solution for steady state cases. After evaluating the performance of the numerical schemes, a new propagation scheme is proposed in chapter 5 using a time splitting method and a continuous limiter. The new scheme is applied to the previous test cases for comparison and also applied to an example of an elliptic shoal in which case experimental data are available. In chapter 6, the new propagation module is combined with a relatively simple wind wave model, and simulation of wind wave generation is demonstrated at the Bight of Abaco in the Bahamas. Conclusions are presented in chapter 7.

2. GOVERNING EQUATIONS

For a linear gravity wave, the propagation of wave energy can be described by an advection of the wave energy or action. In a moving medium such as a current, the wave energy is no longer conserved but the wave action is still conserved along a ray (a spatial path of energy propagation). The action balance equation is therefore chosen as the governing equation for wave propagation. Assuming a slowly varying wave train, various expressions of this equation are presented in terms of a total action or a spectral density. The concept of four dimensional propagation is introduced with the derivation of the corresponding propagation velocities using a ray theory.

2.1 Single Harmonic Wave

Ocean waves can be modeled by a sum of simple harmonic waves with different frequencies and different amplitudes, travelling in different directions. In this section a single harmonic component, a plane-propagating wave, is considered.

$$\eta(\mathbf{x},t) = a\cos(\mathbf{k}\cdot\mathbf{x} - \omega t + \varepsilon) \tag{2.1}$$

where η represents the surface elevation as a function of the spatial coordinate ($\mathbf{x}$) and time (t). This single component follows a harmonic motion with an amplitude of a and an angular frequency of ω (assuming positive ω). Its period is $2\pi/\omega$ and it propagates in the direction of $\mathbf{k}$ (wave number vector) with the wave length of $2\pi/k$ where k (wave number) is the magnitude of $\mathbf{k}$. The argument of the cosine function in (2.1) represents the phase of the wave, such as crest or trough. It is referred to as a phase function with a phase lag of ε.

$$\psi(\mathbf{x},t) = \mathbf{k}\cdot\mathbf{x} - \omega t + \varepsilon \tag{2.2}$$

There are two kinds of propagation velocities; a phase velocity and a group velocity. The phase velocity is the celerity of the wave shape (e.g., crest, trough), which can be calculated by taking a time derivative of a constant phase function ($\psi = constant$). The phase velocity, then, becomes

$$\mathbf{c} = \frac{\omega}{k}\frac{\mathbf{k}}{k} \tag{2.3}$$

The group velocity represents the wave energy propagation velocity and has the following relation (Newman, 1977; Mei, 1983):

$$\mathbf{c_g} = \nabla_{\mathbf{k}}\omega \tag{2.4}$$

where $\nabla_{\mathbf{k}}$ denotes the partial derivative in wave number space ($\mathbf{k}$).

For linear gravity waves, the two velocities are related by

$$\mathbf{c_g} = \frac{1}{2}\left(1 + \frac{2kh}{\sinh 2kh}\right)\mathbf{c} \tag{2.5}$$

where h is the water depth. From this equation, it can be observed that the group velocity is just a half of the phase velocity in deep water ($kh > \pi$) and they become equivalent in shallow water ($kh < \pi/10$).

2.2 Dispersion Relation

In the absence of currents, the free surface boundary condition for linear gravity waves yields the following relation between ω and k called the dispersion relation.

$$\omega^2 = kg \tanh kh \tag{2.6}$$

where g is the acceleration of gravity.

According to this equation, waves with different frequencies have different wave numbers. For example, consider a deep water case. A lower frequency wave has

a smaller wave number, which in turn yields a faster group velocity. That means, the lower frequency a wave has, the faster it propagates in deep water. As a result, a group of ocean waves with different frequencies become "dispersive" due to their different propagation velocities. Thus, the ocean wave is a dispersive wave.

In a moving medium such as a current, the dispersion relation (2.6) should be based on a relative frequency which is measured in a reference of the moving medium. The relative frequency and the absolute frequency (ω) are related by the Doppler shift. The complete dispersion relation for a moving medium becomes

$$\omega = \omega_o + \mathbf{k} \cdot \mathbf{U} \tag{2.7}$$

$$\omega_o^2 = kg \tanh kh \tag{2.8}$$

where ω_o is the relative (or intrinsic) frequency and $\mathbf{U}$ is the velocity vector of the moving medium. These two equations are usually solved simultaneously for the unknown variables of ω_o and k. An iteration procedure for finding these roots requires a good choice of initial guess value which is crucial in converging to the correct roots. Details of solving the equations are described in the Appendix.

Note that the Doppler shift equation (2.7) is based on the moving medium itself, not on the moving source and/or observer. Therefore, the absolute frequency, ω, which is measured in a fixed coordinate system, remains the same. When the wave propagates in a favorable direction to the moving medium ($\mathbf{k} \cdot \mathbf{U} > 0$), the relative frequency decreases (2.7), resulting in a stretching of the wave length, a decrease of the amplitude, and a faster propagation speed than in a resting medium. For the waves propagating upstream ($\mathbf{k} \cdot \mathbf{U} < 0$), the opposite is true.

The phase velocity and group velocity for the moving medium can be written as follows:

$$\mathbf{c} = \frac{\omega}{k}\frac{\mathbf{k}}{k} = \frac{\omega_o}{k}\frac{\mathbf{k}}{k} + \mathbf{U} = \mathbf{c_o} + \mathbf{U} \tag{2.9}$$

$$\mathbf{c_g} = \nabla_{\mathbf{k}}\omega = \nabla_{\mathbf{k}}\omega_o + \mathbf{U} = \mathbf{c_{g_o}} + \mathbf{U} \tag{2.10}$$

where the subscript "o" denotes the quantity measured in a moving coordinate system.

2.3 Kinematic Equations

Another important relation between the wave number and the frequency can be derived from the phase function (2.2). Note that this relation is kinematic while the dispersion relation (2.6) is obtained from the dynamic free surface condition. Using the phase function, the wave number and frequency can be written as

$$\mathbf{k} = \nabla_{\mathbf{x}}\psi(\mathbf{x}, t) \tag{2.11}$$

$$\omega = -\frac{\partial}{\partial t}\psi(\mathbf{x}, t) \tag{2.12}$$

where $\nabla_{\mathbf{x}}$ denotes the partial derivative in spatial coordinate ($\mathbf{x}$) and $\frac{\partial}{\partial t}$ is the partial derivative in time.

It can be seen that the wave number vector is irrotational in the spatial coordinate since $\nabla_{\mathbf{x}} \times \mathbf{k} = 0$. Two equations, (2.11) and (2.12), can be combined into one as follows by taking the partial derivatives in the alternative dimensions.

$$\frac{\partial \mathbf{k}}{\partial t} + \nabla_{\mathbf{x}}\omega = 0 \tag{2.13}$$

This equation represents the balance between the rate of change of the number of waves in a unit length and the spatial flux of the frequency of the waves. In other words, the number and the frequency of waves are balanced so that no waves can be created or destroyed. The kinematic equation (2.13) is called the conservation equation of wave crests.

Next, consider a little more general expression of a wave train rather than a single harmonic wave (2.1).

$$\eta(\mathbf{x}, t) = a(\mathbf{x}, t) \cos(\mathbf{k} \cdot \mathbf{x} - \omega t + \varepsilon) \tag{2.14}$$

The amplitude of wave, $a(\mathbf{x}, t)$, is no longer constant but is varying very slowly in space and time, compared to the variation of the phase function (2.2) itself. In this case, the characteristic parameters of a local space and time can be found under the linearizing assumption that the amplitude $a(\mathbf{x}, t)$ remains constant as in the single harmonic wave. In a large scale, however, the characteristic parameters should include the variation of the amplitude which is determined from the conservation of energy. This wave (2.14) is called a slowly varying wave train or a nearly-plane wave. Many important results in wave theory (e.g., ray theory, action conservation equation) are based on the assumption of the slowly varying wave train. Note that we are still working within the framework of linear wave theory.

Now, we find the kinematic equations of propagation velocities in the slowly varying wave train. Since wind wave models are concerned with wave energy propagation, the group velocity will be implied when the propagation velocity is referred to in the following. For the slowly varying wave train, the absolute wave frequency can be written as

$$\omega = \omega(\mathbf{k}, \xi; \mathbf{x}, t) \tag{2.15}$$

where ξ represents the variation of the medium itself (e.g., varying water depth and moving medium) and the last two variables $(\mathbf{x}, t)$ account for the slow variation.

By using the conservation equation of wave crests (2.13), the following propagation velocities can be obtained (LeBlond and Mysak, 1978):

$$\dot{\mathbf{x}} = \frac{d\mathbf{x}}{dt} = \mathbf{c_g} = \nabla_{\mathbf{k}} \omega \tag{2.16}$$

$$\dot{\mathbf{k}} = \frac{d\mathbf{k}}{dt} = -\frac{\partial\omega}{\partial\xi}\nabla_{\mathbf{x}}\xi \tag{2.17}$$

$$\dot{\omega} = \frac{d\omega}{dt} = \frac{\partial\omega}{\partial\xi}\frac{\partial\xi}{\partial t} \tag{2.18}$$

where $\dot{\mathbf{x}}$ represents the energy propagation velocity in a spatial coordinate ($\mathbf{x}$), which is identical to the group velocity, $\mathbf{c_g}$ (2.10), defined in the previous section. Thus, $\frac{d}{dt}$ denotes the total derivative along a spatial path of the energy propagation which is called a ray. It is defined as

$$\frac{d}{dt} \equiv \frac{\partial}{\partial t} + \dot{\mathbf{x}} \cdot \nabla_{\mathbf{x}} \tag{2.19}$$

Equations (2.17) and (2.18) represent the rate of change's of $\mathbf{k}$ and ω, respectively, along the ray. These terms may be thought of as the propagation velocities in their own domains (i.e., the wave number space and the wave frequency space), if $\mathbf{k}$ and ω are considered to be other dimensions of the problem. This argument is also applied to the case of θ (direction of propagation) in the following.

In a moving medium and varying water depth, the parameter ξ can be represented by $\mathbf{U}(\mathbf{x}, t)$ and $h(\mathbf{x}, t)$. Substituting the Doppler shift equation (2.7) for the absolute frequency in the above equations, we have in tensor notation

$$\dot{x_i} = \frac{\partial\omega_o}{\partial k_i} + U_i \tag{2.20}$$

$$\dot{k_i} = -\frac{\partial\omega_o}{\partial h}\frac{\partial h}{\partial x_i} - k_j\frac{\partial U_j}{\partial x_i} \tag{2.21}$$

$$\dot{\omega} = \frac{\partial\omega_o}{\partial h}\frac{\partial h}{\partial t} + k_j\frac{\partial U_j}{\partial t} \tag{2.22}$$

In wind wave models, more often used is the rate of change of the direction of propagation ($\dot{\theta}$) which will be called the directional propagation velocity as discussed above. It can be easily derived by transforming the rectangular coordinates (k_1, k_2)

to the polar coordinates (k, θ). Using $k^2 = k_1^2 + k_2^2$ and $\theta = \tan^{-1}(k_2/k_1)$, we can obtain

$$\dot{k} = \frac{dk}{dt} = \dot{k_1} \cos\theta + \dot{k_2} \sin\theta \tag{2.23}$$

$$\dot{\theta} = \frac{d\theta}{dt} = \frac{1}{k}(-\dot{k_1} \sin\theta + \dot{k_2} \cos\theta) \tag{2.24}$$

From the dispersion relation for a moving medium (2.8),

$$\frac{\partial \omega_o}{\partial h} = \frac{k\omega_o}{\sinh 2kh} \tag{2.25}$$

Hence, the directional propagation velocity can be written as

$$\begin{aligned} \dot{\theta} = & \frac{\omega_o}{\sinh 2kh}\left(\frac{\partial h}{\partial x_1}\sin\theta - \frac{\partial h}{\partial x_2}\cos\theta\right) \\ & + \left(\frac{\partial U_1}{\partial x_1} - \frac{\partial U_2}{\partial x_2}\right)\sin\theta\cos\theta + \frac{\partial U_2}{\partial x_1}\sin^2\theta - \frac{\partial U_1}{\partial x_2}\cos^2\theta \end{aligned} \tag{2.26}$$

2.4 Action Balance Equation

For a slowly varying wave train, Bretherton and Garrett (1969) showed that the wave energy is no longer conserved in a moving medium but the wave action is still conserved. The action is a well-defined concept in classical physics. It is the quantity of the energy divided by the intrinsic (or relative) frequency, ω_o (2.7). The total wave energy per unit area in a local space and time can be calculated under the assumption of constant wave amplitude, which yields

$$E = \frac{1}{2}\rho g a^2 \tag{2.27}$$

where ρ is the water density.

In a large scale, the total wave energy, E, becomes a function of space and time, i.e., $E(\mathbf{x}, t)$, and the action conservation equation is

$$\frac{\partial}{\partial t}\left(\frac{E}{\omega_o}\right) + \nabla_{\mathbf{x}} \cdot \left(\dot{\mathbf{x}}\frac{E}{\omega_o}\right) = 0 \tag{2.28}$$

This equation becomes equivalent to the energy conservation equation for a resting medium in which the intrinsic frequency has a constant value of the absolute frequency.

Most wind wave models are based on the spectral energy (or action) density rather than the total energy, E. The spectral density function can be obtained by the Fourier transform of the covariance of the surface elevations (Phillips, 1957). The local space and time domains $(\mathbf{x}, t)$ are transformed into the wave number and frequency domains $(\mathbf{k}, \omega)$. Thus, the spectral density function in the local scale can be expressed in

$$P = P(\mathbf{k}, \omega) \tag{2.29}$$

For linear gravity waves, there exists a relationship between the wave number and frequency. It is the dispersion relation (2.8) as described earlier. In the wind wave models we assume linear waves, and then the spectral density function can be described by a pair of variables instead of three variables as in (2.29). In the following, two pairs are used; the wave number vector $(\mathbf{k})$, or the wave frequency and direction (ω, θ). The spectral energy density functions are related to the total wave energy by

$$E = \rho g \int_{\omega} \int_{\mathbf{k}} P(\mathbf{k}, \omega)\, d\mathbf{k} d\omega = \rho g \int_{\mathbf{k}} M(\mathbf{k})\, d\mathbf{k} = \rho g \int_{\theta} \int_{\omega} F(\omega, \theta)\, d\omega d\theta \tag{2.30}$$

where $M(\mathbf{k})$ is the spectral energy density function in wave number space, and $F(\omega, \theta)$ is the same expressed in the wave frequency and direction space. Using the Jacobian, these two spectral density functions can be related as follows:

$$M(\mathbf{k}) = \frac{1}{k} \frac{\partial \omega}{\partial k} F(\omega, \theta) \tag{2.31}$$

As in the previous cases, the spectral density function also becomes a function of space and time in a large scale. The corresponding action conservation equation for the spectral density functions of $M(\mathbf{k})$ and $F(\omega, \theta)$ become

$$\frac{\partial N}{\partial t} + \nabla_{\mathbf{x}} \cdot (\dot{\mathbf{x}} N) + \nabla_{\mathbf{k}} \cdot (\dot{\mathbf{k}} N) = 0 \tag{2.32}$$

$$\frac{\partial A}{\partial t} + \nabla_{\mathbf{x}} \cdot (\dot{\mathbf{x}} A) + \frac{\partial}{\partial \omega}(\dot{\omega} A) + \frac{\partial}{\partial \theta}(\dot{\theta} A) = 0 \tag{2.33}$$

where N and A represent the spectral action density functions defined by $N(\mathbf{k}; \mathbf{x}, t)$ $= M(\mathbf{k}; \mathbf{x}, t)/\omega_o$ and $A(\omega, \theta; \mathbf{x}, t) = F(\omega, \theta; \mathbf{x}, t)/\omega_o$. The relation of (2.31) between the two spectral energy density functions, M and F, still holds for the corresponding action density functions, N and A.

If we consider this problem as the propagation of the spectral action density (N or A) through the four dimensional space, $(\mathbf{x}, \mathbf{k})$ or $(\mathbf{x}, \omega, \theta)$, the action conservation equation (2.32) can be expressed as

$$\frac{\partial N}{\partial t} + \nabla \cdot (\mathbf{v} N) = 0 \tag{2.34}$$

where $\nabla = (\frac{\partial}{\partial x_1}, \frac{\partial}{\partial x_2}, \frac{\partial}{\partial k_1}, \frac{\partial}{\partial k_2})$ and $\mathbf{v} = (\dot{x_1}, \dot{x_2}, \dot{k_1}, \dot{k_2})$.

Similarly, equation (2.33) becomes

$$\frac{\partial A}{\partial t} + \nabla \cdot (\mathbf{v} A) = 0 \tag{2.35}$$

where, in this case, $\nabla = (\frac{\partial}{\partial x_1}, \frac{\partial}{\partial x_2}, \frac{\partial}{\partial \omega}, \frac{\partial}{\partial \theta})$ and $\mathbf{v} = (\dot{x_1}, \dot{x_2}, \dot{\omega}, \dot{\theta})$.

A more useful form of the action conservation equation can be obtained in the wave number space by using the conservation equation of wave crests (2.13).

$$\frac{DN}{DT} = (\frac{\partial}{\partial t} + \dot{\mathbf{x}} \cdot \nabla_{\mathbf{x}} + \dot{\mathbf{k}} \cdot \nabla_{\mathbf{k}}) N = 0 \tag{2.36}$$

where $\frac{D}{DT}$ denotes the total derivative along a ray in the four dimensional space $(\mathbf{x}, \mathbf{k})$. Note its difference from equation (2.19) in which only the spatial dimension $(\mathbf{x})$ is involved.

For a wind wave model, not only the propagation of wave energy but also its generation and dissipation should be included. These contributions are represented here by a source function, S, which is basically composed of a wind input term, a non-linear wave-wave interaction term, and a dissipation term. The action balance equation for wind wave models can be established by adding the source function term divided by the intrinsic frequency at the right hand side of the action conservation equation. The source function term should be expressed in the same dimensions with the left hand side terms. For example, the action balance equation in the frequency and directional dimensions (2.33) becomes

$$\frac{\partial A}{\partial t} + \nabla_{\mathbf{x}} \cdot (\dot{\mathbf{x}} A) + \frac{\partial}{\partial \omega}(\dot{\omega} A) + \frac{\partial}{\partial \theta}(\dot{\theta} A) = \frac{S}{\omega_o} \tag{2.37}$$

where $A = A(\omega, \theta; \mathbf{x}, t)$ and $S = S(\omega, \theta; \mathbf{x}, t)$.

During the following investigation of the propagation itself, the source function term will be set to zero.

3. NUMERICAL SCHEMES FOR LINEAR ADVECTION

This chapter is devoted to investigating the characteristics of some explicit numerical schemes for a linear advection equation. Since our concern is developing the propagation module of a wind wave model, the source function term in the action balance equation is taken to be zero. An assumption that the propagation velocity, $\mathbf{v}$, is constant makes the equation linear, which is true only if water depth is constant and there is no current. Nevertheless, the following linear advection equation can provide local behavior of numerical schemes even for a varying depth and current field case.

$$\frac{\partial A}{\partial t} + \mathbf{v} \cdot \nabla A = 0 \tag{3.1}$$

The 1st order upwind scheme is investigated with higher order numerical schemes such as 2nd order upwind scheme, a Lax-Wendroff scheme (Lax and Wendroff, 1960), and a modified Lax-Wendroff scheme (Gadd, 1978b; Gadd, 1980). The Lax-Wendroff schemes are commonly used in a meteorology field. For the upwind schemes, the Euler Explicit time integration is used.

3.1 One-Dimensional Linear Advection

3.1.1 The 1st Order Upwind Scheme

Most operating wind wave models use this simplest scheme.

$$\begin{aligned} \frac{A_j^{n+1} - A_j^n}{\Delta t} &= -v \frac{A_j^n - A_{j-1}^n}{\Delta x} \qquad for\ v \geq 0 \\ &= -v \frac{A_{j+1}^n - A_j^n}{\Delta x} \qquad for\ v < 0 \end{aligned} \tag{3.2}$$

Since both cases give identical characteristics, only the positive v case will be considered. The value of A at the j-th grid point, then, can be updated by

$$A_j^{n+1} = A_j^n - \lambda (A_j^n - A_{j-1}^n) \tag{3.3}$$

where $\lambda = v\Delta t/\Delta x$, is called the Courant number.

Stability and phase lag of numerical schemes can be determined by the von Neumann stability analysis (e.g., Anderson et al., 1984), which provides an amplification factor, G, between two consecutive time steps. To be a stable scheme, the modulus of the amplification factor, $|G|$, should be less than or equal to one. Another important characteristic to be investigated is the phase lag of the amplification factor:

$$\phi = \tan^{-1} \frac{Im[G]}{Re[G]} \tag{3.4}$$

Now, consider an exact solution of the one dimensional linear advection equation. Its amplification factor is (Anderson et al., 1984):

$$G = e^{-i\beta\lambda} \tag{3.5}$$

where $\beta = 2\pi\Delta x/l$. Thus, the exact solution has a unit amplification factor with a phase lag of $-\beta\lambda$.

Here, l is the wave length of a Fourier component of the spatial action distribution. In other words, the spatial distribution of action values (e.g., square wave in section 3.1.5 or unit pulse in section 3.2.5) can be decomposed into an infinite number of harmonic functions (Fourier components), and l is the wave length of one of the Fourier components. This wave length, l, is thus closely related to the slow variation of wave amplitude in (2.14) whereas the wave length of ocean surface waves, $2\pi/k$, is related to the phase function (2.2).

The value of β varies from 0 to π which corresponds to the Fourier components of an infinitely low frequency and of a Nyquist frequency, respectively. For example, $\beta = \pi$ represents the Fourier component whose wave length is only twice as long as the grid size length, Δx. In wind wave models, since the action distributions are

usually smooth in the spatial coordinates (x, y) and may be rather abrupt in the directional coordinate (θ), the spatial propagation is dominated by the characteristics of numerical schemes in the low β region while the directional propagation is influenced by those in the higher β region.

From the von Neumann stability analysis, the following amplification factor can be derived for the 1st order upwind scheme.

$$G = 1 - \lambda(1 - e^{-i\beta}) \tag{3.6}$$

The stability condition is $|G| \leq 1$ for any β, which provides the stability criterion of this scheme as $|\lambda| \leq 1$.

In the figures to be presented below, the modulus and phase lagging error of the amplification factor are plotted for various Courant numbers (λ) against the β. To be a stable scheme, the modulus of the amplification factor should not exceed 1.0, but a smaller value induces larger dissipation. The phase lagging error is represented by the ratio between the phase lags of the numerical and exact solutions, i.e., $\phi/(-\beta\lambda)$. When this value is larger than 1.0, it gives a phase leading error, and vice versa.

Figure 1 shows the results of the 1st order upwind scheme. First, we can notice that this scheme satisfies the "shift condition" when $\lambda = 1$, i.e., $A_j^{n+1} = A_{j-1}^n$ and the numerical solution coincides with the exact solution. However, a wide range of Courant numbers will be involved in wind wave models since the ocean wave spectra are modeled with many different frequency components resulting in many different propagation speeds.

The modulus of the amplification factor (3.6) decreases as β increases. It starts deviating from 1.0 at the early stage of the low β's, which implies large dissipation in most cases. The modulus for $\lambda = 0.75$ falls over top of that for $\lambda = 0.25$. In

the phase lag plot, no phase lagging error is observed for $\lambda = 0.5$ and 1.0, while it shows phase lagging error for $0 < \lambda < 0.5$ and phase leading error for $0.5 < \lambda < 1$. The truncation error of this scheme is $O[\Delta t, \Delta x]$.

3.1.2 The 2nd Order Upwind Scheme

For a positive propagation speed, the finite difference equation and the amplification factor of the 2nd order upwind scheme with the Euler Explicit time integration can be written as

$$A_j^{n+1} = A_j^n - \lambda \cdot \frac{1}{2}(3A_j^n - 4A_{j-1}^n + A_{j-2}^n) \tag{3.7}$$

$$G = 1 - \lambda \cdot \frac{1}{2}(3 - 4e^{-i\beta} + e^{-2i\beta}) \tag{3.8}$$

Figure 2 shows the modulus and phase lagging error of the amplification factor (3.8). It can be seen that the scheme is unconditionally unstable since its modulus exceeds 1.0 for all λ's. Although it is difficult to see in the case of $\lambda = 0.25$, the value of the modulus always starts from 1.0 at $\beta = 0$, and then increases above 1.0 as β increases. The phase lag coincides with the exact solution for $\lambda = 1.0$ and the other cases ($\lambda < 1$) show phase leading errors. The truncation error becomes $O[\Delta t, (\Delta x)^2]$. Note that this scheme is different from the Warming and Beam's upwind second order scheme (Warming and Beam, 1976) with a truncation error of $O[(\Delta t)^2, (\Delta x)^2]$.

3.1.3 Lax-Wendroff Scheme

Lax and Wendroff (1960) expanded an A_j^{n+1} term into a Taylor series at A_j^n up to second order accurate terms, and using the wave equations, replaced the time derivative terms by the spatial derivative terms. Then, by applying central differencing to the spatial derivative terms, they obtained a second order accurate scheme

which is well known as the Lax-Wendroff scheme. Here, the two-step version of the Lax-Wendroff scheme is introduced since the single-step method becomes unstable when extended to multi-dimensional equations as Gadd (1978b) mentioned. For a one-dimensional linear equation, the two methods are equivalent. The two-step Lax-Wendroff scheme is

$$A_{j+\frac{1}{2}}^{n+\frac{1}{2}} = \frac{1}{2}(A_j^n + A_{j+1}^n) - \frac{\lambda}{2}(A_{j+1}^n - A_j^n) \tag{3.9}$$

$$A_j^{n+1} = A_j^n - \lambda(A_{j+\frac{1}{2}}^{n+\frac{1}{2}} - A_{j-\frac{1}{2}}^{n+\frac{1}{2}}) \tag{3.10}$$

The amplification factor of this scheme is composed of a central differencing first-derivative term and an additional second-derivative term which makes the scheme stable.

$$G = 1 - \lambda \cdot \frac{1}{2}(e^{i\beta} - e^{-i\beta}) + \frac{\lambda^2}{2}(e^{i\beta} - 2 + e^{-i\beta}) \tag{3.11}$$

Figure 3 shows the characteristics of the amplification factor (3.11), which indicates that the scheme is stable for $\lambda \leq 1.0$. It also satisfies the "shift condition" at $\lambda = 1.0$ as does the 1st order upwind scheme. Compared to the 1st order upwind case, the modulus of this scheme is very close to 1.0 in the low β region, which promises much less numerical dissipation. However, a dominant phase lagging error can be expected, since its phase lagging ratio is usually much less than 1.0 in most cases. The phase lagging problem is the main disadvantage of the Lax-Wendroff scheme. This scheme is second order accurate in time and space with a truncation error of $O[(\Delta t)^2, (\Delta x)^2]$.

3.1.4 Modified Lax-Wendroff Scheme

Gadd (1978b) proposed some modification of the Lax-Wendroff scheme to improve its phase lagging problem. He included two more grid points in the second step (3.10) with a control parameter, κ, while the first step (3.9) remains same;

$$A_{j+\frac{1}{2}}^{n+\frac{1}{2}} = \frac{1}{2}(A_j^n + A_{j+1}^n) - \frac{\lambda}{2}(A_{j+1}^n - A_j^n)$$

The second step becomes

$$A_j^{n+1} = A_j^n - \lambda\{(1+\kappa)(A_{j+\frac{1}{2}}^{n+\frac{1}{2}} - A_{j-\frac{1}{2}}^{n+\frac{1}{2}}) - \kappa \cdot \frac{1}{3}(A_{j+\frac{3}{2}}^{n+\frac{1}{2}} - A_{j-\frac{3}{2}}^{n+\frac{1}{2}})\} \tag{3.12}$$

It gives an amplification factor as follows:

$$\begin{aligned} G = 1 &- \lambda\{(1+\frac{2}{3}\kappa)\cdot\frac{1}{2}(e^{i\beta} - e^{-i\beta}) - \frac{2}{3}\kappa\cdot\frac{1}{4}(e^{2i\beta} - e^{-2i\beta})\} \\ &+\frac{\lambda^2}{2}\{(1+\frac{4}{3}\kappa)(e^{i\beta} - 2 + e^{-i\beta}) - \frac{4}{3}\kappa\cdot\frac{1}{4}(e^{2i\beta} - 2 + e^{-2i\beta})\} \end{aligned} \tag{3.13}$$

He derived the equation for the stability criteria and showed that it has the same criteria ($|\lambda| \leq 1$) as the original one, if the parameter, κ, has the following value:

$$\kappa = \frac{3}{4}(1 - \lambda^2) \tag{3.14}$$

The modulus and phase lag error of the amplification factor (3.13) are plotted in Figure 4 for this value of κ. Compared to the original Lax-Wendroff scheme, both characteristics are improved. In particular, the phase lagging ratio in the low β region becomes much closer to 1.0 from the opposite side (upside), which means a phase leading error in this case. Note that the modified Lax-Wendroff scheme uses five (5) grid points in the calculation of the next time step value while three (3) grid points are used in the 2nd order upwind scheme and the original Lax-Wendroff scheme. The order of truncation error is unchanged.

3.1.5 Square Wave Test

The numerical schemes introduced above are tested for square wave propagation. Although this is a rather extreme test for wind wave models, it is a good example to demonstrate the characteristics of numerical schemes. Plotted are the test results after propagating twenty (20) grid points for various Courant numbers.

Figure 5 shows the results of the 1st order upwind scheme. It gives a large amount of dissipation but its phase lag shows good agreement with the exact solution which is given by a solid line. In Figure 6, the 2nd order upwind scheme results are plotted only for $\lambda = 0.25$ since the other Courant numbers yield more unstable and diverging results. Even for this case ($\lambda = 0.25$), it will eventually diverge as iterations continue. Since negative action values are not physically possible for wind waves, we imposed a non-negative condition by setting the negative action values to zero after each iteration. Figure 7 shows the results of this application to the 2nd order upwind scheme. The oscillation ahead of the square wave has been eliminated and the action distribution at that region becomes more spread out. Note that both cases show phase leading errors as can be expected from the phase lagging ratio of this scheme's amplification factor (Figure 2b). Figure 8 represents the results of the Lax-Wendroff scheme. It shows spurious oscillations and a phase lagging error. On the other hand, the modified Lax-Wendroff scheme in Figure 9 shows a slight phase leading error and less spurious oscillations. Figures 10 and 11 show the results after applying the non-negative condition to the Lax-Wendroff scheme and the modified Lax-Wendroff scheme, respectively. As in the 2nd order upwind case, the oscillations around zero are eliminated with a little spreading of the spatial action distribution.

3.2 Two-Dimensional Linear Advection

Consider a two-dimensional linear advection equation with constant propagation speeds.

$$\frac{\partial A}{\partial t} + v_x \frac{\partial A}{\partial x} + v_y \frac{\partial A}{\partial y} = 0 \tag{3.15}$$

The procedure to find the amplification factor is the same as in the one-dimensional case except one more spatial variable is included. Therefore, the amplification factor should be plotted as a function of two variables, (e.g., Fromm, 1968). Most characteristics of the one-dimensional case still hold for the two-dimensional case. The order of truncation errors in time and space remain the same. As another extreme example comparable to the square wave in the one-dimensional case, unit pulse propagation will be presented in the two-dimensional spatial coordinates.

3.2.1 The 1st Order Upwind Scheme

For positive propagation speeds, the two-dimensional finite difference equation of the 1st order upwind scheme becomes

$$\frac{A_{j,k}^{n+1} - A_{j,k}^{n}}{\Delta t} = -v_x \frac{A_{j,k}^{n} - A_{j-1,k}^{n}}{\Delta x} - v_y \frac{A_{j,k}^{n} - A_{j,k-1}^{n}}{\Delta y} \tag{3.16}$$

The value of A at the $n+1$ time step can be written as

$$A_{j,k}^{n+1} = A_{j,k}^{n} - \lambda(A_{j,k}^{n} - A_{j-1,k}^{n}) - \mu(A_{j,k}^{n} - A_{j,k-1}^{n}) \tag{3.17}$$

where $\lambda = v_x \Delta t/\Delta x$ and $\mu = v_y \Delta t/\Delta y$.

The von Neumann stability analysis with two spatial variables yields the following amplification factor:

$$G = 1 - \lambda(1 - e^{-i\beta}) - \mu(1 - e^{-i\gamma}) \tag{3.18}$$

where $\beta = 2\pi\Delta x/l_x$ and $\gamma = 2\pi\Delta y/l_y$.

The corresponding stability criterion is $\lambda+\mu \leq 1$. When the Courant numbers, λ and μ, are equivalent, the criterion becomes $\lambda \leq 0.5$, which is a more restrictive condition than that of the one-dimensional case. This statement can be applied to any numerical scheme.

3.2.2 The 2nd Order Upwind Scheme

This scheme has the following finite difference equation and amplification factor:

$$\begin{aligned} A_{j,k}^{n+1} = A_{j,k}^n &- \lambda \cdot \frac{1}{2}(3A_{j,k}^n - 4A_{j-1,k}^n + A_{j-2,k}^n) \\ &- \mu \cdot \frac{1}{2}(3A_{j,k}^n - 4A_{j,k-1}^n + A_{j,k-2}^n) \end{aligned} \tag{3.19}$$

$$G = 1 - \lambda \cdot \frac{1}{2}(3 - 4e^{-i\beta} + e^{-2i\beta}) - \mu \cdot \frac{1}{2}(3 - 4e^{-i\gamma} + e^{-2i\gamma}) \tag{3.20}$$

And it is still unconditionally unstable.

3.2.3 Lax-Wendroff Scheme

Since the two-step method uses "staggered points" such as $A_{j+\frac{1}{2},k+\frac{1}{2}}$, two-dimensional interpolation involves many grid points making the calculation of the amplification factor rather cumbersome. Hence, the stability criterion will be described without showing the amplification factor. A two-dimensional two-step Lax-Wendroff scheme is

$$\begin{aligned} A_{j+\frac{1}{2},k+\frac{1}{2}}^{n+\frac{1}{2}} =& \frac{1}{4}(A_{j,k}^n + A_{j+1,k}^n + A_{j,k+1}^n + A_{j+1,k+1}^n) \\ &- \frac{\lambda}{2} \cdot \frac{1}{2}(A_{j+1,k}^n - A_{j,k}^n + A_{j+1,k+1}^n - A_{j,k+1}^n) \\ &- \frac{\mu}{2} \cdot \frac{1}{2}(A_{j,k+1}^n - A_{j,k}^n + A_{j+1,k+1}^n - A_{j+1,k}^n) \end{aligned} \tag{3.21}$$

$$\begin{aligned} A_{j,k}^{n+1} = A_{j,k}^n &- \lambda \cdot \frac{1}{2}(A_{j+\frac{1}{2},k-\frac{1}{2}}^{n+\frac{1}{2}} - A_{j-\frac{1}{2},k-\frac{1}{2}}^{n+\frac{1}{2}} + A_{j+\frac{1}{2},k+\frac{1}{2}}^{n+\frac{1}{2}} - A_{j-\frac{1}{2},k+\frac{1}{2}}^{n+\frac{1}{2}}) \\ &- \mu \cdot \frac{1}{2}(A_{j-\frac{1}{2},k+\frac{1}{2}}^{n+\frac{1}{2}} - A_{j-\frac{1}{2},k-\frac{1}{2}}^{n+\frac{1}{2}} + A_{j+\frac{1}{2},k+\frac{1}{2}}^{n+\frac{1}{2}} - A_{j+\frac{1}{2},k-\frac{1}{2}}^{n+\frac{1}{2}}) \end{aligned} \tag{3.22}$$

After some manipulation, the following stability criterion can be obtained (Gadd, 1978b):

$$\lambda^2 + \mu^2 \leq 1 \tag{3.23}$$

Note that this stability criterion is less restrictive than that of the 1st order upwind scheme ($\lambda + \mu \leq 1$). Nine (9) grid points are involved in this calculation while only five (5) grid points are used in the 2nd order upwind scheme.

3.2.4 Modified Lax-Wendroff Scheme

Extension of this scheme to the two-dimensional case requires lots of work at the second step while the first step remains the same as (3.21). Gadd (1980) suggested the following second step using a sixteen (16) point approximation of the half time values ($A^{n+\frac{1}{2}}$).

$$\begin{aligned}
A_{j,k}^{n+1} = A_{j,k}^{n} - \lambda\{&(1+\kappa)\cdot\frac{1}{2}(A_{j+\frac{1}{2},k-\frac{1}{2}}^{n+\frac{1}{2}} - A_{j-\frac{1}{2},k-\frac{1}{2}}^{n+\frac{1}{2}} + A_{j+\frac{1}{2},k+\frac{1}{2}}^{n+\frac{1}{2}} - A_{j-\frac{1}{2},k+\frac{1}{2}}^{n+\frac{1}{2}}) \\
&-\frac{2\kappa}{3}\cdot\frac{1}{6}(A_{j+\frac{3}{2},k-\frac{1}{2}}^{n+\frac{1}{2}} - A_{j-\frac{3}{2},k-\frac{1}{2}}^{n+\frac{1}{2}} + A_{j+\frac{3}{2},k+\frac{1}{2}}^{n+\frac{1}{2}} - A_{j-\frac{3}{2},k+\frac{1}{2}}^{n+\frac{1}{2}}) \\
&-\frac{\kappa}{3}\cdot\frac{1}{6}(A_{j+\frac{3}{2},k-\frac{3}{2}}^{n+\frac{1}{2}} - A_{j-\frac{3}{2},k-\frac{3}{2}}^{n+\frac{1}{2}} + A_{j+\frac{3}{2},k+\frac{3}{2}}^{n+\frac{1}{2}} - A_{j-\frac{3}{2},k+\frac{3}{2}}^{n+\frac{1}{2}})\} \\
-\mu\{&(1+\kappa)\cdot\frac{1}{2}(A_{j-\frac{1}{2},k+\frac{1}{2}}^{n+\frac{1}{2}} - A_{j-\frac{1}{2},k-\frac{1}{2}}^{n+\frac{1}{2}} + A_{j+\frac{1}{2},k+\frac{1}{2}}^{n+\frac{1}{2}} - A_{j+\frac{1}{2},k-\frac{1}{2}}^{n+\frac{1}{2}}) \\
&-\frac{2\kappa}{3}\cdot\frac{1}{6}(A_{j-\frac{1}{2},k+\frac{3}{2}}^{n+\frac{1}{2}} - A_{j-\frac{1}{2},k-\frac{3}{2}}^{n+\frac{1}{2}} + A_{j+\frac{1}{2},k+\frac{3}{2}}^{n+\frac{1}{2}} - A_{j+\frac{1}{2},k-\frac{3}{2}}^{n+\frac{1}{2}}) \\
&-\frac{\kappa}{3}\cdot\frac{1}{6}(A_{j-\frac{3}{2},k+\frac{3}{2}}^{n+\frac{1}{2}} - A_{j-\frac{3}{2},k-\frac{3}{2}}^{n+\frac{1}{2}} + A_{j+\frac{3}{2},k+\frac{3}{2}}^{n+\frac{1}{2}} - A_{j+\frac{3}{2},k-\frac{3}{2}}^{n+\frac{1}{2}})\}
\end{aligned} \tag{3.24}$$

This scheme has the same stability criterion as the original Lax-Wendroff scheme (3.23) if the value of κ is determined by

$$\kappa = \frac{3}{4}(1 - \lambda^2 - \mu^2) \tag{3.25}$$

A total of twenty five (25) grid points are involved through the two steps.

3.2.5 Unit Pulse Test

Propagation of a unit pulse is tested for the above numerical schemes to examine their dispersion properties in two-dimensional spatial coordinates (x, y). Since no refraction is considered, it propagates only in one direction without any propagation between directional bins. This fact allows us to use only one directional band. For the spatial coordinates, a 20 $\times$ 20 grid is used.

At the start of the calculation, four (4) grid points forming a rectangle centered at $(3.5\Delta x, 3.5\Delta y)$ are given unit action values. Elsewhere, the action values are set to zero at the initial time. Two directions of propagation are chosen; one parallel to the x-axis (0°) and the other 60° off from the x-axis. Tests are performed with a Courant number of 0.3. As explained before, this value is not too low in wind wave models.

The results after 20 and 40 time steps are plotted with the exact locations of the center of the unit pulses. The exact locations are marked with a plus(+) sign and the numerical results are shown in a three dimensional contour plot. For each of these figures, the minimum contour value is 0.05 and increases by 0.1 for subsequent contours. The non-negative condition for action values is applied.

Figure 12 shows the results of the 1st order upwind scheme. The location of the peak shows good agreement with the exact solution but, for 60° propagation, the numerical dispersion is so severe that the pulses are spread out through nearly the entire region. For 0° propagation, the lateral propagation is restricted, resulting in one-dimensional propagation along the line parallel to the x-axis. Contours shown in the figure are interpolated results by the plotting routine. Besides the severe numerical dispersion, another problem of the 1st order upwind scheme is that the shape of the dispersion strongly depends on the direction of propagation. To avoid

this problem, the directional grid may be specified not to be aligned with the spatial axes.

Figure 13 shows the results of the Lax-Wendroff scheme. The numerical dispersion is much less than in the 1st order upwind case, and both directions of propagation yield similar shapes. However, the spatial dispersion is not so uniform (circular) and it shows a severe phase lagging problem. Its peaks fall far behind the exact solutions. In Figure 14, further improved results can be seen for the modified Lax-Wendroff scheme. The shape of the dispersion becomes more uniform and its amount is being reduced. More important is the improvement of the phase lagging error. Although the peaks are still behind the exact locations, they become much closer than in the original Lax-Wendroff scheme.

4. TESTS FOR STEADY CASES

The numerical schemes introduced in the previous chapter are tested for some ideal cases which can demonstrate depth and/or current refraction. The problems are restricted to steady-state solution in (x, θ) space since an analytic solution is available in this case for verification of the numerical results. A relatively fine grid (24×24) with 15° resolution is mainly used for the evaluation of the numerical schemes, and some results of a coarser grid (12×12) with 30° resolution are also presented for comparison.

4.1 Analytic Solution

As described in chapter 2, the action balance equation in wave number space can be written as follows when the source function term is taken to be zero:

$$\frac{DN}{DT} = (\frac{\partial}{\partial t} + \dot{\mathbf{x}} \cdot \nabla_{\mathbf{x}} + \dot{\mathbf{k}} \cdot \nabla_{\mathbf{k}})N = 0 \tag{2.36}$$

Its solution, for the steady case, is simply

$$N(\mathbf{k}; \mathbf{x}) = constant \tag{4.1}$$

along a ray. Using equation (2.31), the action density in the wave number space, $N(\mathbf{k}; \mathbf{x}, t)$, can be transformed into the frequency and directional space, $A(\omega, \theta; \mathbf{x}, t)$. Equation (4.1), then, may be written in the frequency and directional space relating two different positions on the same ray; an arbitrary position, $\mathbf{x}$, and a given reference position, $\mathbf{x}_r$.

$$A(\omega, \theta; \mathbf{x}) = \frac{k}{k_r} \frac{(\frac{\partial \omega}{\partial k})_r}{(\frac{\partial \omega}{\partial k})} A(\omega_r, \theta_r; \mathbf{x}_r) \tag{4.2}$$

where the subscript "r" denotes the quantity measured at the reference position. It is convenient to specify the reference position at deep water in the absence of current.

We assume that the water depth (h) and current velocity ($\mathbf{U}$) are not time dependent (i.e., the absolute frequency, ω, is invariant), and that there is no y-direction dependence, thus,

$$\omega = \omega_r \tag{4.3}$$

$$k \sin\theta = k_r \sin\theta_r \tag{4.4}$$

Tayfun et al. (1976) described the following constraints to the analytic solution, which represent wave breaking and reflecting conditions, respectively.

$$\frac{\partial \omega}{\partial k} = \nabla_{\mathbf{k}} \omega \cdot \frac{\mathbf{k}}{k} > 0 \tag{4.5}$$

$$\left(\frac{\omega_o}{\omega}\right)^2 = \frac{k \tanh kh}{k_r \tanh k_r h_r} \geq \frac{\tanh kh}{\tanh k_r h_r} |\sin\theta_r| \tag{4.6}$$

The wave breaking condition (4.5) represents that the energy propagation speed along the orthogonal (perpendicular to crests or troughs) should be positive. In other words, when the current moves so fast in the opposite direction as to reverse the direction of wave propagation, we consider that wave breaking occurs and no wave energy can propagate. The second restriction (4.6) provides the range of directions of propagation for which the wave energy at the reference position, $\mathbf{x_r}$, can reach the position $\mathbf{x}$ without being reflected. It is calculated by setting the extreme value at the position $\mathbf{x}$ (i.e., $|\sin\theta| = 1$). Note that the reflecting condition of (4.6) is based on the reference position in the absence of current.

4.2 Numerical Solutions

The numerical schemes investigated for the linear advection problem are applied to non-linear test cases. The schemes are the 1st and 2nd order upwind schemes, the Lax-Wendroff scheme, and the modified Lax-Wendroff scheme. These will be referred to as UP1, UP2, LW, and LWG, respectively. As investigated in the previous chapter, the 2nd order upwind scheme (UP2) is unstable, but the results presented here are the steady state solutions after the unstable transient behavior has passed away.

Since the propagation velocity, $\mathbf{v}$, is a function of position, the action balance equation can be written in two different forms,

$$\frac{\partial A}{\partial t} + \nabla \cdot (\mathbf{v}A) = 0 \tag{4.7}$$

$$\frac{\partial A}{\partial t} + \mathbf{v} \cdot (\nabla A) + A(\nabla \cdot \mathbf{v}) = 0 \tag{4.8}$$

which are termed the conservative and the non-conservative forms, respectively. For the schemes based on central differencing such as the Lax-Wendroff schemes, these two forms yield very similar results. Hence, only the conservative form is considered for the Lax-Wendroff scheme and the modified Lax-Wendroff scheme. The $(\nabla \cdot \mathbf{v})$ term of the non-conservative form may be evaluated either numerically or analytically. If done numerically, the choice of differencing will have no bearing (other than through the accuracy of the evaluation) on the performance of the propagation scheme as a whole. We have chosen to evaluate it numerically using 2nd order central differencing.

4.3 Test Cases

To compare the numerical solutions to an analytic solution, we must restrict ourselves to steady problems with no y dependence. The governing equation then becomes two-dimensional (x, θ). Since there will be no propagation in the frequency direction ($\dot{\omega} = 0$), we need only treat one frequency. Three cases of depth and/or current refraction are considered.

Case 1. Current Refraction; A current flows in the y direction varying its speed parabolically from zero at both ends to a maximum at the middle of the x region as shown in Figure 15. The peak value is specified to be equal to the wave energy propagation speed in deep water.

Case 2. Depth Refraction; A cubic variation of water depth is designed to cover the range of $0.47 < kh < 3.07$ as shown in Figure 16.

Case 3. Depth and Current Refraction; This case is the combination of the two cases described above.

Choosing the current speed and depth in this way makes the choice of frequency and x scale arbitrary. For the calculation, we chose 0.318 Hz (2 rad/sec) wave frequency and a total length of 240 meters in the x direction. The corresponding current speed is 2.45 m/sec, and water depth varies from 7.5 meters to 0.5 meters.

In each case, an initial energy spectrum,

$$F(\omega, \theta; x_0, t_0) = \begin{cases} \cos^2\theta & -\frac{\pi}{2} \leq \theta \leq \frac{\pi}{2} \\ 0 & elsewhere \end{cases} \tag{4.9}$$

is specified along $x = 0$.

The Courant number, based on maximum total velocity, is chosen as 0.7 for all calculations. In fact, its value doesn't make any difference for a steady-state solution as long as it is within the stability criteria. In the implementation of each scheme, the negative action correction of section 3.1.5 is used.

4.4 Test Results

4.4.1 Analytic Solution

The analytic solutions for the three cases are shown in Figures 17 - 19 at the 15° resolution, and Figure 20 shows another look of Figure 19 (the analytic solution for case 3) at the 30° resolution. We plot the wave energy spectral distribution of the chosen frequency, $F(\theta; x) = \omega_o A(\theta; x)$. In case 1 (current refraction only), Figure 17, energy at positive angles is refracted toward $\theta = 0°$ while a large portion of the energy at negative angles is reflected by the current field. Upon exiting the current field, we recover the initial spectrum, minus the reflected energy at the negative angles. In case 2 (depth refraction only), Figure 18, energy is being concentrated near $\theta = 0°$ as the waves shoal. Case 3 (depth and current refraction), Figure 19, shows a combination of the two effects. These solutions are shown at the relatively fine angular resolution (for a wave model) of 15°, however, we still miss the peak in the current refraction which falls in $15° \leq \theta \leq 30°$. With the 30° resolution, Figure 20, much of the current refraction, including the peak, is missed.

4.4.2 Evaluation of Numerical Results

Corresponding numerical solutions were obtained for each case using most combinations of the above differencing methods in each of the x and θ directions, in combination of conservative and non-conservative forms, and at 15° and 30° angular resolutions. We will use case 3 to demonstrate most of the main conclusions, then examine a reduced set of combinations in the other cases. These calculations were performed on a 24 by 24 grid, which implies a 15° resolution in θ.

To obtain a quantitative measure of the agreement between the analytic and numerical solutions, we have calculated the standard deviation of the two over the

entire grid. Also, since this number is dominated by the peaks in the solution, we have calculated the standard deviation along $x = 0$ only, to isolate the portion of the energy reflected by the current, along $x = L/2$ only (the midpoint of the grid) to examine the current refraction, and along $x = L$ only, to examine what is being transmitted out of the domain. In doing this, there is the danger that, particularly at low resolution, these numbers are dominated by differences between the numerical and analytic solutions in only one or two bins. Often, an objective examination of the plot of a numerical solution will give one a different impression than the standard deviation values. To try to minimize this danger, we will present results for our highest resolution (to have more meaningful statistics), and caution the reader to look at each of the statistics rather than only the overall standard deviation values.

4.4.3 Numerical Solutions

Table 1 shows the standard deviation values for case 3. For the upwind schemes, the type of differencing used (UP1, UP2) in the x and θ directions is shown followed by a C or N to indicate use of the conservative or non-conservative forms respectively. For the Lax-Wendroff schemes, the use of the conservative form is implied. The first thing we notice is that the results are sensitive to the differencing form used in the θ direction, however, for a given differencing form in θ, the results are relatively insensitive to the form used in x. This can be attributed to the fact that the bin to bin variation in the θ direction, especially near the peaks, is much greater than in the x direction. Next, we notice that when using upwind schemes in the θ direction, the non-conservative form yields better agreement with the analytic solution than does the conservative form. The Lax-Wendroff schemes were found to give better agreement than the 2nd order upwind schemes which in turn outperformed

the 1st order schemes. No results are given for Lax-Wendroff schemes in both x and θ directions because this combination resulted in an instability problem.

Recognizing the insensitivity to x direction differencing, we choose 2nd order upwind differencing of the conservative form (UP2C) for the x derivative and examine the behavior of three θ direction differencing schemes with the three geometry cases. The differencing schemes are 2nd order upwind / non-conservative (UP2N), Lax-Wendroff / conservative (LW) and the modified Lax-Wendroff / conservative (LWG). The most commonly used 1st order upwind scheme is also included with the conservative form (UP1C) in both the x and θ derivatives. Table 2 contains the numerical standard deviation results (defined as before) for the three cases. Note that in Tables 2 and 3, the results of the new scheme which will be described in the next chapter are also presented together with these results.

Figure 21 shows the numerical solution of case 1 for the simplest differencing, 1st order upwind differencing of the conservative form for both the x and θ derivatives. The numerical dispersion of this scheme spreads out the peak and the reflected energy. Figures 22 - 24 show solutions using 2nd order upwind differencing of the conservative x derivative and, respectively, 2nd order differencing of the non-conservative form, Lax-Wendroff differencing and modified Lax-Wendroff differencing for the θ derivative. Figure 22 (UP2N) shows less numerical dispersion than in Figure 21, but the over-expansion of energy is observed after exiting the current field. Figure 23 (LW) gives a much larger peak than the analytic solution does, and it shows some noise in the reflected energy and in the over-expanded energy. Figure 24 (LWG) shows similar but improved results to Figure 23 in overall aspects. When examining the case 1 results, recall that the peak of the analytic solution falls between bands and thus although the Lax-Wendroff solutions appear to have overly large peaks, they may actually be better approximations to the analytic

solution than the 1st and 2nd order upwind schemes. Also evident in the figures is a leakage of energy into bands of $\theta \geq 90°$ as the spectrum re-expands upon emerging from the current. Although the analytic solution re-expands up to $\theta = 90°$, the numerical schemes produce some numerical dispersion beyond this limit. This energy travelling beyond $\theta = 90°$ becomes trapped within the current by refraction. The over-expanded energy in the current field grows until the trapped energy and the numerical dispersion are balanced to a steady equilibrium. For a transient case, such a large leakage of energy does not happen since the energy at a specific bin is not supplied continuously for such a long time.

Figures 25 - 28 show the case 2 results in the same order as in the case 1. In Figure 25, the energy spreading due to the 1st order scheme's numerical dispersion can be observed. Figure 26 (UP2N) shows good agreement with the analytic solution for the peak, but yet the numerical dispersion is observed at the other directions of propagation. Figure 27 (LW) gives a smaller peak but less dispersion than the upwind schemes. While the LWG scheme, Figure 28, produces better overall agreement with the analytic solution than the other schemes, it does introduce a small amount of noise which is evident at $\theta = \pm 60°$.

Figures 29 - 32 show the numerical solutions for case 3. Figure 29 (UP1C) shows energy spreading in the peak and reflected area due to the numerical dispersion. Figure 30 (UP2N) shows much improved results but still has a significant amount of dispersion at $\theta = 30°$ and $60°$. It can be seen that the LW scheme, Figure 31, produces superior results to the upwind schemes. The LWG scheme, Figure 32, gives even better results but it has a small amount of noise at the positive angles ahead of the current field.

We have found that the trends observed at the 24 by 24 resolution hold for the 12 by 12 resolution (30° in θ) as well. Table 3 presents the standard deviation

values for 12 by 12 resolution solutions of case 3. Keeping in mind the very few non-zero values on which these statistics are based, we still see superior results when the LWG scheme is used in the θ direction. The results for the same combinations of differencing as in the finer grid are shown in Figures 33 - 36. The UP1C scheme, Figure 33, shows a much smaller peak due to the numerical dispersion. The UP2N scheme, Figure 34, provides a good shape of the peak but shows over-expanded energy at $\theta = 30°$. The LW scheme, Figure 35, gives a smaller peak than the analytic solution and introduces noise at $\theta = -90°$. The LWG scheme, Figure 36, yields superior results except for the noise at $\theta = \pm 90°$.

5. PROPOSAL OF A NEW PROPAGATION SCHEME

In the previous chapter, several numerical schemes were tested for the steady cases of the non-linear two-dimensional advection. For wind wave models, however, the transient behavior is also important. The transient behavior of numerical schemes for linear advection was investigated in chapter 3. These schemes are found to have similar behavior in the more general cases of non-linear and multi-dimensional advection.

The 1st order upwind scheme shows large dispersion for the transient case as was seen in Figures 5 and 12. The initial shapes become very smooth due to numerical dispersion. For the 2nd order upwind scheme, its transient behavior is much worse. The scheme is unstable and diverging no matter how small the Courant number is. Therefore, the 2nd order upwind scheme is out of our candidates for wind wave models. The Lax-Wendroff scheme shows noticeable phase lagging errors for transient cases as shown in the unit pulse test (Figure 13). For steady cases, it provides reasonably accurate results but produces spurious oscillations. The modified Lax-Wendroff scheme shows good performance for both steady and transient cases, except for the spurious oscillations. Another problem of the Lax-Wendroff schemes is that they become unstable when used in both the spatial and directional dimensions.

In this chapter, some methods to remedy the spurious oscillations and the instability problem of the Lax-Wendroff schemes are introduced, and by integrating these methods a new scheme is proposed. The new scheme is designed to take the performance of the modified Lax-Wendroff scheme, reducing the spurious oscillations and avoiding the instability problem by the use of a limiter and time splitting. The tests given in the previous chapters are repeated for the new scheme to check

its performance. Then, this scheme as well as the 1st order upwind scheme are tested for the propagation of wave spectra over an elliptic shoal for which model test results are available.

5.1 The Limiter

According to Godunov's theorem, no second order scheme can be monotone-preserving (Roe, 1986). In other words, the spurious oscillation is an inherent problem of second order schemes which do not possess the "total variation diminishing (TVD)" property as discussed in Morton and Sweby (1987). A limiter is used to retain the TVD property for the higher order schemes by adopting first order schemes where the spurious oscillation is expected. There are various types of limiters to do this work.

For linear advection equations, Sweby(1984) rearranged several second order schemes into the first order upwind scheme and a "limited" flux called an additional anti-diffusive flux. A limiter is the parameter which controls the amount of the "limited" flux. He compared a class of limiters which can be transformed into his expression, and showed the range of values which the limiters may take to keep the scheme oscillation-free. Its application to non-linear equations, however, is quite complicated and the modified Lax-Wendroff scheme, which is our choice from the previous test results, cannot be transformed into his expression. His expression is based on a three(3) point approximation while the modified Lax-Wendroff scheme uses a five(5) point approximation for a one-dimensional advection equation.

Therefore, we will use a rather simple kind of limiter which yields a weighted average of two schemes, i.e., the 1st order upwind scheme and the modified Lax-Wendroff scheme. That is,

$$A_j^{n+1} = A_j^n + s_j^n \Delta A_{j,LWG}^n + (1 - s_j^n) \Delta A_{j,UP1}^n \tag{5.1}$$

where $\Delta A^n_{j,LWG}$ is an increment of A^n_j during one time step as found from the modified Lax-Wendroff scheme and $\Delta A^n_{j,UP1}$ is the corresponding increment from the 1st order upwind scheme. These are combined using a weighting determined by the limiter, s^n_j.

The limiter, s^n_j, varies from 0 to 1, depending on the shape of the variation of A^n near the j-th grid point. The extreme values of s^n_j, 0 and 1, result in the 1st order upwind scheme and the modified Lax-Wendroff scheme, respectively. After testing various types of limiters, we found that the following limiter gives stable and reasonably accurate results. That is,

$$s_j = \frac{|2r_j|}{1 + r_j^2} \tag{5.2}$$

where $r_j = (A_{j+1} - A_j)/(A_j - A_{j-1})$. Figure 37 shows the variation of s_j vs. r_j. This limiter without the absolute value is Van Albada's continuously differential limiter (Van Albada et al., 1982), which when used with the modified Lax-Wendroff scheme produced unstable results.

The limiter, s_j, is a function of r_j which represents the ratio between two consecutive gradients of A. If a gradient of A at one side is dominant, the limiter has a small value which gives more weight to the 1st order upwind scheme to reduce the spurious oscillation. When both sides have comparable gradients, then the result is closer to that of the modified Lax-Wendroff scheme. Note that this limiter satisfies a reciprocal symmetry, i.e., $s(r_j) = s(1/r_j)$, which means that the limiter has the same value for a pair of gradients regardless of their order of appearance.

5.2 Time-Splitting Method

In chapter 3, the numerical schemes were extended from a one-dimensional equation to a two-dimensional equation. The dimensional extension requires tremendous efforts for the schemes which use the "staggered" point approximation (e.g., Lax-Wendroff schemes). Since wind wave models have usually three or four dimensions, the use of the modified Lax-Wendroff scheme for all dimensions is quite difficult.

A time-splitting method (Yanenko, 1971) developed by Soviet mathematicians provides an easier way to solve a multi-dimensional equation. It solves a series of one-dimensional equations instead of one multi-dimensional equation. As a simple example, consider a two-dimensional linear advection equation.

$$\frac{\partial A}{\partial t} + \dot{x}\frac{\partial A}{\partial x} + \dot{y}\frac{\partial A}{\partial y} = 0 \tag{5.3}$$

For explicit schemes, the finite difference equation can be written as follows using an operator notation.

$$A_{j,k}^{n+1} = L_{xy}(\Delta t) A_{j,k}^{n} \tag{5.4}$$

The form of the operator, $L_{xy}(\Delta t)$, depends on the numerical scheme being used. For example, if the 1st order upwind scheme is used, the operator becomes

$$L_{xy}^{UP1}(\Delta t) A_{j,k}^{n} = A_{j,k}^{n} - \frac{\dot{x}\Delta t}{\Delta x}(A_{j,k}^{n} - A_{j-1,k}^{n}) - \frac{\dot{y}\Delta t}{\Delta y}(A_{j,k}^{n} - A_{j,k-1}^{n}) \tag{5.5}$$

The time-splitting method "splits" one equation (5.4) into a couple of one-dimensional equations.

$$A_{j,k}^{n+\frac{1}{2}} = L_{x}(\Delta t) A_{j,k}^{n} \tag{5.6}$$

$$A_{j,k}^{n+1} = L_{y}(\Delta t) A_{j,k}^{n+\frac{1}{2}} \tag{5.7}$$

One-dimensional operators, $L_x(\Delta t)$ and $L_y(\Delta t)$, are defined in the same manner as the two-dimensional operator, $L_{xy}(\Delta t)$. For the case of the 1st order upwind scheme, they are defined as

$$\begin{aligned} L_x^{UP1}(\Delta t)A_{j,k}^n &= A_{j,k}^n - \frac{\dot{x}\Delta t}{\Delta x}(A_{j,k}^n - A_{j-1,k}^n) \\ L_y^{UP1}(\Delta t)A_{j,k}^n &= A_{j,k}^n - \frac{\dot{y}\Delta t}{\Delta y}(A_{j,k}^n - A_{j,k-1}^n) \end{aligned} \tag{5.8}$$

This is also called a fractional step method since one time step is divided into several fractional time steps as we "split" the equations. Besides the ease of handling multi-dimensional equations, this method also provides a wider stability region for numerical schemes. Note that more grid points are used in calculating the split form. For the above example of the 1st order upwind scheme, one more grid point value, $A_{j-1,k-1}^n$, is included in the split form.

When applying the time-splitting method to a second order scheme, the sequence of operators should be symmetric to keep its second order accuracy (Warming and Beam, 1976; Anderson et al., 1984), for example,

$$A_{j,k}^{n+1} = L_x(\frac{\Delta t}{2})L_y(\frac{\Delta t}{2})L_y(\frac{\Delta t}{2})L_x(\frac{\Delta t}{2})A_{j,k}^n \tag{5.9}$$

In the proposed scheme, we have adopted the following sequence to reduce the amount of computation necessary for each time step.

$$A_{j,k}^{n+1} = L_x(\frac{\Delta t}{2})L_y(\Delta t)L_x(\frac{\Delta t}{2})A_{j,k}^n \tag{5.10}$$

Although this is an approximation of (5.9), we retain the second order accuracy.

5.3 New Propagation Scheme

Among the numerical schemes tested in the previous chapters, the modified Lax-Wendroff scheme shows the best performance for both steady and transient cases. The new scheme is based on the modified Lax-Wendroff scheme, adopting the limiter and the time-splitting method to resolve the spurious oscillation and the instability problem described above.

First, the four-dimensional action conservation equation (2.33) can be "split" into the following three equations which represent propagation in a spatial, a frequency, and a directional dimension, respectively.

$$\frac{\partial A}{\partial t} + \frac{\partial}{\partial x}(\dot{x}A) + \frac{\partial}{\partial y}(\dot{y}A) = 0 \tag{5.11}$$

$$\frac{\partial A}{\partial t} + \frac{\partial}{\partial \omega}(\dot{\omega}A) = 0 \tag{5.12}$$

$$\frac{\partial A}{\partial t} + \frac{\partial}{\partial \theta}(\dot{\theta}A) = 0 \tag{5.13}$$

The spatial advection equation (5.11) may be also split into two equations, but we keep this in one equation since the same physical domain is involved. These equations are solved sequentially at each time step.

If we use the operator notations as before, the finite difference equation becomes

$$A^{n+\frac{1}{3}} = L_{xy}(\Delta t)A^n \tag{5.14}$$

$$A^{n+\frac{2}{3}} = L_{\omega}(\Delta t)A^{n+\frac{1}{3}} \tag{5.15}$$

$$A^{n+1} = L_{\theta}(\Delta t)A^{n+\frac{2}{3}} \tag{5.16}$$

Operators are defined in the same manner as in the previous section. For example, when the 1st order upwind scheme is applied, the formula of the two-dimensional operator, L_{xy}, can be derived from equation (3.17). This results in

L_{xy}^{UP1} as defined by equation (5.5). The one-dimensional operators, L_{ω}^{UP1} and L_{θ}^{UP1}, are given by the ω and θ equivalents of equation (5.8) which is derived from (3.3). For the modified Lax-Wendroff case, each operator represents a two step operation. L_{xy}^{LWG} includes the operations of (3.21) and (3.24), while L_{θ}^{LWG} and L_{ω}^{LWG} are the two step operators of equations (3.9) and (3.12).

The 1st order upwind scheme and the modified Lax-Wendroff scheme are then combined by a limiter at each level of the time split equations. The values of the limiters are calculated at the beginning of each time step, Δt, and then be kept unchanged through the fractional time steps. For example, the last level equation (5.16) becomes

$$A^{n+1} = A^{n+\frac{2}{3}} + s_{\theta}^{n}[L_{\theta}^{LWG}(\Delta t) - 1]A^{n+\frac{2}{3}} + (1 - s_{\theta}^{n})[L_{\theta}^{UP1}(\Delta t) - 1]A^{n+\frac{2}{3}} \quad (5.17)$$

where s_{θ}^{n} is the limiter defined by (5.2) in the θ direction.

Since the limiter has a different value for each dimension, the updated value using the two-dimensional operator, (5.14), should be decomposed into x and y components to be combined with the corresponding limiters, s_x^n and s_y^n, which is quite straightforward. The sequence of operators is taken to be symmetric as shown in (5.10) to keep the second order accuracy. Another advantage of the use of the limiter is to be able to avoid erroneous results of the central differencing such as the Lax-Wendroff schemes near a fixed value point (e.g., land boundary, wave breaking point). In this region, the schemes which involve the fixed point often fail to converge due to the constant value being forced at the fixed point. By setting $s_j = 0$ at the adjacent points, this undesirable effect of the fixed point can be avoided.

5.4 Tests For Ideal Cases

The new scheme is tested for the same examples used in chapters 3 and 4. Its amplification factor falls between those of the 1st order upwind scheme and the modified Lax-Wendroff scheme, depending on the local variation of the action values.

Figure 38 shows the square wave test results with the new scheme. No spurious oscillations are observed and its phase lagging error is quite acceptable. It shows more dissipation than the modified Lax-Wendroff scheme but much less than the 1st order upwind scheme. Figure 39 shows the unit pulse propagation using the new scheme. At the very beginning of the propagation, the new scheme is dominated by the 1st order upwind scheme since the initial shape of the unit pulse is very abrupt. Once the abrupt shape is numerically dispersed by the 1st order upwind scheme, the modified Lax-Wendroff scheme starts to contribute its portion. It can be seen that the results are dominated by the 1st order upwind scheme, but the numerical dispersion is a little bit improved at the cost of a phase lagging error. The restriction of the lateral dispersion in the 0° propagation discussed earlier can be avoided by specifying the directional grid not to be aligned with the spatial grid axes. Propagations in 5° and 75° directions (5° and 15° to spatial grid respectively) are shown in Figure 40. It shows less dispersion but more phase lagging error, as the direction of propagation becomes aligned with the spatial grid axis.

Figures 41 - 44 show the results of the new scheme for the steady cases given in chapter 4. They, respectively, represent each of the three test cases in the 15° resolution, and case 3 in the 30° resolution. Figure 41 (case 1) shows good agreement with the analytic solution in the peak and the reflected energy while the spurious oscillation and the energy leakage of the LWG scheme in Figure 24 are significantly improved. Figure 42 (case 2) and Figure 43 (case 3) also show the elimination of

the spurious oscillations of the LWG scheme in Figures 28 and 32. For a coarser grid (Figure 44), some loss of accuracy is observed in the size of the peak and the reflected energy.

The most important fact of this test is that convergent results are achieved with the use of a higher order scheme in both the x and θ directions. Effects of setting the limiter to zero near the wave breaking points can be observed at the region of $x = 80$ m and $\theta = 45°$ in Figures 41 and 43. The standard deviation values defined in chapter 4 are compared in Tables 2 and 3 along with the other numerical schemes.

5.5 Comparison With Experimental Data

Wave propagation over an elliptic shoal was tested at the U.S. Army Engineers' Coastal Engineering Research Center (Briggs, 1987). The tests were performed in a model basin (96 ft long, 114 ft wide) equipped with the directional spectral wave generator. Water depth was adjusted to have a uniform depth of 1.5 ft, and an elliptic shoal (minor radius of 10 ft in the longitudinal direction; major radius of 13 ft in the lateral direction) was located midway along the wave generator and 20 ft away from the wave generator to the center of the elliptic shoal. The height of the elliptic shoal was 1.0 ft at its center so that the minimum water depth was 0.5 ft. Figure 45 shows the layout of the test set-up. The measuring points are marked with the "×" sign in the figure.

Several different wave fields were tested for the same peak frequency ($T = 1.3$ sec). They are a monochromatic wave and irregular wave spectra with different combinations of frequency spreading (Figure 46) and directional spreading (Figure 47). Details of the spreading functions are described in Briggs (1987), Vincent and Briggs (1989), and Panchang et al.(1990). Since they found that the directional

spreading is more important than the frequency spreading, we reduce the comparison cases to the monochromatic wave, the narrow and broad directional spreading waves with the broad frequency spreading. The experimental results of the "initial test series" (Briggs, 1987) are used for comparison since a wide range of measured data are available for those test series in spite of some occurrences of wave breaking. Results are shown in a three-dimensional contour plot of the wave heights normalized by the input wave height. When the wave energy is concentrated, the normalized wave height becomes larger than 1.0 and vice versa. The boundary of the elliptic shoal is shown in a broken line.

Figures 48 - 50 show the model test results for the monochromatic wave, the narrow and broad directional spreading waves, respectively. Note that these figures are based on a relatively small group of measured data points as shown in Figure 45. When evaluating the results, we focus on three aspects of the contour plot, location of the peak, level of the peak, and the pattern of energy concentration. If there is no obstacle such as the elliptic shoal in wave propagation, energy concentration will not happen, resulting in a uniform distribution of wave height except for the three-dimensional effect from the finite length of the wave generator. As can be seen in Figure 48, the monochromatic wave yields a strong energy concentration behind the elliptic shoal in the longitudinal direction. The peak value of the normalized wave height is about 2.4 at $x = 35$ ft. The narrow directional spreading spectrum (Figure 49) shows a similar pattern but its concentration level is much lower than that of the monochromatic wave. It gives a peak of 1.35 between $x = 35$ ft and $x = 40$ ft. The broad directional spreading wave (Figure 50) has a dramatically different look. Instead of a strong concentration, a weak peak of 1.2 is observed above the elliptic shoal, which is far ahead of the peak locations in the other cases.

Before we compare the numerical solutions with the model test results, it should be considered that this is an extreme test of our linear theory because of the relative sizes of the wave length and the radius of the elliptic shoal. The purpose of this numerical calculation is not to obtain an accurate estimation of this problem, but to investigate the performance of the new scheme compared to the widely used 1st order upwind scheme with some indication of proper results. The numerical solutions, however, show good agreement with the model test result for the broad directional spreading case which is the most usual condition in the ocean.

For the numerical calculations, a 20×16 grid is generated in the x-y space as shown in Figure 51. It has a grid size of 2.5 ft in both directions. The frequency spectrum is discretized into fifteen (15) frequency bands with a logarithmic increment, ranging from 0.5 Hz to 2.0 Hz. For the monochromatic wave, only one frequency band of 0.7692 Hz ($T = 1.3$ sec) is used. The directional spreading for the irregular waves is modeled with twelve (12) or twenty four (24) directional bands which correspond to 30° resolution and 15° resolution, respectively. It can be realized from Figure 47 that these resolutions provide very poor approximations, especially for the narrow directional spreading. Both cases of the aligned and misaligned directional grids to the spatial axes are tested. For the misaligned case, the spatial axis is located at the center of the directional bin to avoid asymmetric results.

The numerical solutions are shown for two schemes: (a) the 1st order upwind scheme and (b) the new scheme. Figures 52 and 53 represent the results of the monochromatic wave in the 30° and 15° resolutions, respectively. Since the wave propagates only in the x direction, the misaligned grid is not considered. The new scheme provides better results than the 1st order upwind scheme, and the finer directional grid (15° resolution) yields better results than the 30° resolution grid.

This statement will not be repeated since it is also true for the remaining test cases. The new scheme contributes to improving the level and location of the peak, while the finer directional grid improves aspects including the pattern of energy concentration. The new scheme with the 30° resolution (Figure 52b) yields a result comparable to that of the 1st order upwind scheme with the 15° resolution (Figure 53a). The former has an advantage in the level of the peak while the latter shows a better pattern of energy concentration. In both cases, the locations of the peak are far ahead of model test result.

The numerical results of the narrow directional spreading are given in Figures 54 - 57. For the 30° resolution grid (Figures 54 and 55), the alignment of the directional grid to the spatial axes shows a significant effect on the results, especially for the 1st order upwind scheme case. As described in the unit pulse test, the misaligned grid provides a more uniform shape of the numerical dispersion in the spatial coordinates. In this case, however, it can be attributed rather to the coarse discretization of the directional spreading function (Figure 47). The results of the finer (15°) resolution grid (Figures 56 and 57) are less sensitive to the alignment, since the directional spreading function is discretized in a little more detail for these cases. Compared with the model test result (Figure 49), the numerical solutions provide good estimations in the level of the peak but yet they give the locations of the peak far ahead.

For the broad directional spreading (Figures 58 -61), the choice of the numerical scheme is more sensitive than that of the directional resolution or the alignment. This can be attributed to the fact that the directional spreading function is discretized relatively in detail. Once again, the new scheme shows better performance than the 1st order upwind scheme in the level and location of the peak. It is encouraging that the new scheme with the 30° resolution (Figures 58b and 59b) provides

comparable results to the 1st order upwind scheme with the 15° resolution (Figures 60a and 61a). These numerical results show good agreement with the model test result (Figure 50).

6. APPLICATION TO WIND WAVE MODEL

In this chapter, operation of a wind wave model is demonstrated using the propagation module developed in the previous chapters. For the calculation of the source function terms, a first generation wind wave model named VPINK is used. The development of wind generated sea is simulated for a one-dimensional fetch limited case and at the Bight of Abaco where field measurement of wind and wave data is in progress. The field measurement data for comparison with the numerical results of the wind wave model are unfortunately not yet available. It is assumed that the water depth and current are varying only in space, not in time, so that the absolute frequency (ω) may remain invariant.

6.1 Wind Wave Model

The propagation module developed in the previous chapters is solving the action conservation equation (2.33), while a complete wind wave model should solve the action (or energy) balance equation which includes the source function term. In this paper, the VPINK model will be used to calculate the source function term.

6.1.1 VPINK Wind Wave Model

Since our main concern is investigating the propagation module, a relatively simple wind wave model, the VPINK developed by Neu and Kwon (1986), is chosen. They recognized some erroneous results of the SOWM (Spectral Ocean Wave Model; Pierson, 1982) which is one of the operating wind wave models of first generation. When the wind and wave fields are not aligned, the SOWM responds unreasonably since its growth mechanism is based on the point spectral value with a specified directional spreading function and it does not allow wave growth for each directional

band individually. To remedy this problem, they replaced the point spectral growth mechanism of the SOWM by a directional growth mechanism.

To demonstrate the growth pattern (i.e., source term) of the VPINK model, A point spectral growth in an open sea area (unlimited fetch) is investigated. In this case, the propagation module does not affect at all since there is no dependence in the spatial coordinates. A typical growth pattern of the point spectrum is shown in Figure 62(a). It represents the point spectral evolution at three hour intervals for a steady wind at 10 m elevation of 10 m/sec. For this calculation, sixteen (16) frequency bands and twelve (12) directional bands (30° resolution) are used. The frequency band starts from 0.05 Hz and increases in a logarithmic manner up to 1.0 Hz. The broken line in the figure represents the fully developed sea which is described by the Pierson-Moskowitz spectrum. Figure 62(b) shows the time history of significant wave height corresponding to the point spectral evolution. For the steady wind of 10 m/sec in an open sea, the fully developed sea has the significant wave height of 2.4 m. The significant wave height and the spectral density functions have the following relation:

$$H_s = 4\sqrt{\int_f F_f(f)\, df} = 4\sqrt{\int_\theta \int_\omega F(\omega,\theta)\, d\omega d\theta} \tag{6.1}$$

where H_s is the significant wave height and f is the frequency in Hz. $F_f(f)$ is the point spectrum in frequency base, while $F(\omega,\theta)$ is the spectral energy density function as defined in (2.30).

The VPINK model does not include a bottom friction effect but it does consider wind energy input and, implicitly, non-linear wave-wave interaction as well as the dissipation effect of the waves propagating against wind. For details of the VPINK model, refer to Kwon (1986); Neu and Kwon (1986).

6.1.2 Structure of Wind Wave Model

Wind wave models usually seek to solve the energy or action balance equation. As explained in chapter 2, the action balance equation (2.37) is chosen in this paper since it provides greater ease of computation in a moving medium such as a current.

$$\frac{\partial A}{\partial t} + \nabla_{\mathbf{x}} \cdot (\dot{\mathbf{x}} A) + \frac{\partial}{\partial \omega}(\dot{\omega} A) + \frac{\partial}{\partial \theta}(\dot{\theta} A) = \frac{S}{\omega_o} \tag{2.37}$$

where $A(\omega, \theta; \mathbf{x}, t)$ is the action spectral density function, and $S(\omega, \theta; \mathbf{x}, t)$ is the source function term representing the rate of change of energy. To keep the same dimension of the action on both sides, the source function term, S, is divided by the intrinsic frequency, ω_o.

The idea of the time-splitting method can also be applied to the action balance equation (2.37) as well as to the action conservation equation (2.33). The action balance equation (2.37) can be "split" into two equations as follows:

$$\frac{\partial A}{\partial t} + \nabla_{\mathbf{x}} \cdot (\dot{\mathbf{x}} A) + \frac{\partial}{\partial \omega}(\dot{\omega} A) + \frac{\partial}{\partial \theta}(\dot{\theta} A) = 0 \tag{6.2}$$

$$\frac{\partial A}{\partial t} = \frac{S}{\omega_o} \tag{6.3}$$

The first equation (6.2) which is identical to the action conservation equation (2.33) is responsible for the propagation of wave energy. Numerical schemes investigated and developed in the previous chapters are all about this equation. The second equation (6.3) represents the balance between the local time derivative of the wave action and its generation and dissipation (the source function term) which is calculated by the VPINK model.

Figure 63 shows the flow chart of the wind wave model consisting of three modules; parameter, propagation, and source term modules. The parameter module solves the dispersion relation as described in the Appendix and calculates the

propagation speeds for all dimensions $(\dot{x}, \dot{y}, \dot{\omega}, \dot{\theta})$. Since we assume that the water depth and current are not time dependent, these parameters are calculated once and for all. The propagation module which is the main concern of this paper provides many options of selecting numerical schemes. In the flow chart, a case of selecting the new scheme is presented. At the beginning and the end of this module, conversions between energy and action are performed to solve the propagation problem in the wave action, not in the energy. After calculating the values of limiters once per iteration, the differencing operators are applied in a specified sequence. The source term module calculates wave growth and dissipation using the VPINK model. Upon exiting each of the propagation and the source term modules, the spectral energy values are updated and the non-negative corrections are performed. These two modules are in a time increment loop.

6.2 Simulation Of Developing Wind Sea

Operation of the wind wave model is demonstrated by simulating the development of a wind generated sea in fetch limited areas. After investigating a one-dimensional fetch limited growth, the wind wave model is applied to the Bight of Abaco grid. These calculations are performed using the same conditions as in the example of the point spectral growth (section 6.1.1), i.e., the steady wind of 10 m/sec, which may result in a fully developed sea of 2.4 m significant wave height in an open area, and the sixteen (16) frequency bands (0.05 - 1.0 Hz) and the twelve (12) directional bands (30° resolution). Results are given for the two different propagation schemes; the 1st order upwind scheme and the new scheme proposed in the previous chapter. The effects of the directional grid alignment to the spatial grid axes are also investigated.

6.2.1 One-Dimensional Fetch Limited Growth

The point spectral growth considered in section 6.1.1 represents the wave growth in an open area where the fetch distance is unlimited. Since there is no spatial coordinate (x, y) dependence in this case, the propagation module did not affect the calculation results at all. A fetch limited growth is simulated for a one-dimensional grid (no y dependence) of which one end is a land point and the other open. A total length of 200 km is modeled with a grid size of 20 km. A steady wind blows orthogonally offshore (i.e., from the land point to the open point) on initially calm water. Effects of depth and current refraction are investigated for the same profiles (Figures 15 and 16) as used in the steady test cases of chapter 4.

Figure 64 represents the evolution of significant wave height along the fetch distance (x axis) without any refraction (deep water and no current). Calculations are performed with a 20 minute time step and the results are shown at 2 hour intervals. No significant differences are observed between (a); the spatial grid axes coincide with the directional band, and (b); the spatial and directional grids are set to be misaligned by 15°. The new scheme, compared to the 1st order upwind scheme, yields higher wave heights during the developing sea and lower values at the steady state condition. This observation implies that the new scheme propagates more energy than the 1st order upwind scheme. Effects of the current (maximum speed 2.45 m/sec) are not so significant in this case (Figure 65), resulting in a little decrease of wave height in the current zone. This can be explained by the fact that the peak of energy concentration due to the current refraction falls in a directional bin which, for the relatively coarse grid (30° resolution), misses the peak for both cases of (a) and (b). Figure 66 shows the results of the depth refraction, in which the alignment of the spatial and directional grids has significant effects, especially for the new scheme. Energy is concentrated due to the depth refraction

near $\theta = 0°$ where the directional band does exist in (a), and does not in (b). The misaligned grid, (b), gives lower wave heights since it misses the peak at $\theta = 0°$. The 1st order upwind scheme, however, shows less differences between (a) and (b) because of its large numerical dispersion as in the steady case (Figure 25). Note that the discussion of the grid alignment in this example is different from that in the unit pulse test case where the necessity of the misaligned grid was introduced. In the unit pulse test, the numerical schemes, especially the 1st order upwind scheme (Figure 12), showed different patterns of numerical dispersion depending on the angle between the direction of propagation and the spatial grid axis. The problem in this section is not the numerical dispersion but whether the directional grid is modeled to include the region of energy concentration ($\theta = 0°$) or not. The wave growth rate is proportional to the amount of energy present. When the current refraction as well as the depth refraction (Figure 67) are considered, the pattern of energy concentration becomes asymmetric and the grid alignment results in less discrepancy, especially for the new scheme.

6.2.2 Simulation of the Bight of Abaco

A group of scientists including my advisor are involved in a long term research project of developing an integrated wind wave model. As a part of this project, they are collecting field measurement data of wind and wave spectra at a fetch limited region. The Bight of Abaco in Bahamas provides such a good fetch limited region since it has a semi-enclosed ocean area of an appreciable size. An intensive measurement of wind and wave data is being carried out at this region for two years, but unfortunately it is not yet ready to compare with the results of a wind wave model.

Figure 68 shows the geometry and bathymetry of this region. The enclosed area is about 100 km long and 40 km wide. One division of the frame in the figure is 10 km long. The maximum depth in this region does not exceed 10 m and the northern part is generally deeper than the southern part. The only open boundary, in the southwest, has very shallow water depth so that the effects from the open sea are significantly blocked. It is modeled with a square grid of 4.8 km length as shown in Figure 69. In the figure, the locations of wave arrays and weather stations are also shown. A total of 152 grid points are involved, among which boundary points are defined as either a fixed point (land point) or an open boundary point (only outflow of energy is allowed). Figure 70 represents the depth contour map of the modeled region, based on the input data of depth at each grid point.

Two-dimensional fetch limited growth is simulated for a steady wind of 10 m/sec in several different directions. Calculations are performed using a 100 second time step, and the same frequency (16) and directional (12) bands as before. Simulated results are presented in a three-dimensional contour plot of significant wave heights (in meters). The arrows indicate the mean directions of propagation at each grid point, and their lengths are linearly proportional to the significant wave heights. All the figures represent the wave growth after 10 hour duration of the steady wind on initially calm water. This time duration is long enough to reach a steady state sea for this example. Although observations are not yet available to confirm these results, the wave heights calculated agree well with expected values for this wind speed and region.

First, effects of the grid alignment are investigated. As mentioned in the previous section, the necessity of the misaligned grid was introduced in the unit pulse test where the 1st order upwind scheme showed very different patterns of numerical dispersion, depending on the angle between the spatial grid axis and the directional

grid. To examine the effects of the grid alignment apart from the depth refraction, the Abaco grid is tested assuming deep water everywhere with a northwest wind which blows along the spatial grid axis.

Figures 71 and 72 show these results with the 1st order upwind scheme using the aligned grid and the misaligned grid, respectively. Noticeable differences are observed along the open boundary and behind the isolated island. The aligned grid (Figure 71) propagates wave energy in a straight pattern along the wind direction while the misaligned grid (Figure 72) shows a pattern of energy propagation which smoothly follows the boundaries.

The same trend can be observed in the results of the new scheme (Figures 73 and 74). The misaligned (Figure 74) grid allows more energy to be bent near the open boundary and the island than the aligned grid (Figure 73) does. In Figure 73, spurious oscillations occur perpendicular to the wind. They result from the mechanism of the staggered point approximation (e.g., Lax-Wendroff schemes) which transfers boundary effects in an alternating pattern. For the aligned grid, this kind of spurious oscillation can happen in the directional band which is parallel to a boundary and also parallel to the spatial grid axis. It is another advantage of the misaligned grid to be able to avoid this spurious solution. In the following, except where noted, calculations are limited to the misaligned grid only.

Next, effects of depth refraction are investigated as well as those of the propagation schemes (i.e., the 1st order upwind scheme and the new scheme). Two different wind directions are simulated using a misaligned grid with 30° resolution.

Figures 75 and 76 show these results for the northwest wind as before. The depth refraction changes the mean direction of wave propagation along the boundaries, especially behind the island. While the 1st order upwind scheme shows less differences between the deep water (Figure 72) and the depth refraction (Figure

75), the new scheme yields more refracted results, evident in the shape of energy concentration in Figure 76 (depth refraction) compared with Figure 74 (deep water).

Figures 77 - 80 represent the simulated results for a north wind. The deep water results (Figures 77 and 78) give a higher level of significant wave heights and more homogeneous mean directions of wave propagation than the depth refraction cases (Figures 79 and 80). The depth refraction (Figures 79 and 80) causes the mean directions of propagation to be bent toward shallow water, resulting in lower wave heights at the center of the region. As in the previous wind direction, the new scheme (Figure 80) shows more energy refraction along the boundaries than the 1st order upwind scheme (Figure 79), which can be clearly noticed by the mean directions of propagation and the shape of energy concentration along the island.

7. CONCLUSION

A new numerical scheme for the propagation of wind wave spectra was proposed after investigating the characteristics of some higher order numerical schemes. They were examined as an alternative to the commonly used 1st order upwind scheme for the action balance equation. The schemes examined are the 2nd order upwind scheme, the Lax-Wendroff scheme, and the modified version of Lax-Wendroff scheme suggested by Gadd.

First, their characteristics were investigated for a linear advection equation which is equivalent to deep water in the absence of current. After calculating the amplification factors, transient behaviors were demonstrated in a one-dimensional space (square wave test) as well as in a two-dimensional space (unit pulse test). These tests showed severe dissipation and numerical dispersion of the 1st order upwind scheme, and diverging results for the 2nd order upwind scheme. The Lax-Wendroff schemes showed superior results in the aspect of the numerical dispersion, but the Lax-Wendroff scheme had a significant phase lagging problem. This problem was much improved in the modified Lax-Wendroff scheme.

Then, these schemes were applied to a non-linear advection equation in which depth and current refraction is considered. To compare with an analytic solution, the problem was restricted to the steady state solution in an x-θ space. Various combinations of differencing schemes were tested including the conservative and non-conservative forms in the upwind schemes. From this problem, we found:

a. The choice of the numerical scheme used in the θ-direction is more important than that in the x-direction when wave energy is concentrated in a small number of bands due to refraction.

b. For upwind schemes in the θ-direction, the non-conservative derivative form gives better results than the conservative form. However, there is little difference between these forms when using a Lax-Wendroff scheme.

c. Lax-Wendroff schemes have less tendency to spread out (or are more capable of concentrating) the energy in direction than the upwind schemes, however, they introduce a small amount of noise into the solution.

d. The modified Lax-Wendroff scheme of Gadd performed better than the original for this problem.

A new scheme was designed to take advantage of the modified Lax-Wendroff scheme's performance at the same time reducing the spurious oscillation of the second order schemes. A continuous limiter was suggested which gives a weighted average of the 1st order upwind scheme and the modified Lax-Wendroff scheme, depending on the shape of variation of the action (or energy) values. The instability problem of the Lax-Wendroff schemes when used in both the spatial and directional dimensions was remedied by introducing a time-splitting method. This method provides a wider range of numerical stability as well as the ease of handling a multi-dimensional equation. Application of the new scheme to the previous examples showed successful results.

As another example, propagation of wave spectra over an elliptic shoal was simulated for which model test results are available. Although it is an extreme test for a linear wave theory, the numerical calculations gave very encouraging results, especially for a wave spectrum broadly spread in direction. The new scheme with 30° resolution provided comparable results to the 1st order upwind scheme with 15° resolution.

The complete action balance equation was solved by combining the propagation module (action conservation equation) with a source function term (VPINK model).

Operation of the wind wave model was simulated for a one-dimensional fetch limited case and for the Bight of Abaco grid. They showed that depth refraction has significant effects on the shape of energy concentration and the mean directions of propagation. The new scheme provided more energy propagation and more refraction than the 1st order upwind scheme did, resulting in a more smooth pattern of wave energy flow along the boundaries. When a directional band is aligned with a spatial grid axis which is also parallel to the boundaries, the staggered point approximations, such as the Lax-Wendroff schemes, induce spurious solutions along the axis perpendicular to the directional band. This can be avoided by setting the directional grid to be misaligned to the spatial grid axes, which also provides more uniform numerical dispersion for each direction of propagation.

REFERENCES

Anderson, D.A., J.C. Tannehill and R.H. Pletcher, 1984: *Computational Fluid Mechanics and Heat Transfer*, Hemisphere Publishing Corporation.

Boris, J.P. and D.L. Book, 1973: Flux-Corrected transport, *J. Computational Physics*, **11**, 38-69.

Bretherton, F.P. and C.J.R. Garrett, 1969: Wavetrains in inhomogeneous moving media, *Proc. Roy. Soc.*, A. **302**, 529-554.

Briggs, M.J., 1987: Summary of WET shoal test results, *CEWES-CW-P*, Coastal Engineering Research Center.

Crank, J. and P. Nicolson, 1947: A practical method for numerical evaluation of solutions of partial differential equations of the heat-conduction type, *Proceedings of the Cambridge Philosophical Society*, **43**, no.50, 50-67.

Fromm, J.E., 1968: A method for reducing dispersion in convective difference schemes, *J. Computational Physics*, **3**, 176-189.

Gadd, A.J., 1978a: A split explicit integration scheme for numerical weather prediction, *Quart. J. R. Met. Soc.*, **104**, 569-582.

Gadd, A.J., 1978b: A numerical advection scheme with small phase speed errors, *Quart. J. R. Met. Soc.*, **104**, 583-594.

Gadd, A.J., 1980: Two refinements of the split explicit integration scheme, *Quart. J. R. Met. Soc.*, **106**, 215-220.

Golding, B., 1983: A wave prediction system for real-time sea state forecasting, *Quart. J. R. Met. Soc.*, **109**, 393-416.

Hasselmann, K., 1962: On the non-linear energy transfer in a gravity-wave spectrum; Part 1, general theory, *J. Fluid Mech.*, **12**, no.4, 481-500.

Hasselmann, K., T.P. Barnett, E. Bouws, H.Carlson, D.E. Cartwright, K. Enke, J.A. Ewing, H. Gienapp, D.E. Hasselmann, P. Kruseman, A. Meerburg, P. Muller, D.J. Olbers, K. Richter, W. Sell and H. Walden, 1973: Measurements

of wind-wave growth and swell decay during the Joint North Sea Wave Project (JONSWAP), *Deut. Hydrogr. Z.*, **A12**.

Hubbert, K.P. and J. Wolf, 1991: Numerical investigation of depth and current refraction of waves, *J. Geophysical Research*, **96**, no.C2, 2737-2748.

Karlsson, T., 1969: Refraction of continuous ocean wave spectra, *J. Waterways and Harbors Division, ASCE*, **WW4**, 437-448.

Kwon, S.H., 1986: *Directional growth of wind generated waves*, Ph.D. dissertation, Virginia Polytechnic Institute and State University.

Lax, P.D. and B. Wendroff, 1960: Systems of conservation laws, *Comm. Pure Appl. Math.*, **13**, 217-237.

LeBlond, P.H. and L.A. Mysak, 1978: *Waves in the Ocean*, Elsevier Scientific Publishing Company.

Longuet-Higgins, M.S., 1956: The refraction of sea waves in shallow water, *J. Fluid Mech.*, **1**, 163-176.

Longuet-Higgins, M.S. and R.W. Stewart, 1961: The changes in amplitude of short gravity waves on steady non-uniform currents, *J. Fluid Mech.*, **10**, 529-549.

Mehaute, B.L. and J.D. Wang, 1982: Wave spectrum changes on sloped beach, *J. Waterway, Port, Coastal and Ocean Division, ASCE*, **108**, no.WW1, 33-47.

Mei, C.C., 1983: *The Applied Dynamics of Ocean Surface Waves*, A Wiley Interscience Publication, John Wiley & Sons.

Miles, J.W., 1957: On the generation of surface waves by shear flow, *J. Fluid Mech.*, **3**, no.2, 185-204.

Morton, K.W. and P.K. Sweby, 1987: A comparison of flux limited difference methods and characteristic Galerkin methods for shock modelling, *J. Computational Physics*, **73**, 203-230.

Neu, W.L. and S.H. Kwon, 1986: Directional growth for numerical wind wave models, *Proceedings of Coastal Engineering*, **1**, 618-632.

Neu, W.L. and Y.S. Won, 1990: Propagation schemes for wind wave models with finite depth and current, *Proceedings of CAMS (Canadian Applied Mathematics Society) Conference*, 947-954.

Newman, J.N., 1977: *Marine Hydrodynamics*, The MIT Press.

Noye, J., 1987: Time-splitting the one-dimensional transport equation, *Numerical Modelling: Application to Marine Systems*, Elsevier Science Publishers B.V., 271-295.

Panchang, V.G., G. Wei, B.R. Pearce and M.J. Briggs, 1990: Numerical simulation of irregular wave propagation over shoal, *J. Waterway, Port, Coastal, and Ocean Engineering*, **116**, no.3, 324-340.

Phillips, O.M., 1957: On the generation of surface waves by turbulent wind, *J. Fluid Mech.*, **2**, no.5, 417-445.

Phillips, O.M., 1977: *The Dynamics of the Upper Ocean*, second edition, Cambridge University Press.

Pierson, W.J., 1982: The spectral ocean wave model (SOWM); A northern hemisphere computer model for specifying and forecasting ocean wave spectra, DTNSRDC-82/011.

Pond, S. and G.L. Pickard, 1983: *Introductory Dynamical Oceanography*, second edition, Pergamon Press.

Roe, P.L., 1986: Characteristic-based schemes for the Euler equations, *Ann. Rev. Fluid Mech.*, **18**, 337-365.

Sakai, T., M. Koseki and Y. Iwagaki, 1983: Irregular wave refraction due to current, *J. Hydraulic Engineering, ASCE*, **109**, no.9, 1203-1215.

The SWAMP Group, 1988: *Ocean Wave Modeling*, Plenum Press.

Sweby, P.K., 1984: High resolution schemes using flux limiters for hyperbolic conservation laws, *SIAM J. Numer. Anal.*, **21**, no.5, 995-1011.

Tayfun, M.A., R.A. Dalrymple and C.Y. Yang, 1976: Random wave-current interactions in water of varying depth, *Ocean Engineering*, **3**, 403-420.

Tolman, H.L., 1989: The numerical model WAVEWATCH; A third generation model for hindcasting of wind waves on tides in shelf seas, *Report No.89-2*, Delft University of Technology.

Tolman, H.L., 1990: The influence of unsteady depths and currents of tides on wind-wave propagation in shelf seas, *J. Physical Oceanography*, **20**, no.8, 1166-1174.

Van Albada, G.D., B. Van Leer and W.W. Roberts Jr., 1982: A comparative study of computational methods in cosmic gas dynamics, *Astron. Astrophys.*, **108**, 76-84.

Vincent, C.L. and M.J. Briggs, 1989: Refraction-diffraction of irregular waves over a mound, *J. Waterway, Port, Coastal, and Ocean Engineering*, **115**, no.2, 269-284.

The WAMDI Group, 1988: The WAM model - A third generation ocean wave prediction model, *J. Physical Oceanography*, **18**, 1775-1810.

Warming, R.F. and R.M. Beam, 1976: Upwind second-order difference schemes and applications in aerodynamic flows, *AIAA Journal*, **14**, no.9, 1241-1249.

Whitham, G.B., 1965: A general approach to linear and non-linear dispersive waves using a Lagrangian, *J. Fluid Mech.*, **22**, part 2, 273-283.

Yanenko, N.N., 1971: *The Method of Fractional Steps*, The Solution of Problems of Mathematical Physics in Several Variables (English translation edited by M. Holt), Springer-Verlag.

APPENDIX: Solution of Dispersion Relation for a Moving Medium

As described in section 2.2, a linear gravity wave should satisfy the dispersion relation which is derived from the dynamic free surface condition. In a moving medium such as a current, an intrinsic frequency is involved in the dispersion relation, resulting in the following simultaneous equations:

$$\omega = \omega_o + \mathbf{k} \cdot \mathbf{U} \tag{2.7}$$

$$\omega_o^2 = kg \tanh kh \tag{2.8}$$

In most cases, the unknown variables are the intrinsic frequency, ω_o, and the wave number, k. Since these equations have multiple roots, it is necessary to choose the correct one. A graphical solution (Mei, 1983) provides good understanding on the characteristics of the roots. Rearranging the above equations to represent ω_o as a function of k, we have

$$\omega_o = \omega - qk \tag{A1}$$

$$\omega_o = \pm\sqrt{kg \tanh kh} \tag{A2}$$

where $q = \mathbf{U} \cdot \mathbf{k}/k$.

The roots can be found from the intersections of the straight line, $(A1)$, and the curve, $(A2)$, as shown in Figure 81. In this figure, the deep water approximation ($\tanh kh = 1$) and the shallow water approximation ($\tanh kh = kh$) are plotted in broken lines, and only positive values of the absolute frequency (ω) and wave number (k) are considered. The simplest case is when the current moves orthogonally to the direction of wave propagation ($\mathbf{k} \cdot \mathbf{U} = 0$). Obviously, the intrinsic frequency is equal to the absolute frequency in this case, resulting in a single root at point Z which is identical to the solution in the absence of current.

When the current moves in a favorable direction to the wave ($\mathbf{k} \cdot \mathbf{U} > 0$), two roots always exist, P_1 and P_2, which respectively yield a positive and a negative intrinsic frequency. Our choice is clearly the positive one (P_1) since it provides continuity near $\mathbf{k} \cdot \mathbf{U} = 0$. As the current speed increases, the wave length and the relative (intrinsic) propagation speed also increase. The negative root (P_2) represents the wave which propagates in the opposite direction from a view point of the moving coordinate system. Its phase velocity is still favorable to the current but so slow as to be swept along by the current.

When the current flows against the wave ($\mathbf{k} \cdot \mathbf{U} < 0$), solutions may or may not exist depending on the value of q ($= \mathbf{U} \cdot \mathbf{k}/k$). The threshold case has a double root at N_{12} which corresponds to the critical wave breaking condition (4.5) described in section 4.1. In this case, wave energy is no longer propagated (group velocity), but the shape of the wave is still being propagated (phase velocity). No solutions exist beyond this threshold, while there are two roots (N_1 and N_2) for a weaker current. As the current speed decreases, the wave length and intrinsic propagation velocity increase for the smaller root (N_1), and the opposite is true for the larger one (N_2). The smaller root (N_1) is again our choice which satisfies the continuity near $\mathbf{k} \cdot \mathbf{U} = 0$.

These equations can be solved numerically by one of many root finding methods. In this problem, no matter which method is used, a good initial guess of the root is very important for the correct convergence, since the variation near the desired root easily misleads the root finding methods to converge to the other root or to diverge. In the following, the two equations, ($A1$) and ($A2$), are combined into a single equation, and then the corresponding initial guess value is derived along with constraints on the root.

By equating the intrinsic frequency terms of $(A1)$ and $(A2)$, a single equation involving to the wave number is obtained. Using non-dimensional variables,

$$f(k') = (\omega' - q'k')^2 - k' \tanh k' = 0 \tag{A3}$$

where $\omega' = \omega\sqrt{h/g}, q' = q\sqrt{gh}$, and $k' = kh$.

The shallow water approximation provides

$$f(k') = (\omega' - q'k')^2 - k'^2 = 0 \tag{A4}$$

Since it is found from the graphical solution that both ω_o and k are positive, equation $(A4)$ has the solution of

$$k' = \frac{\omega'}{q' + 1} \tag{A5}$$

with a constraint of

$$q' + 1 > 0 \tag{A6}$$

The deep water approximation of equation $(A3)$ is

$$f(k') = (\omega' - q'k')^2 - k' = q'^2 \left[k'^2 - \left(\frac{2\omega'}{q'} + \frac{1}{q'^2} \right) + \left(\frac{\omega'}{q'} \right)^2 \right] = 0 \tag{A7}$$

which has the roots of

$$k' = \left(\frac{\omega'}{q'} + \frac{1}{2q'^2} \right) \pm \sqrt{\left(\frac{\omega'}{q'} + \frac{1}{2q'^2} \right)^2 - \left(\frac{\omega'}{q'} \right)^2} \tag{A8}$$

under the constraint that

$$\left(\frac{\omega'}{q'} + \frac{1}{2q'^2} \right)^2 - \left(\frac{\omega'}{q'} \right)^2 = \frac{1}{4q'^4}(1 + 4\omega' q') \geq 0 \tag{A9}$$

From the graphical solution, it is seen that the smaller root of k' is the desired solution. A good initial guess of the root can be obtained by interpolating the following two values:

$$k'_1 = \left(\frac{\omega'}{q'} + \frac{1}{2q'^2}\right) - \sqrt{\left(\frac{\omega'}{q'} + \frac{1}{2q'^2}\right)^2 - \left(\frac{\omega'}{q'}\right)^2} \tag{A10}$$

$$k'_m = \frac{\omega'}{q'} + \frac{1}{2q'^2} \tag{A11}$$

The secant method gives the initial guess as

$$k'_i = \frac{k'_1 f(k'_m) - k'_m f(k'_1)}{f(k'_m) - f(k'_1)} \tag{A12}$$

where the function $f(k')$ is the same as $(A3)$.

Equation $(A3)$ can now be solved. In this paper, the Newton-Raphson method, one of the slope methods, is used to find the root. Finally, the slope of the function $f(k')$ at the root is checked, which should be negative, to confirm the correct root convergence. For the cases tested in this paper, this initial guess is very successful in converging quickly to the desired root.

Table 1. Standard Deviation from the Analytic Solution for Various Differencing Combinations - Case 3, 24 x 24 grid

x	θ	σ_{all}	$\sigma_{x=0}$	$\sigma_{x=L/2}$	$\sigma_{x=L}$
UP1C	UP1C	0.2135	0.0308	0.2547	0.2684
UP1N	UP1C	0.2174	0.0312	0.2409	0.2562
UP1C	UP1N	0.1957	0.0320	0.1626	0.2281
UP1N	UP1N	0.2195	0.0313	0.1406	0.2324
UP2C	UP2C	0.1981	0.0302	0.2365	0.2503
UP2N	UP2C	0.1996	0.0306	0.2350	0.2508
LW	UP2C	0.2317	0.0359	0.2282	0.2488
UP1C	UP2N	0.1784	0.0269	0.2004	0.1828
UP1N	UP2N	0.1784	0.0279	0.1829	0.1745
UP2C	UP2N	0.1745	0.0241	0.1802	0.1820
UP2N	UP2N	0.1764	0.0249	0.1764	0.1814
LW	UP2N	0.1937	0.0259	0.1709	0.1772
LWG	UP2N	0.1938	0.0252	0.1713	0.1774
UP2C	LW	0.1499	0.0281	0.1150	0.0817
UP2C	LWG	0.1261	0.0196	0.0816	0.0898

Table 2. Standard Deviation from the Analytic Solution for Cases 1,2, and 3 - 24 x 24 grid

case	x	θ	σ_{all}	$\sigma_{x=0}$	$\sigma_{x=L/2}$	$\sigma_{x=L}$
	UP1C	UP1C	0.1786	0.0656	0.3374	0.1554
	UP2C	UP2N	0.1777	0.0467	0.3375	0.0680
1	UP2C	LW	0.2645	0.0405	0.6322	0.0449
	UP2C	LWG	0.2525	0.0400	0.5844	0.0472
	new	new	0.1986	0.0443	0.4618	0.0909
	UP1C	UP1C	0.1457	0.0000	0.0814	0.2541
	UP2C	UP2N	0.0772	0.0000	0.0451	0.1255
2	UP2C	LW	0.0754	0.0000	0.0374	0.1152
	UP2C	LWG	0.0406	0.0003	0.0247	0.0469
	new	new	0.0660	0.0004	0.0364	0.0981
	UP1C	UP1C	0.2135	0.0308	0.2547	0.2684
	UP2C	UP2N	0.1745	0.0241	0.1802	0.1820
3	UP2C	LW	0.1499	0.0281	0.1150	0.0817
	UP2C	LWG	0.1261	0.0196	0.0816	0.0898
	new	new	0.1392	0.0217	0.1216	0.1006

Table 3. Standard Deviation from the Analytic Solution for Various Differencing Combinations - Case 3, 12 x 12 grid

x	θ	σ_{all}	$\sigma_{x=0}$	$\sigma_{x=L/2}$	$\sigma_{x=L}$
UP1C	UP1C	0.2031	0.0494	0.0293	0.3449
UP1C	UP2N	0.2008	0.0479	0.0182	0.2929
UP2C	UP2N	0.1887	0.0505	0.0269	0.2798
UP2C	LW	0.2122	0.0376	0.0394	0.2776
UP2C	LWG	0.1759	0.0274	0.0196	0.1503
new	new	0.1540	0.0345	0.0305	0.1953

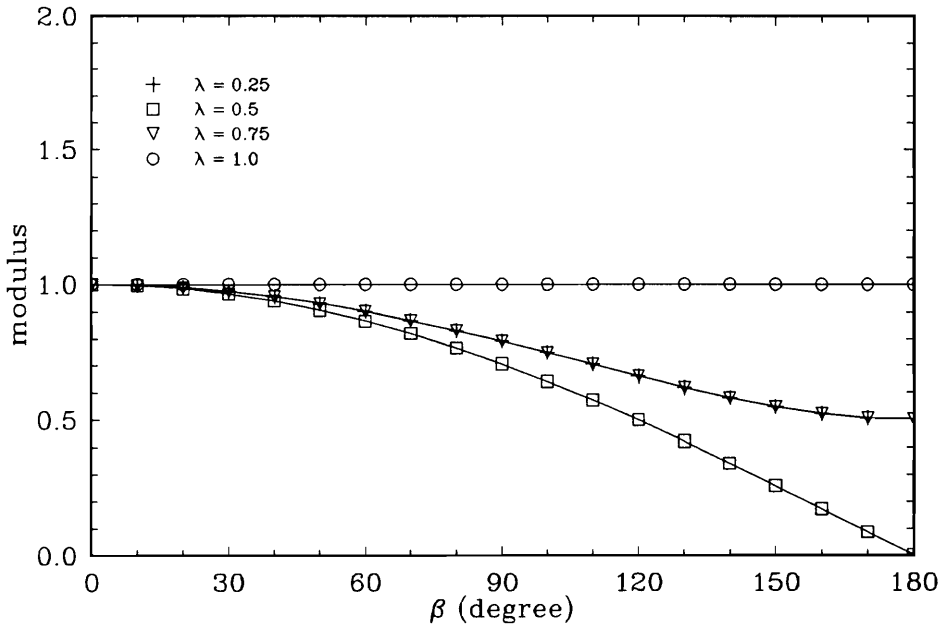

(a) modulus, $|G|$

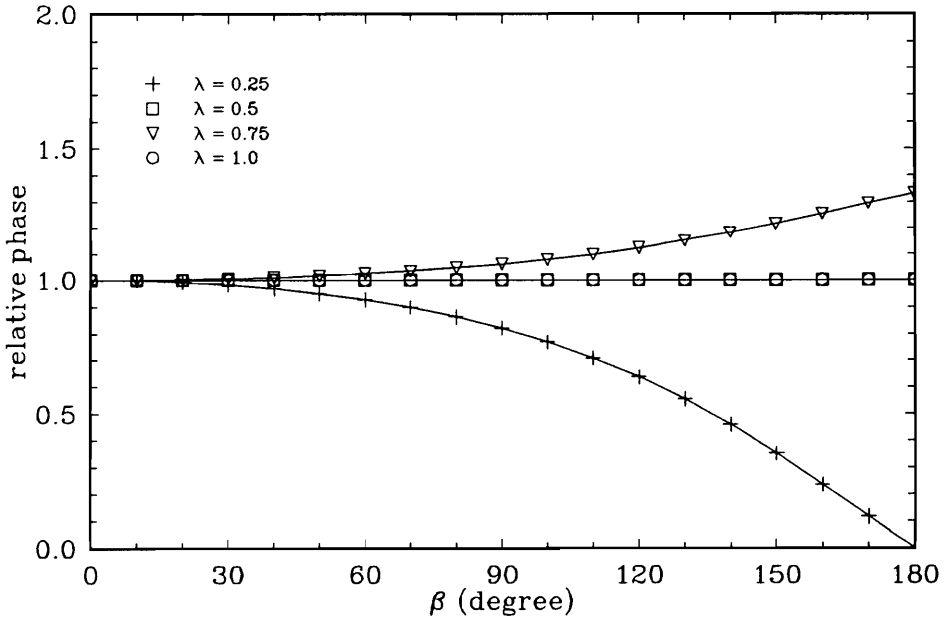

(b) relative phase, $\phi/(-\beta\lambda)$

Figure 1. Amplification factor of 1st order upwind scheme

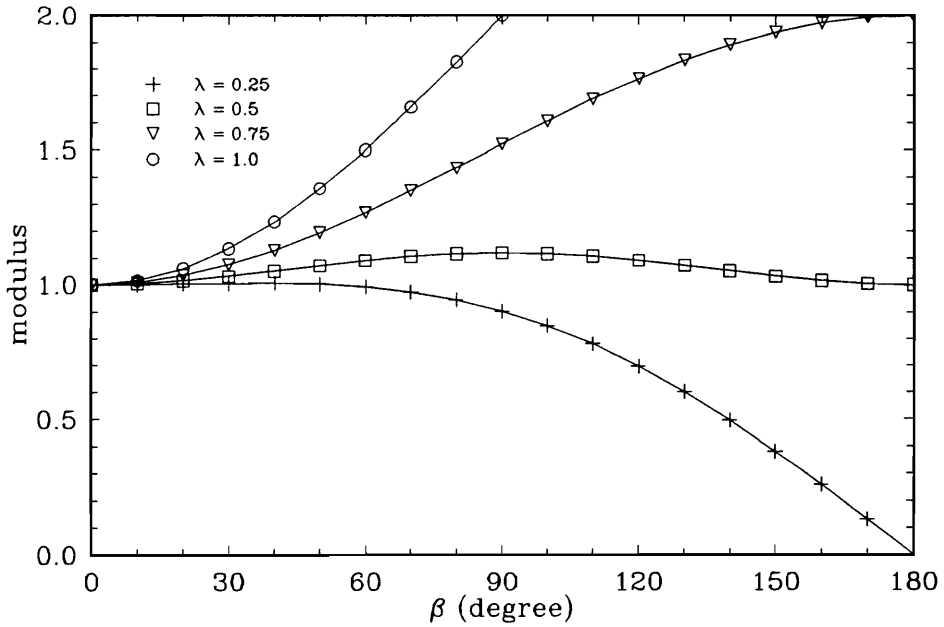

(a) modulus, $|G|$

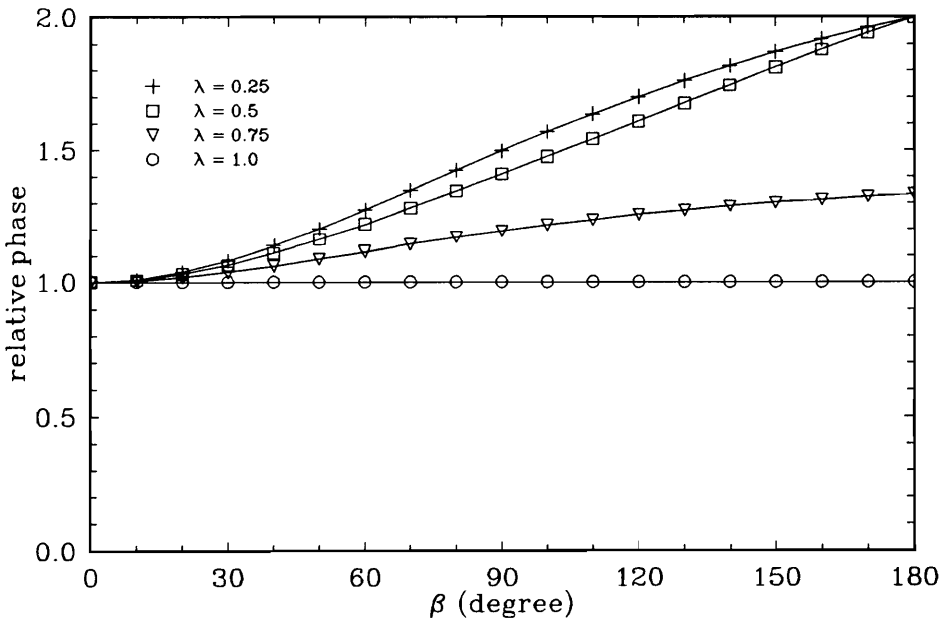

(b) relative phase, $\phi/(-\beta\lambda)$

Figure 2. Amplification factor of 2nd order upwind scheme

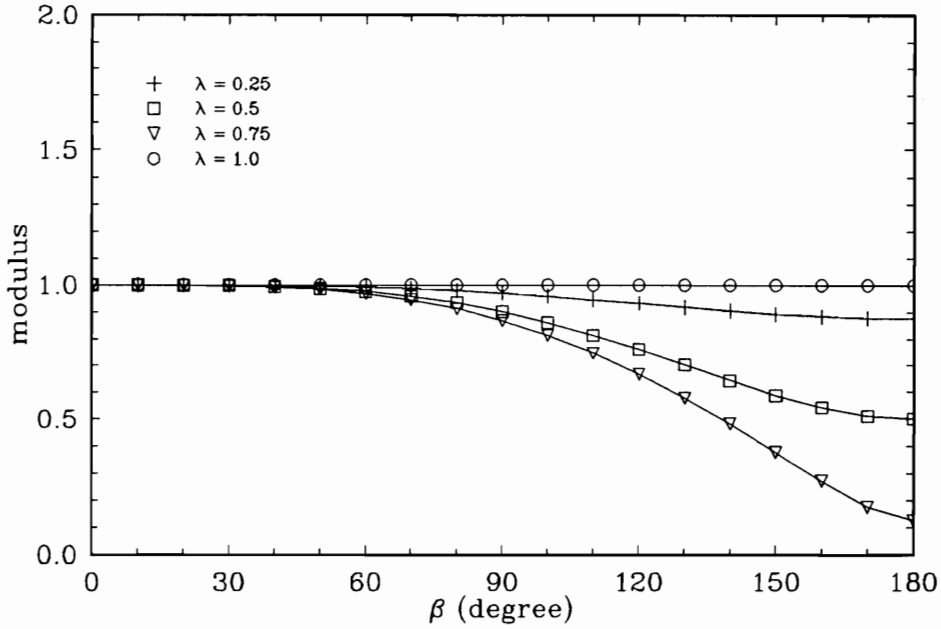

(a) modulus, $|G|$

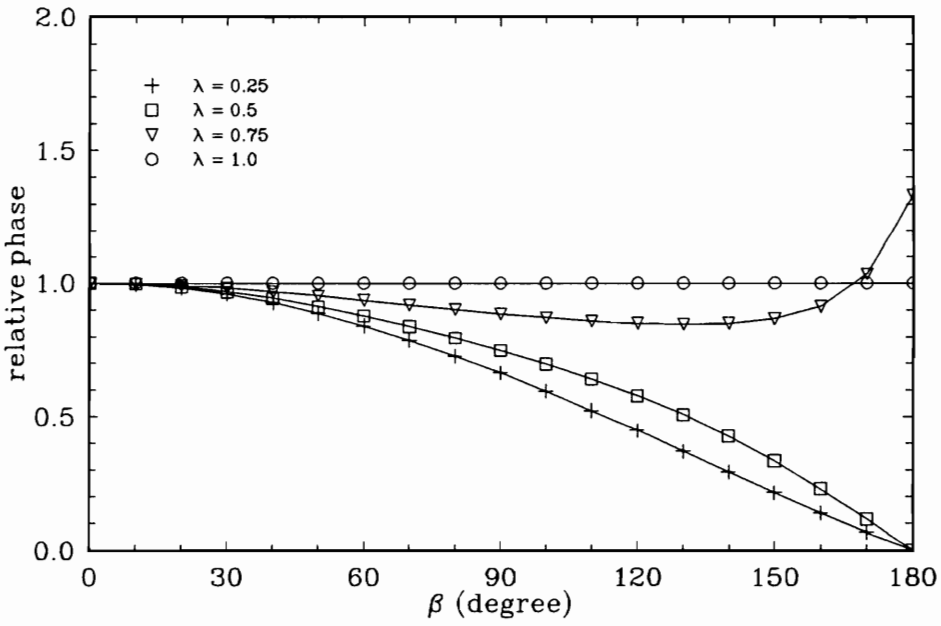

(b) relative phase, $\phi/(-\beta\lambda)$

Figure 3. Amplification factor of Lax-Wendroff scheme

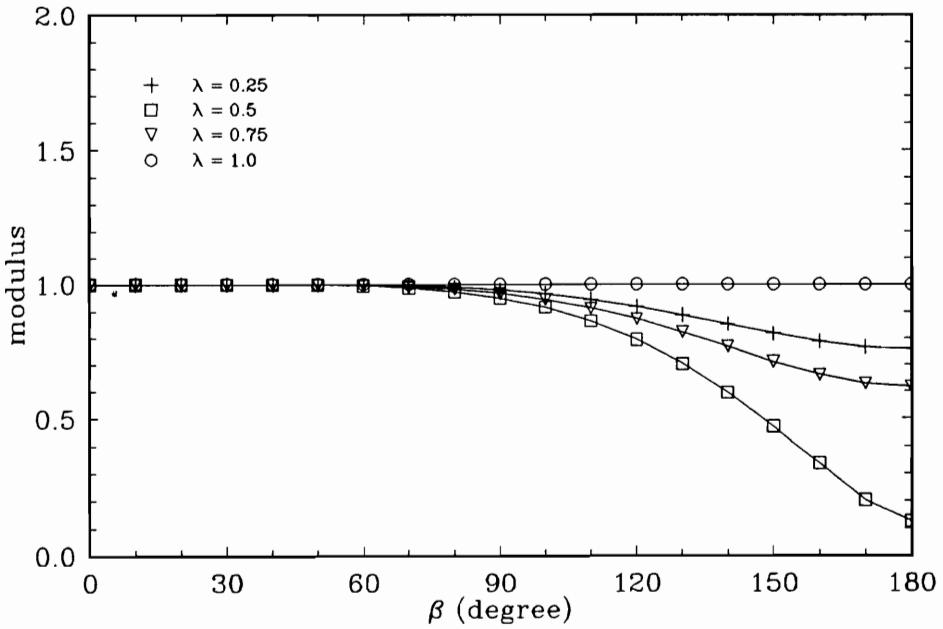

(a) modulus, $|G|$

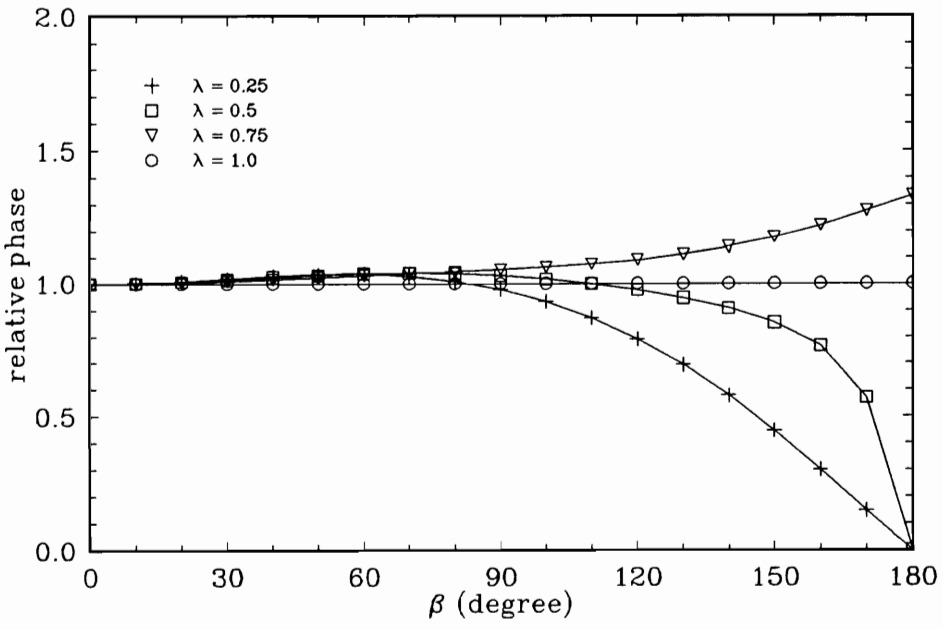

(b) relative phase, $\phi/(-\beta\lambda)$

Figure 4. Amplification factor of modified Lax-Wendroff scheme

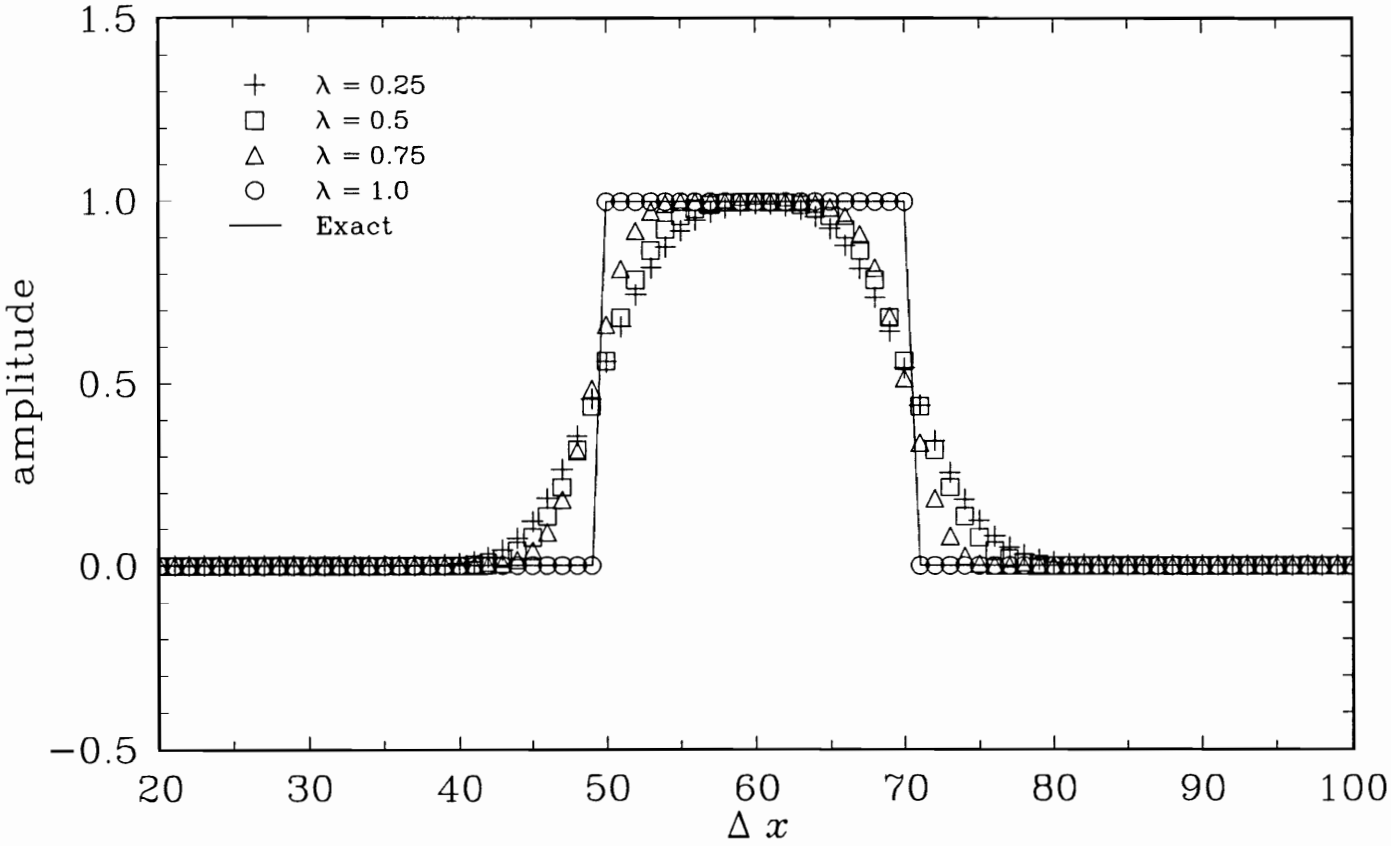

Figure 5. Square wave test for 1st order upwind scheme

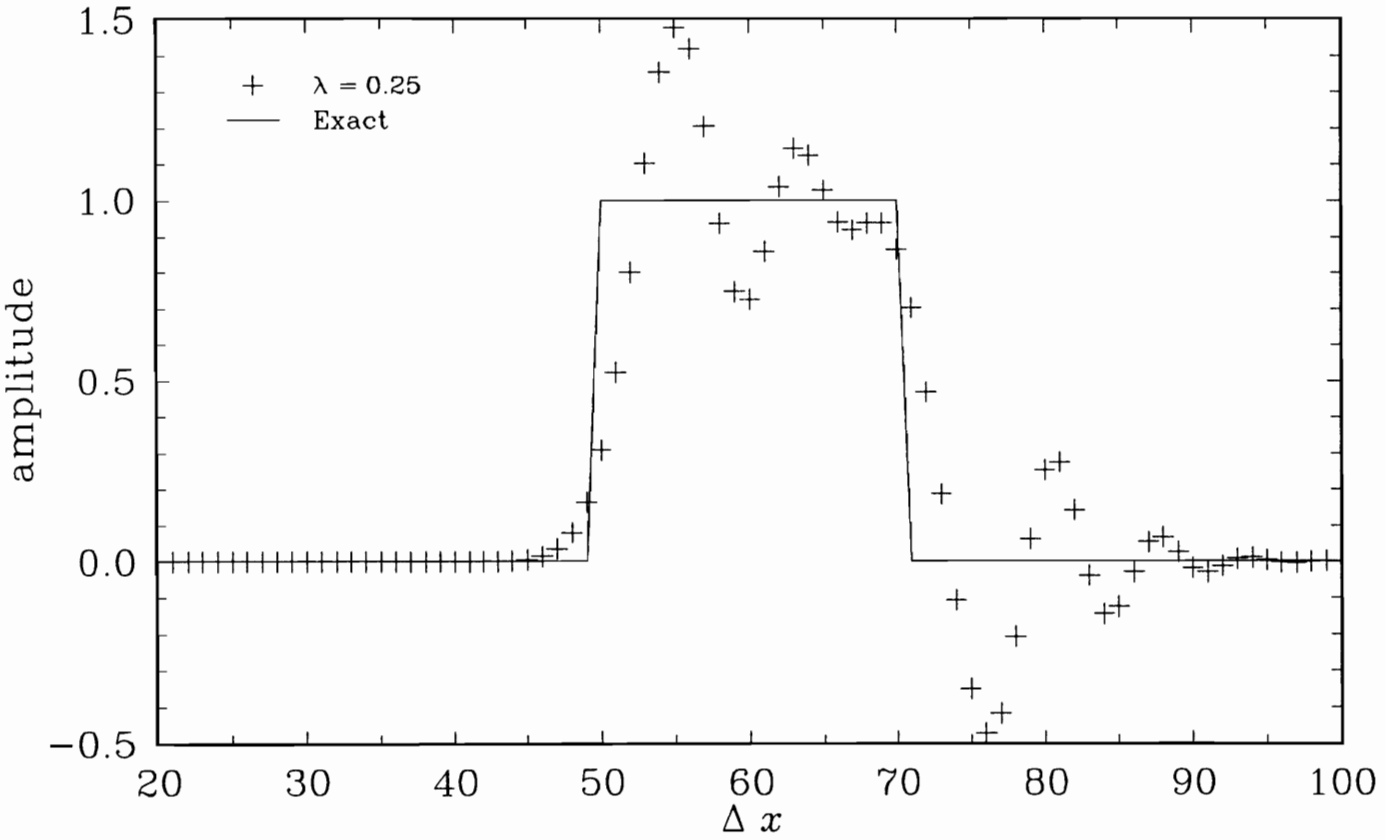

Figure 6. Square wave test for 2nd order upwind scheme

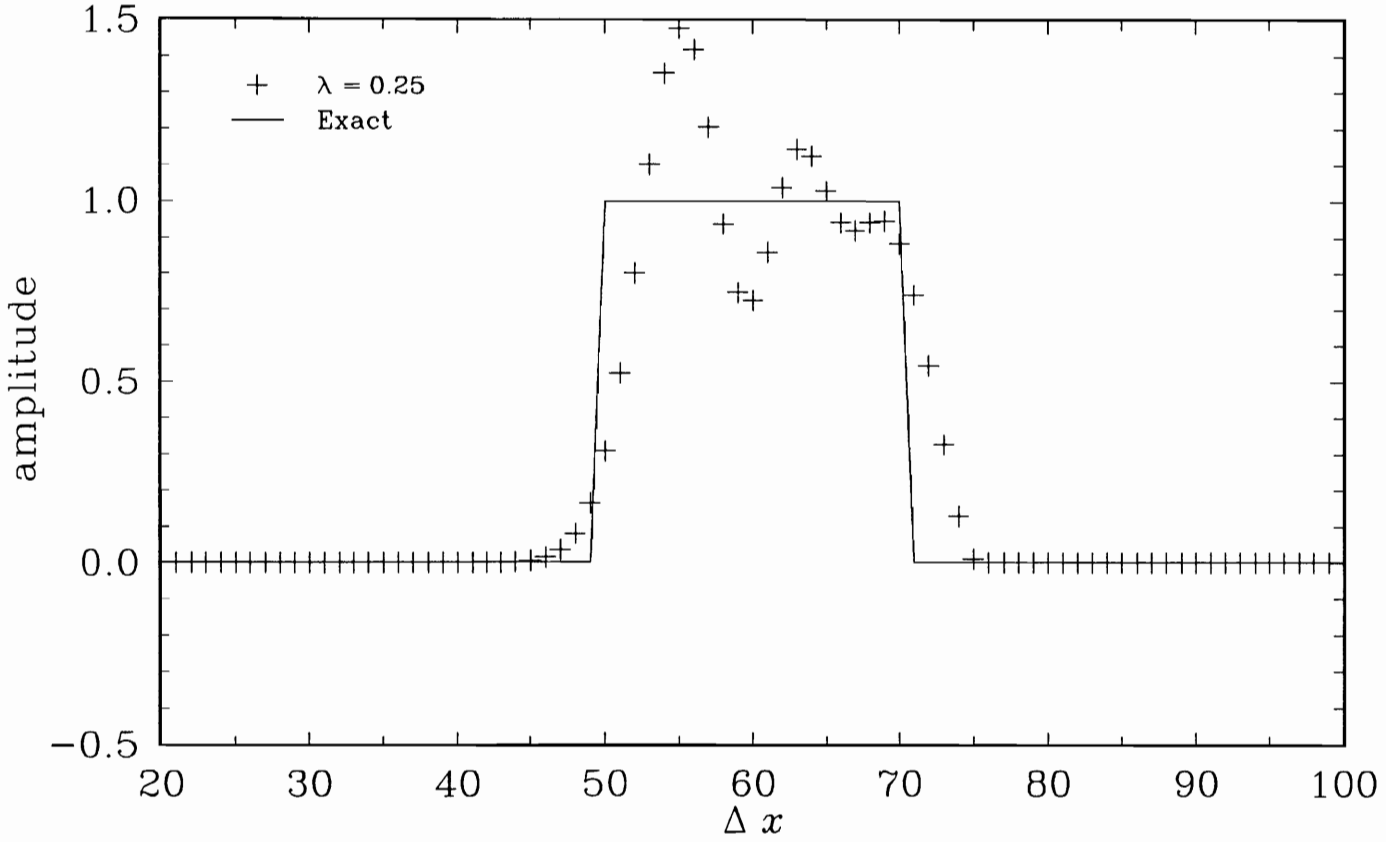

Figure 7. Square wave test for 2nd order upwind scheme with non-negative correction

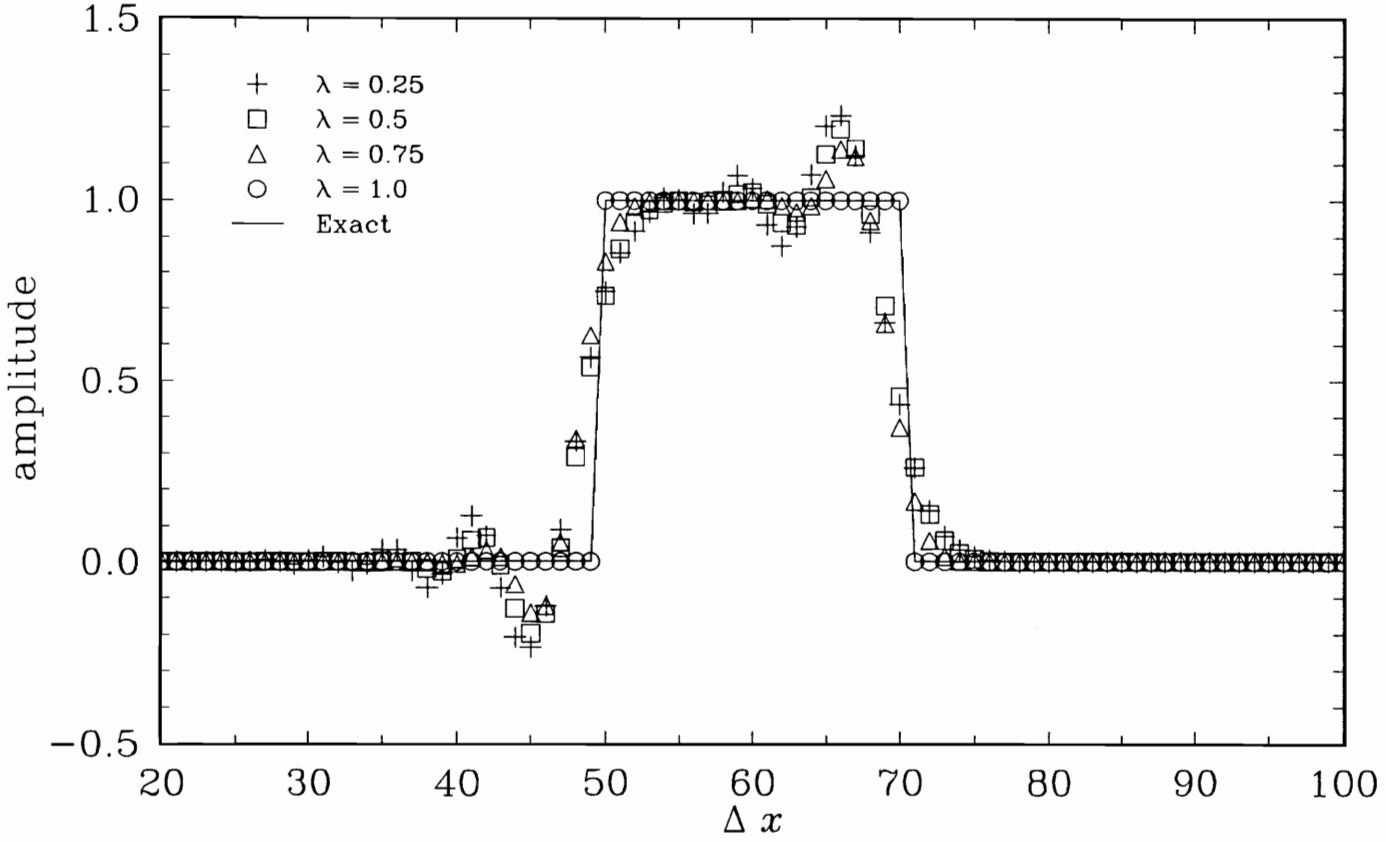

Figure 8. Square wave test for Lax-Wendroff scheme

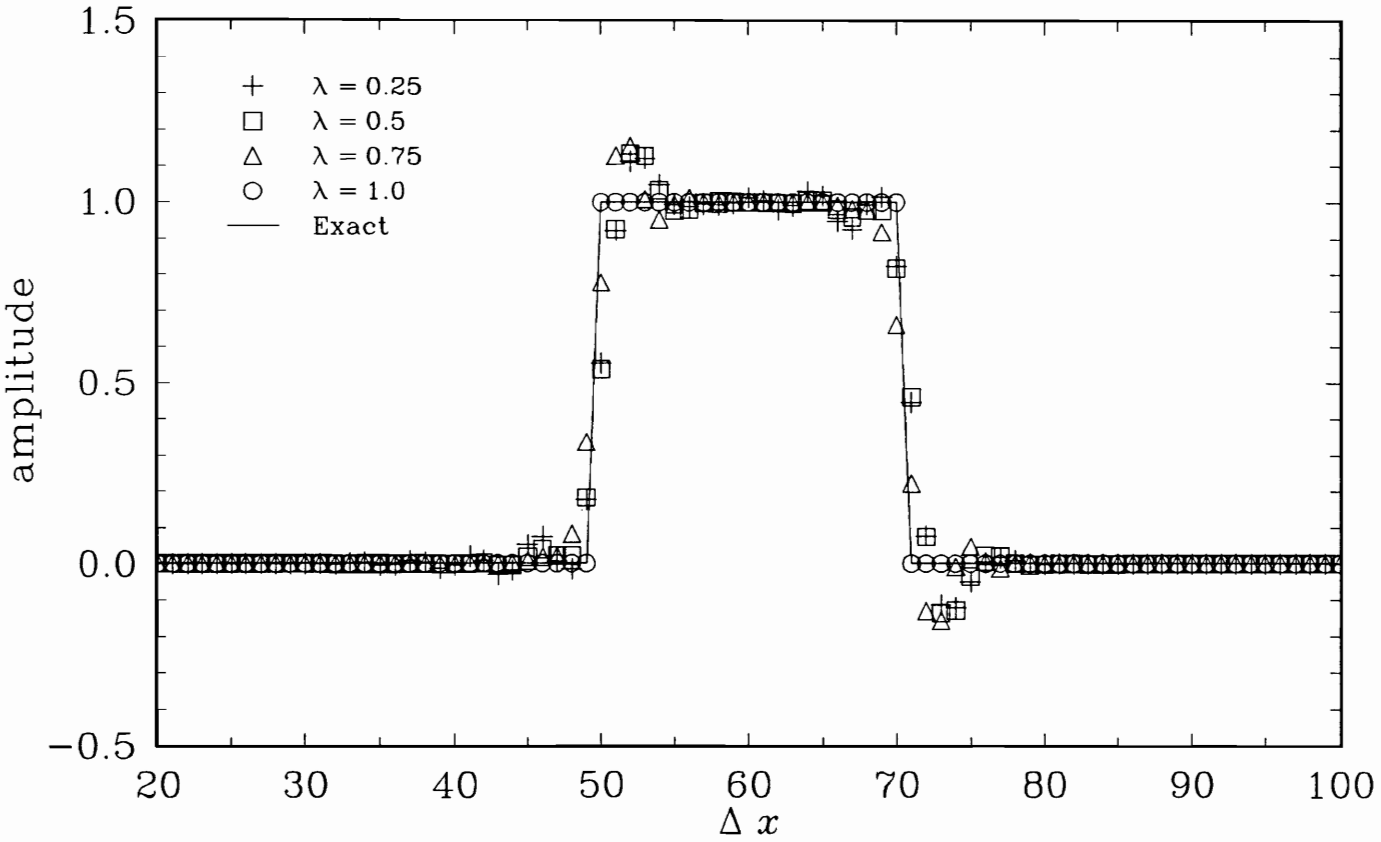

Figure 9. Square wave test for modified Lax-Wendroff scheme

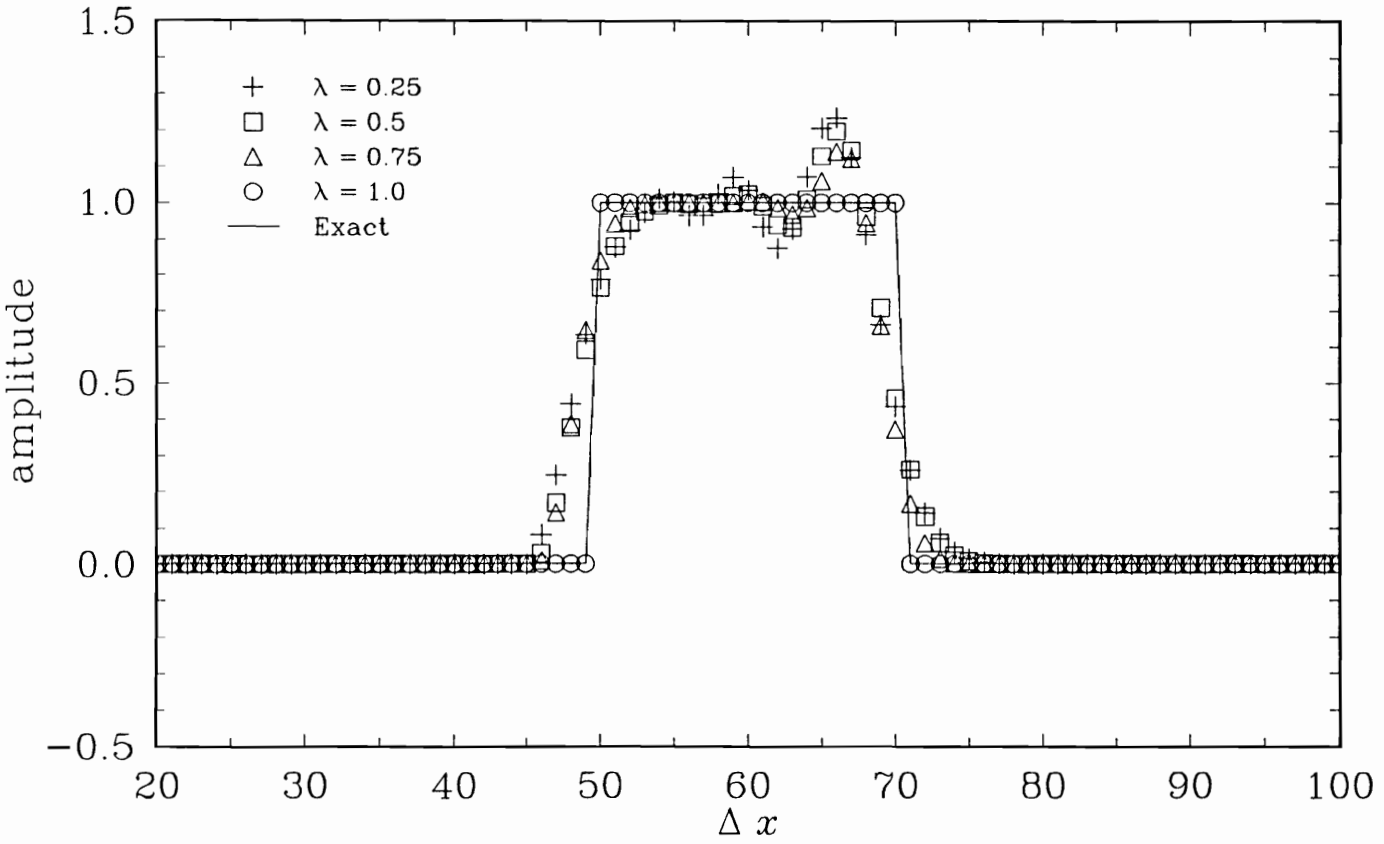

Figure 10. Square wave test for Lax-Wendroff scheme with non-negative correction

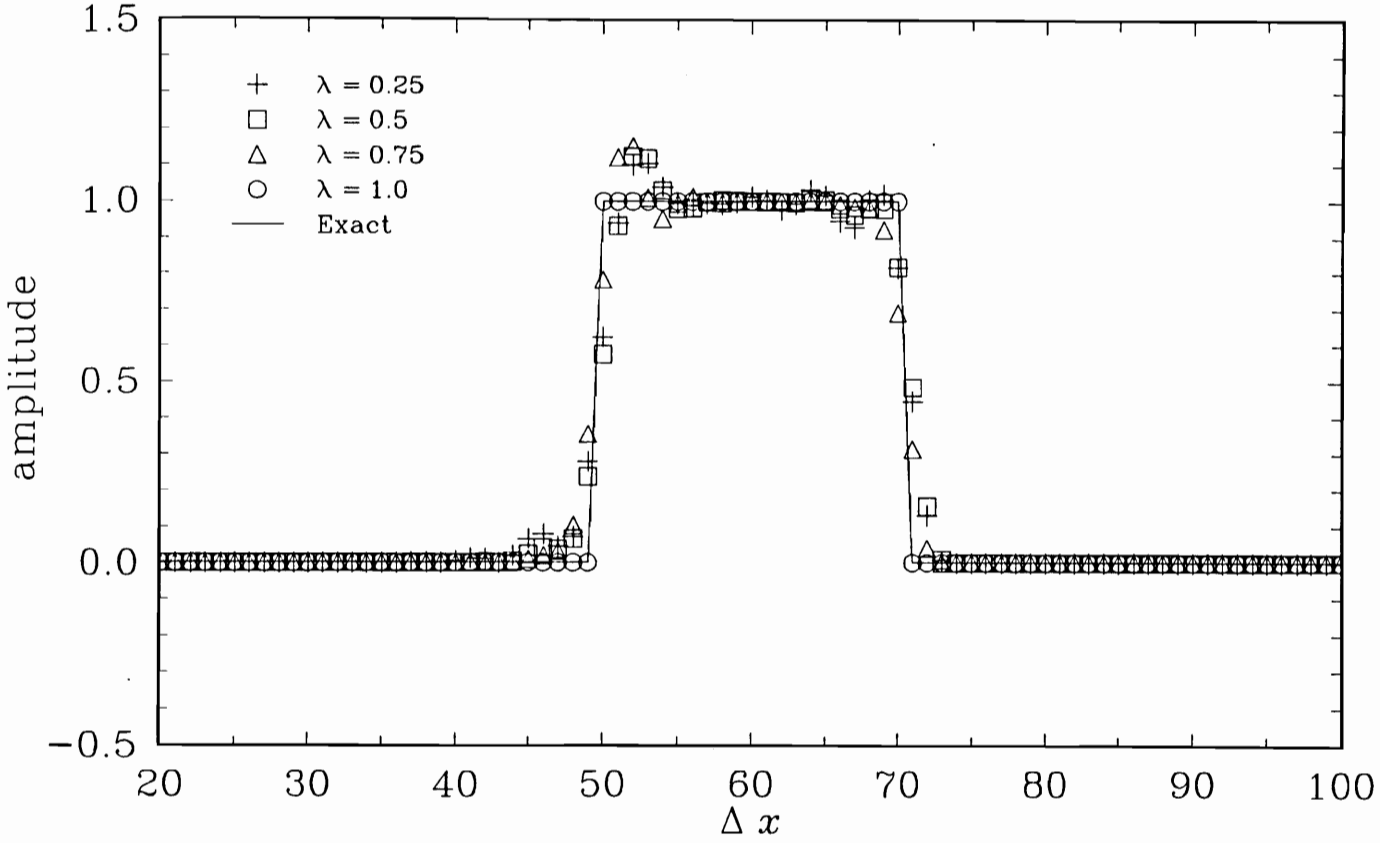

Figure 11. Square wave test for modified Lax-Wendroff scheme with non-negative correction

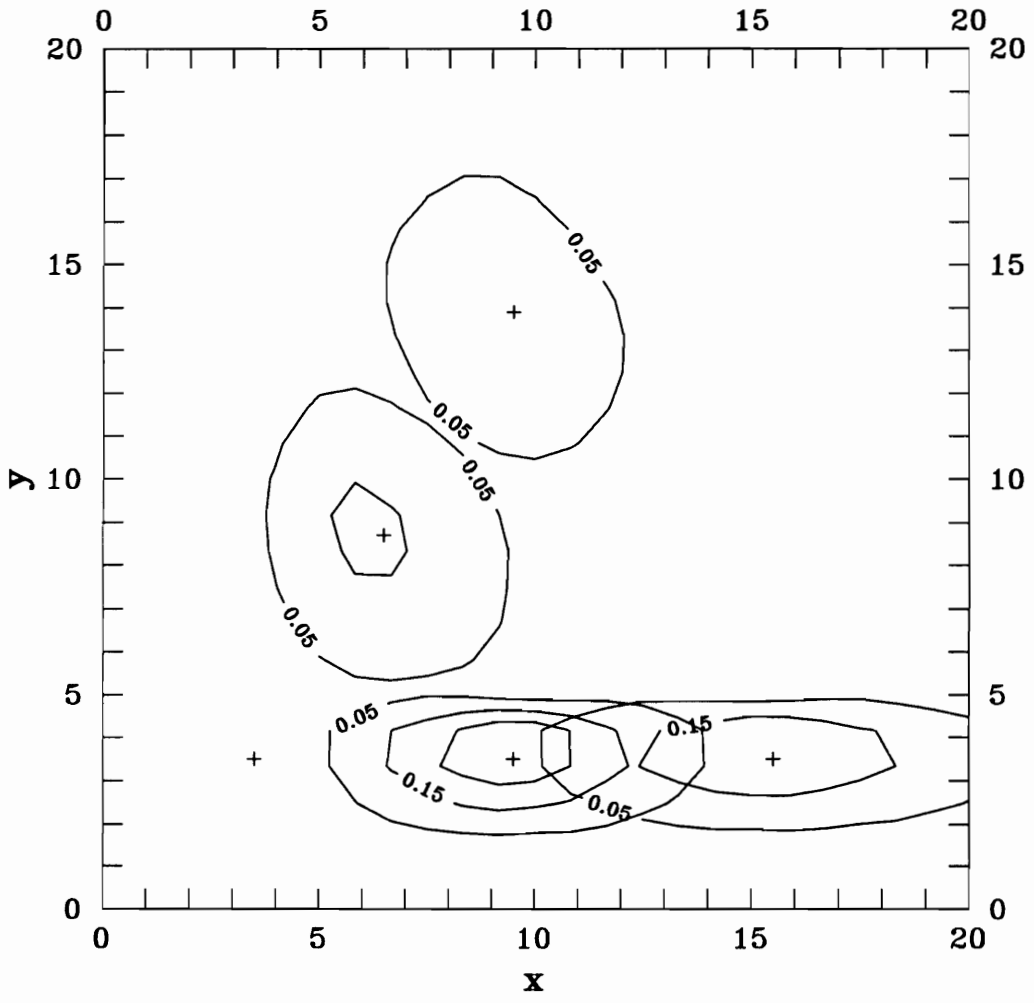

Figure 12. Unit pulse test for 1st order upwind scheme

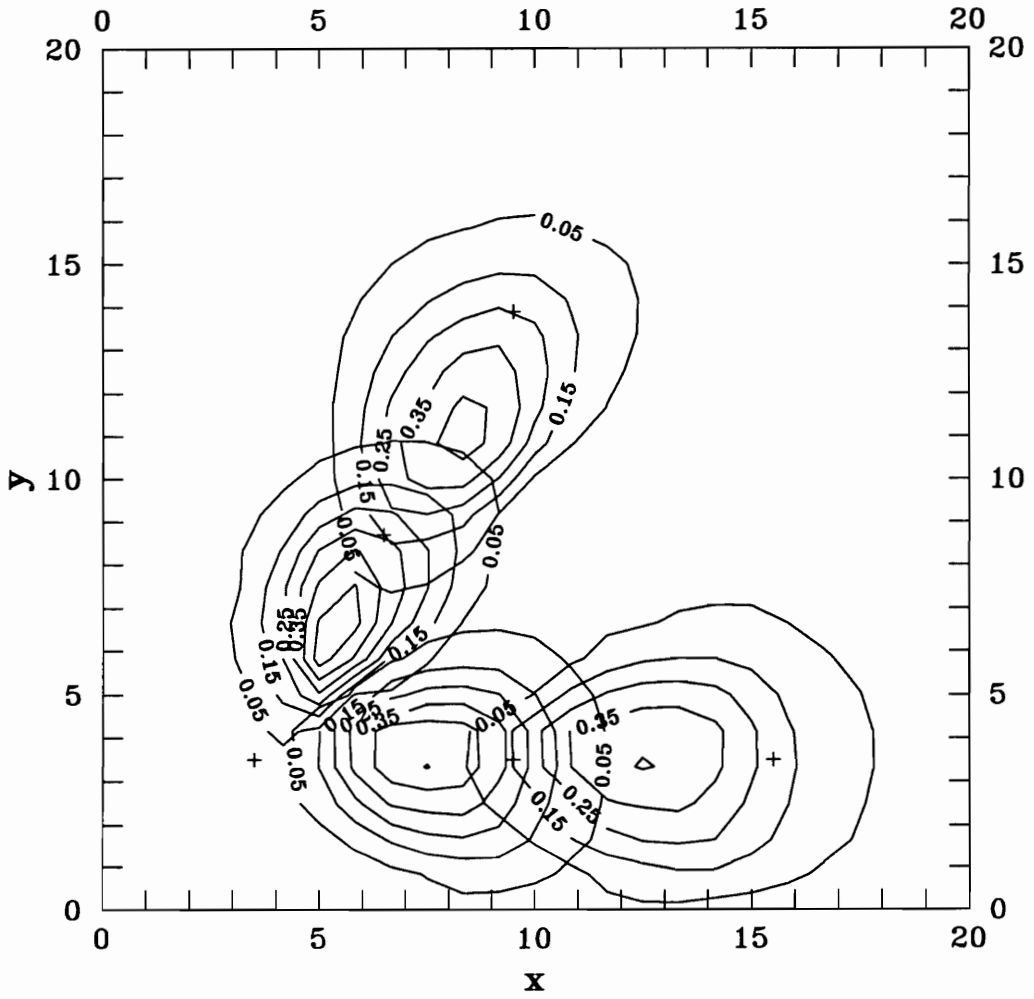

Figure 13. Unit pulse test for Lax-Wendroff scheme

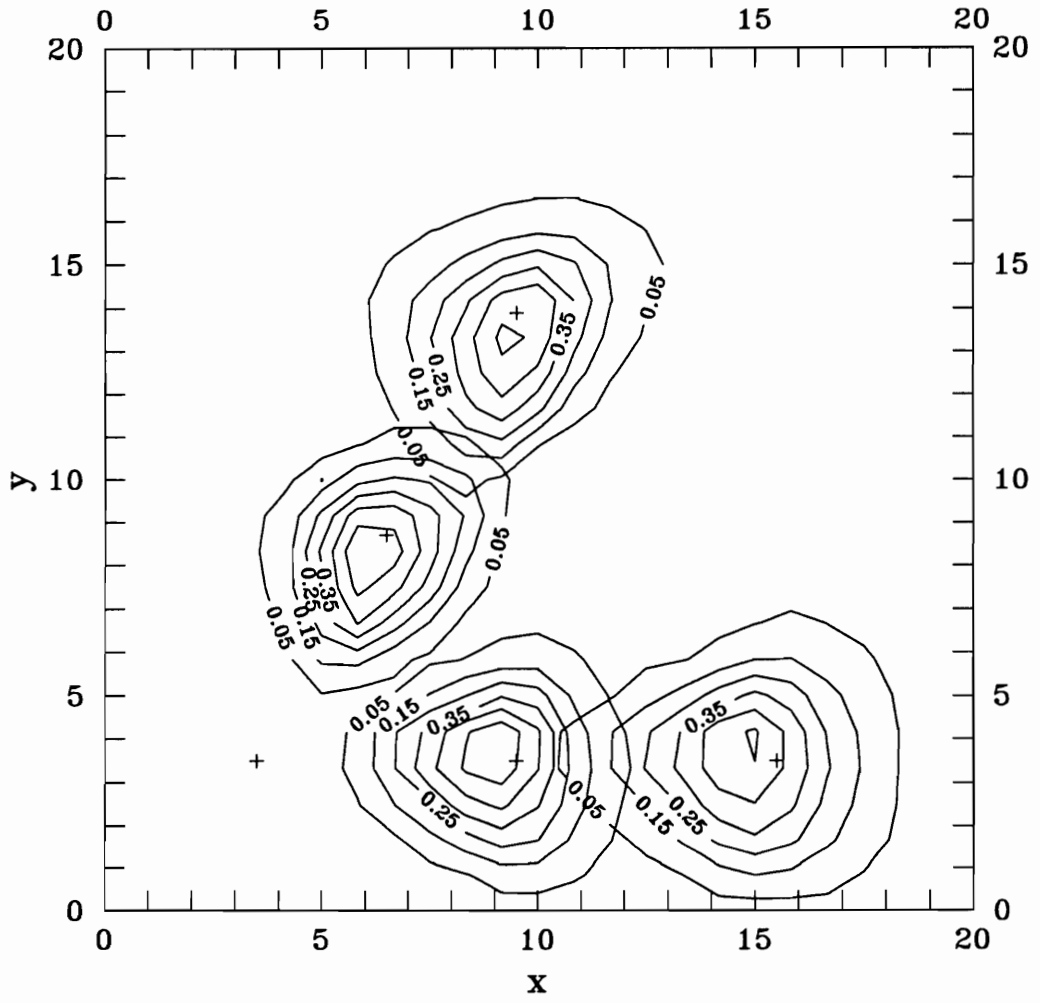

Figure 14. Unit pulse test for modified Lax-Wendroff scheme

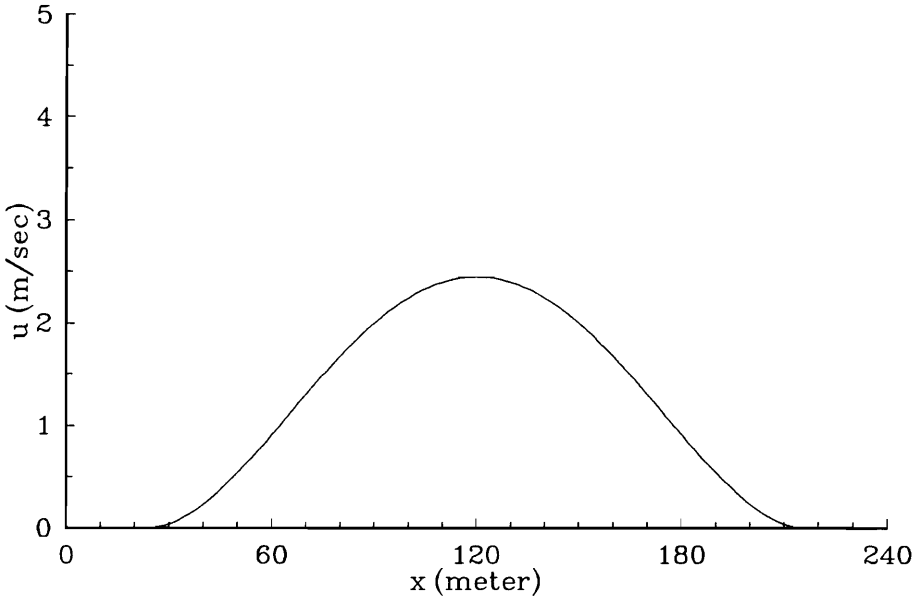

Figure 15. Current distribution

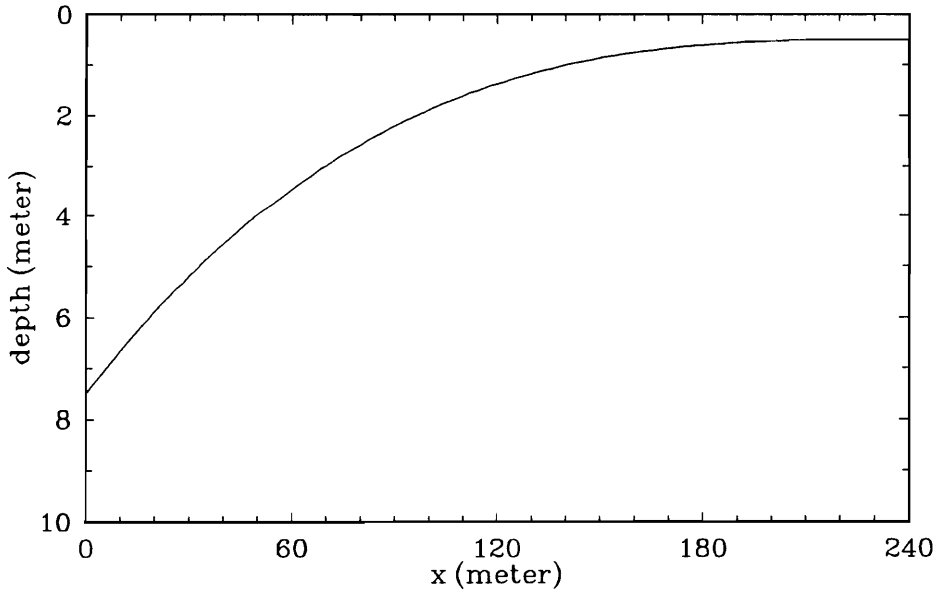

Figure 16. Depth distribution

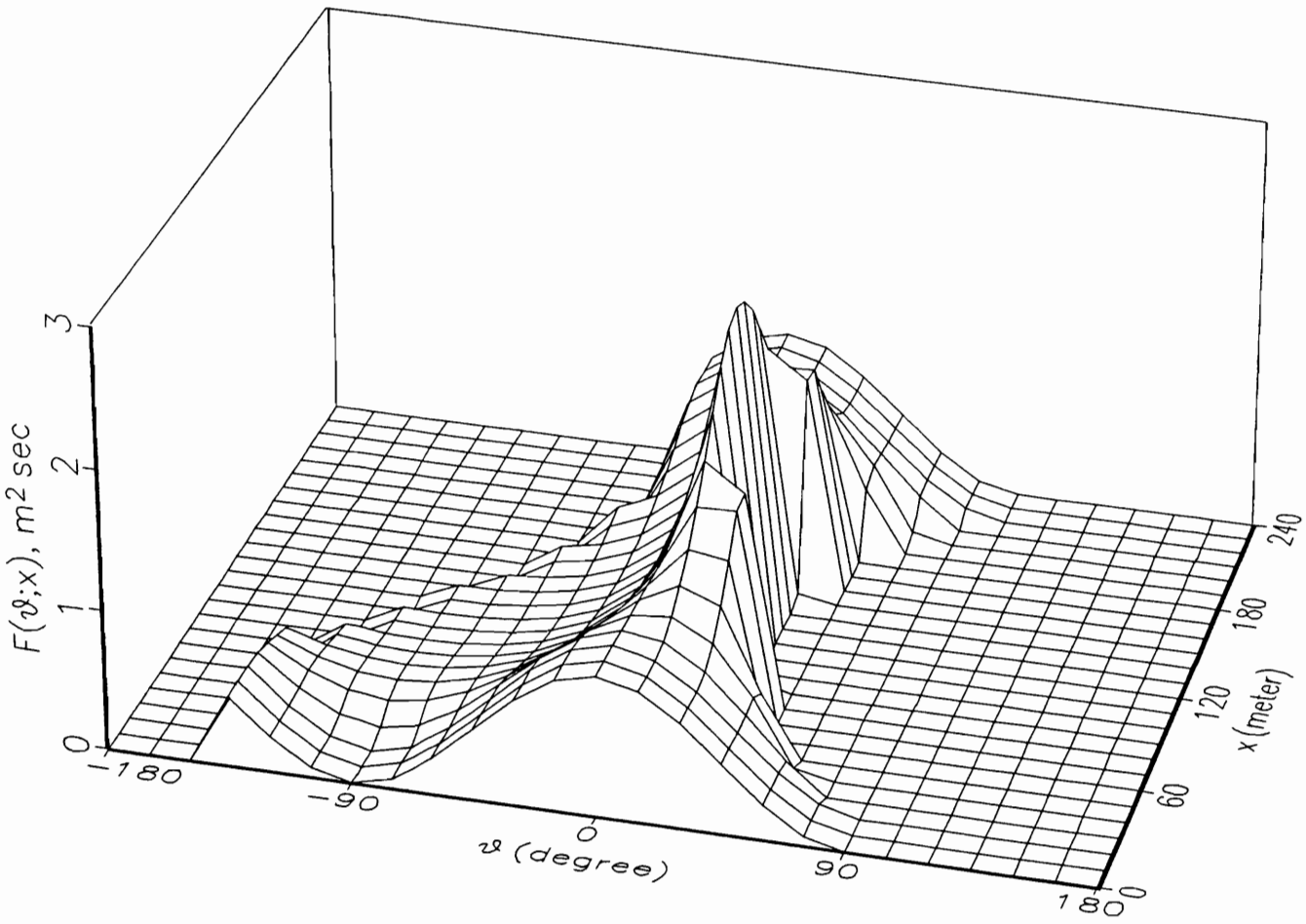

Figure 17. Analytic solution for Case 1; current refraction only, deep water

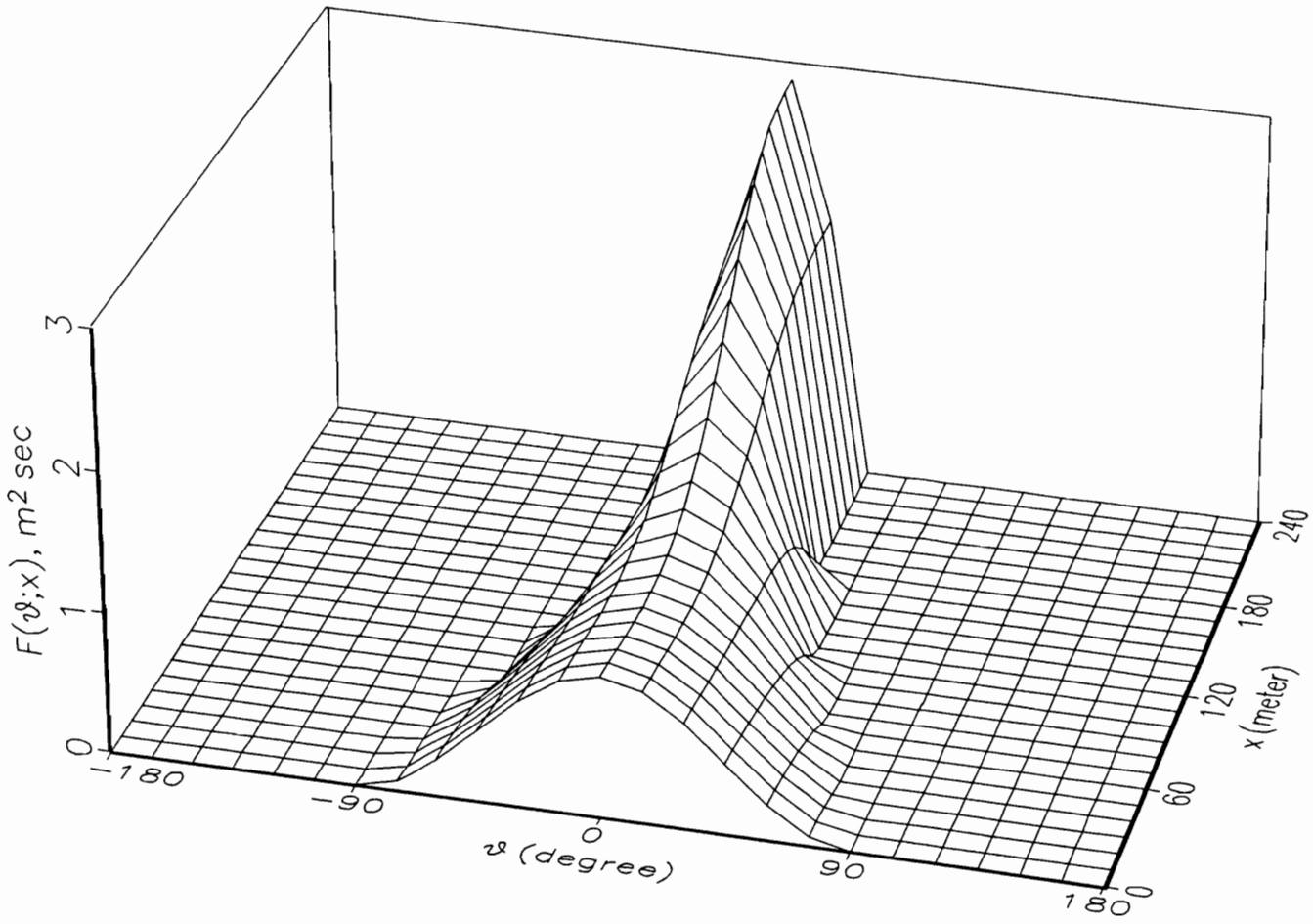

Figure 18. Analytic solution for Case 2; depth refraction only, no current

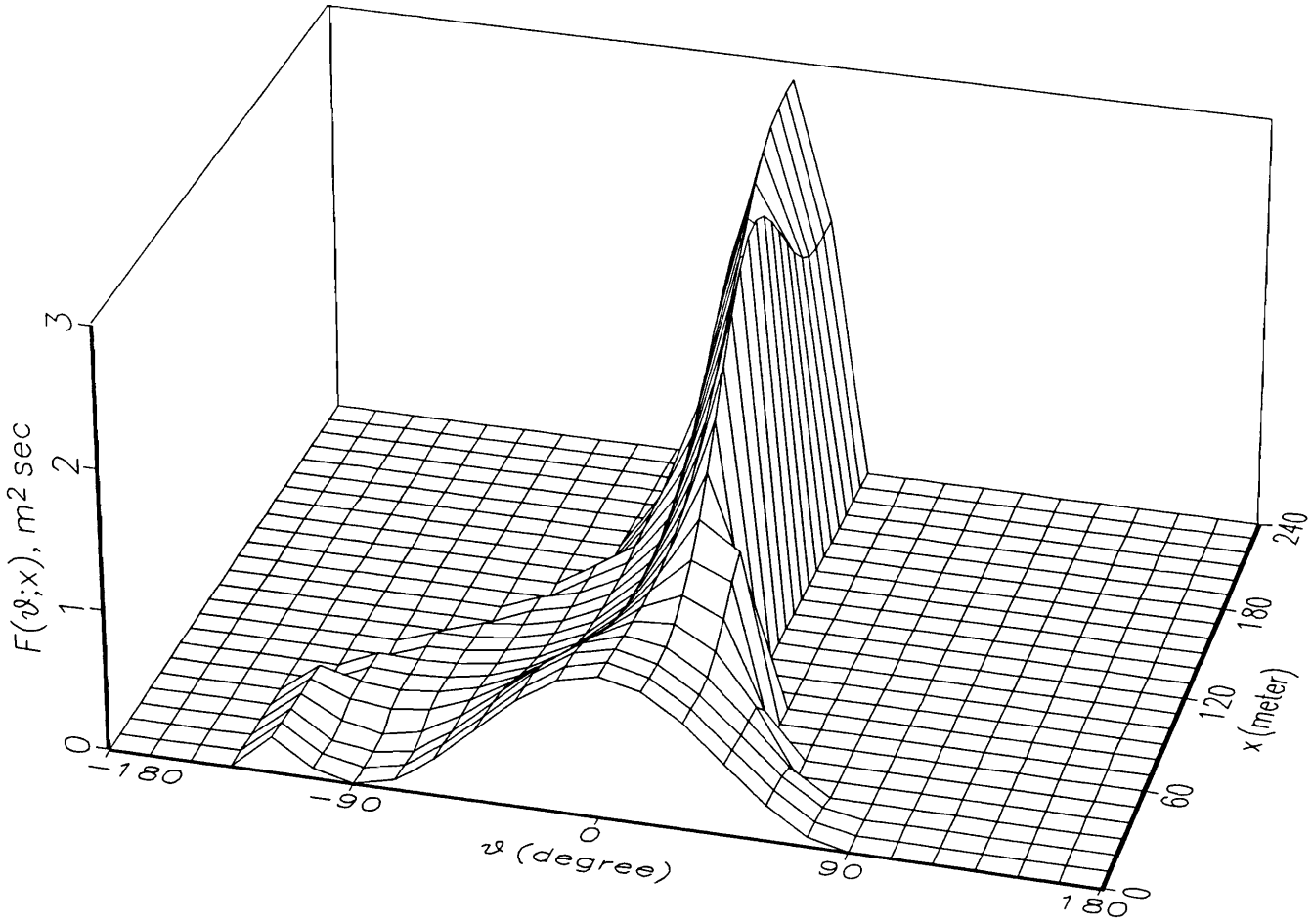

Figure 19. Analytic solution for Case 3; both depth and current refraction

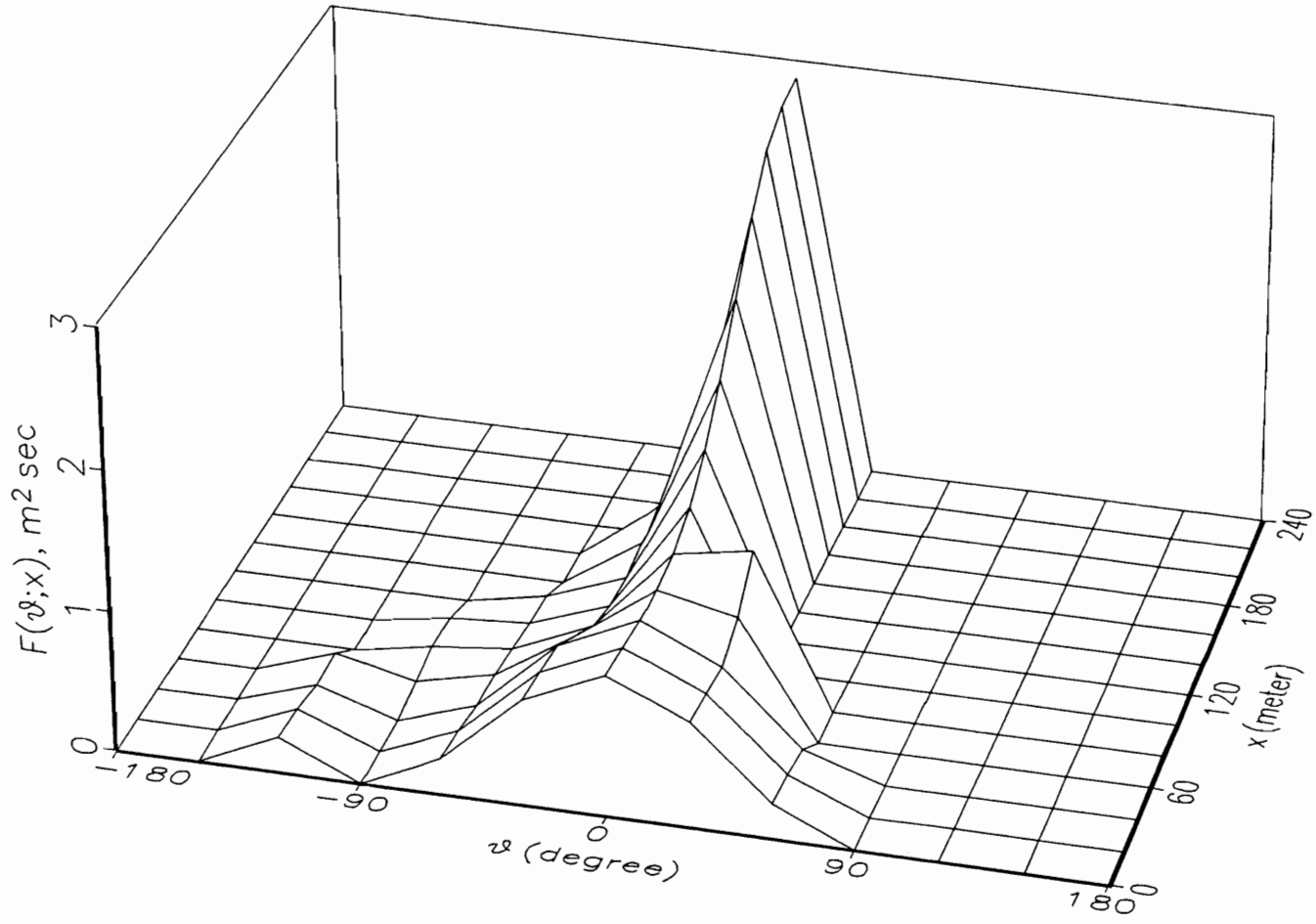

Figure 20. Analytic solution for Case 3; in a coarser grid (12 × 12)

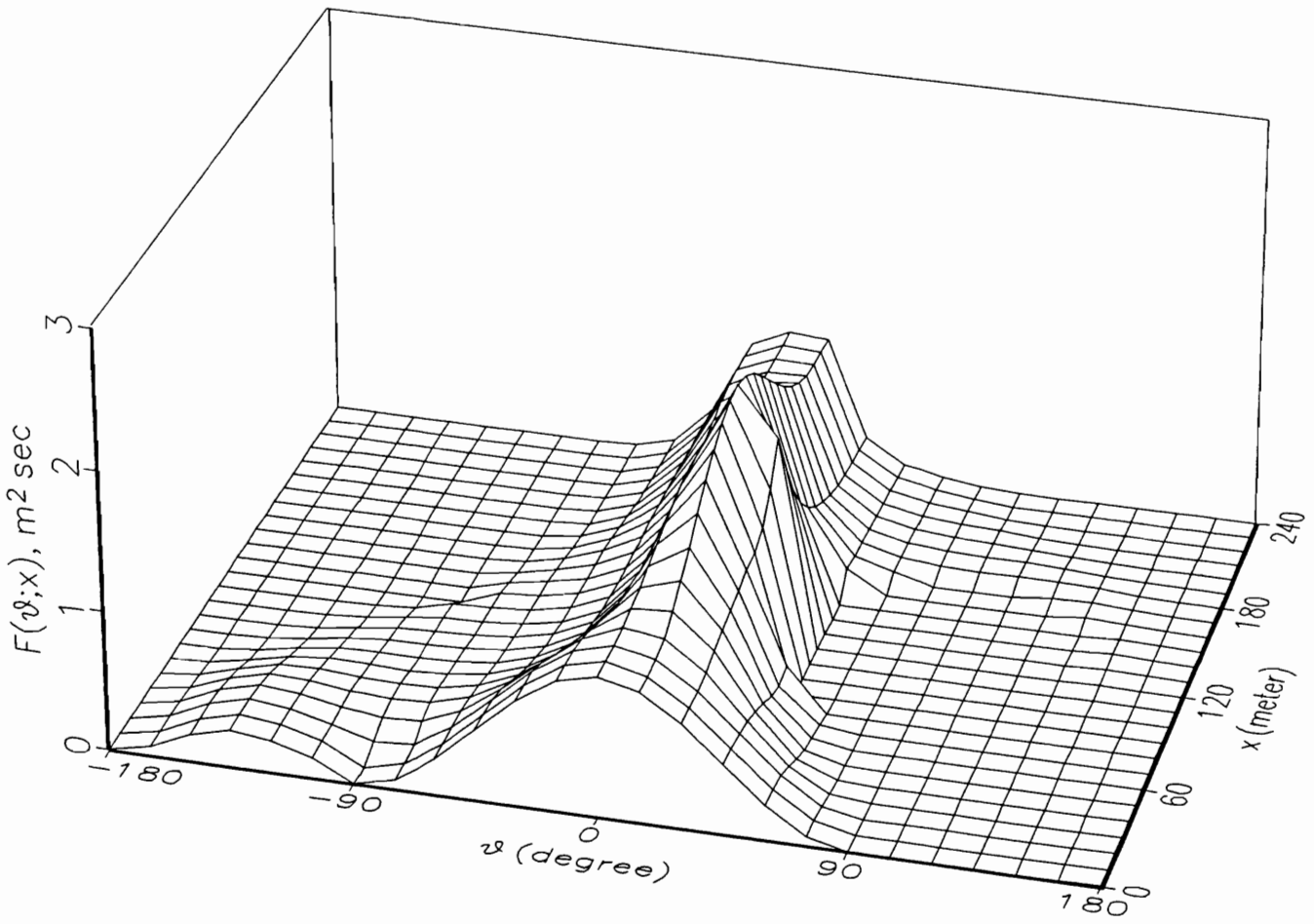

Figure 21. Case 1 - 24 × 24 grid; UP1C in x, UP1C in θ

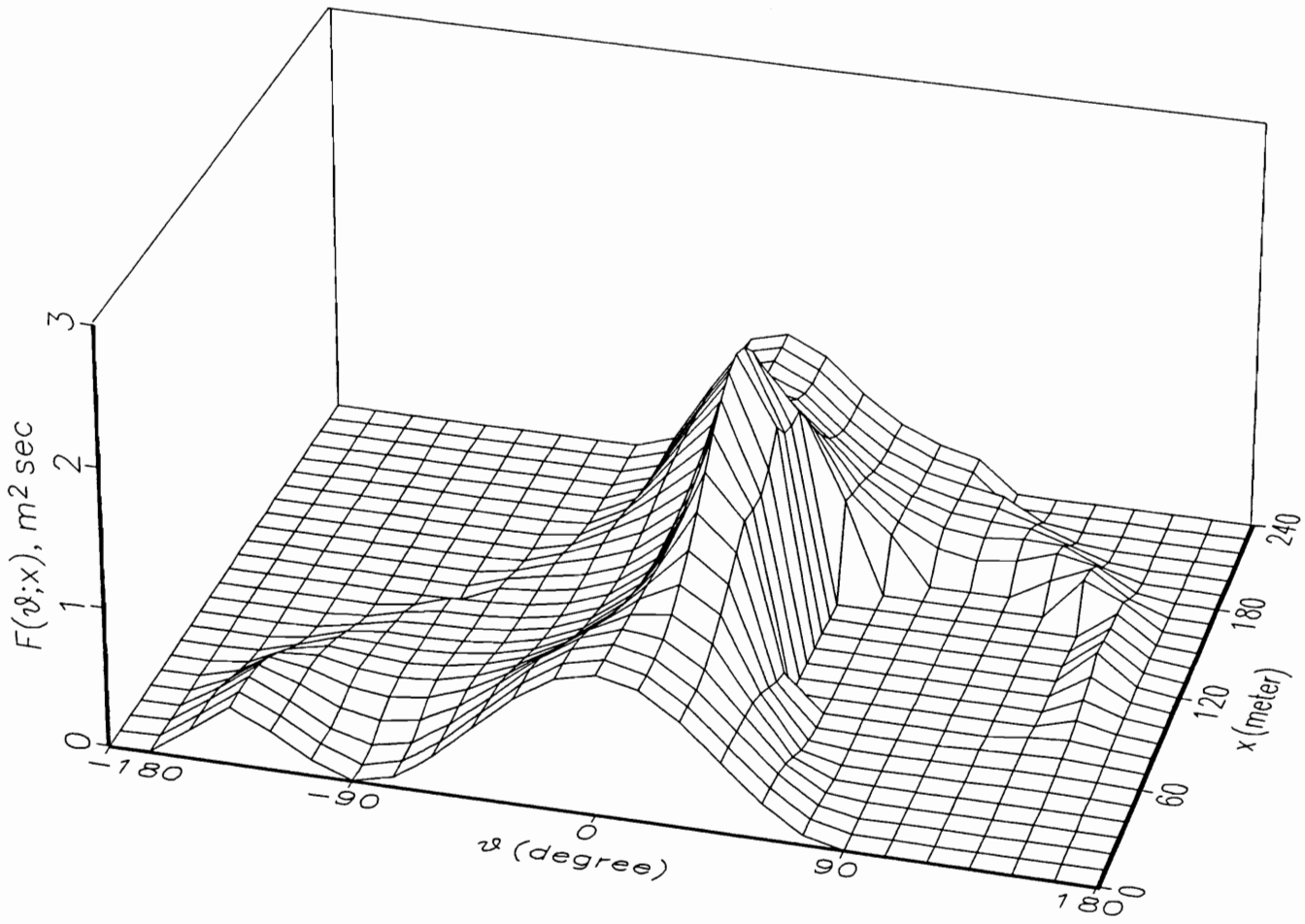

Figure 22. Case 1 - 24 × 24 grid; UP2C in x, UP2N in θ

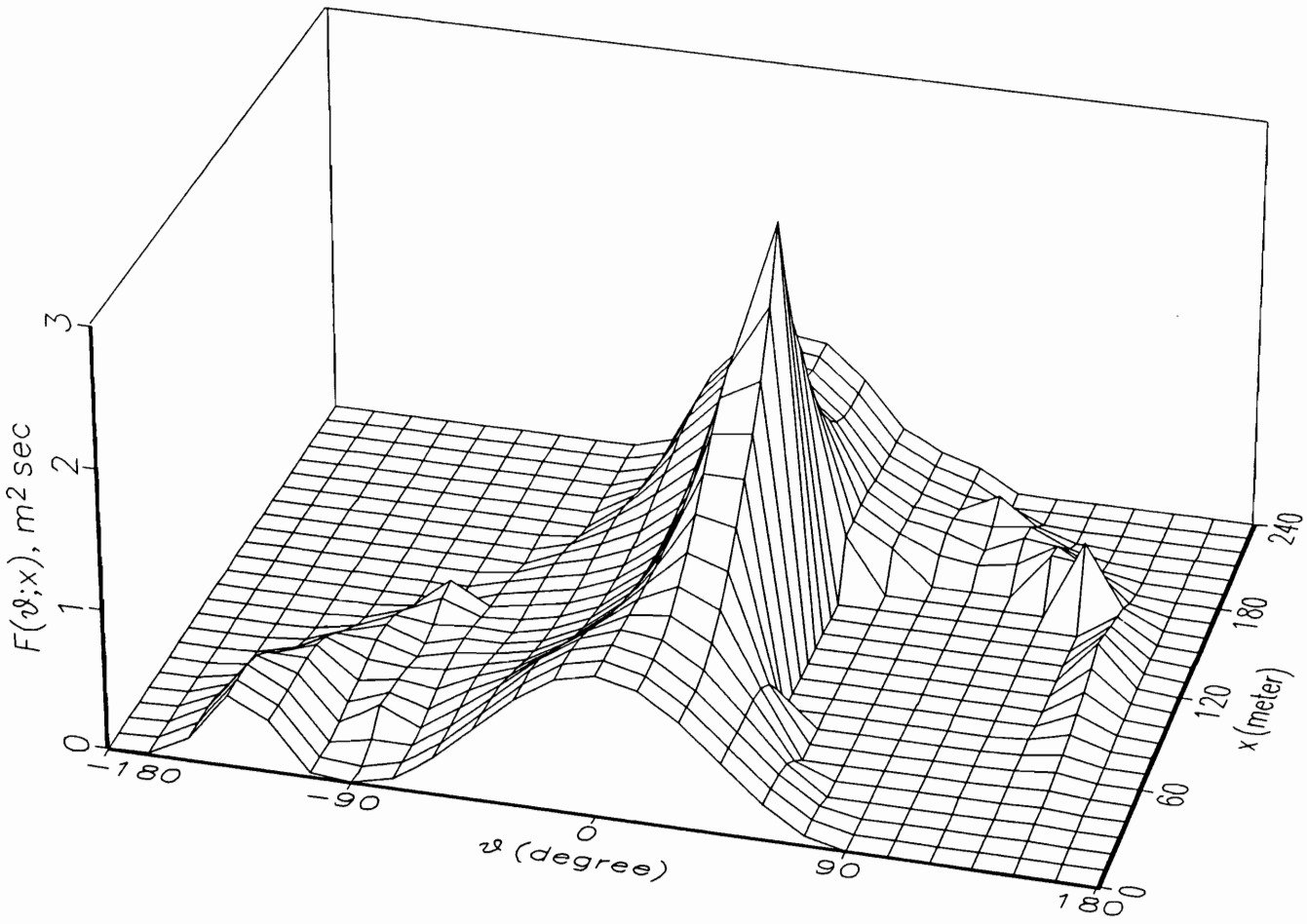

Figure 23. Case 1 - 24 × 24 grid; UP2C in x, LW in θ

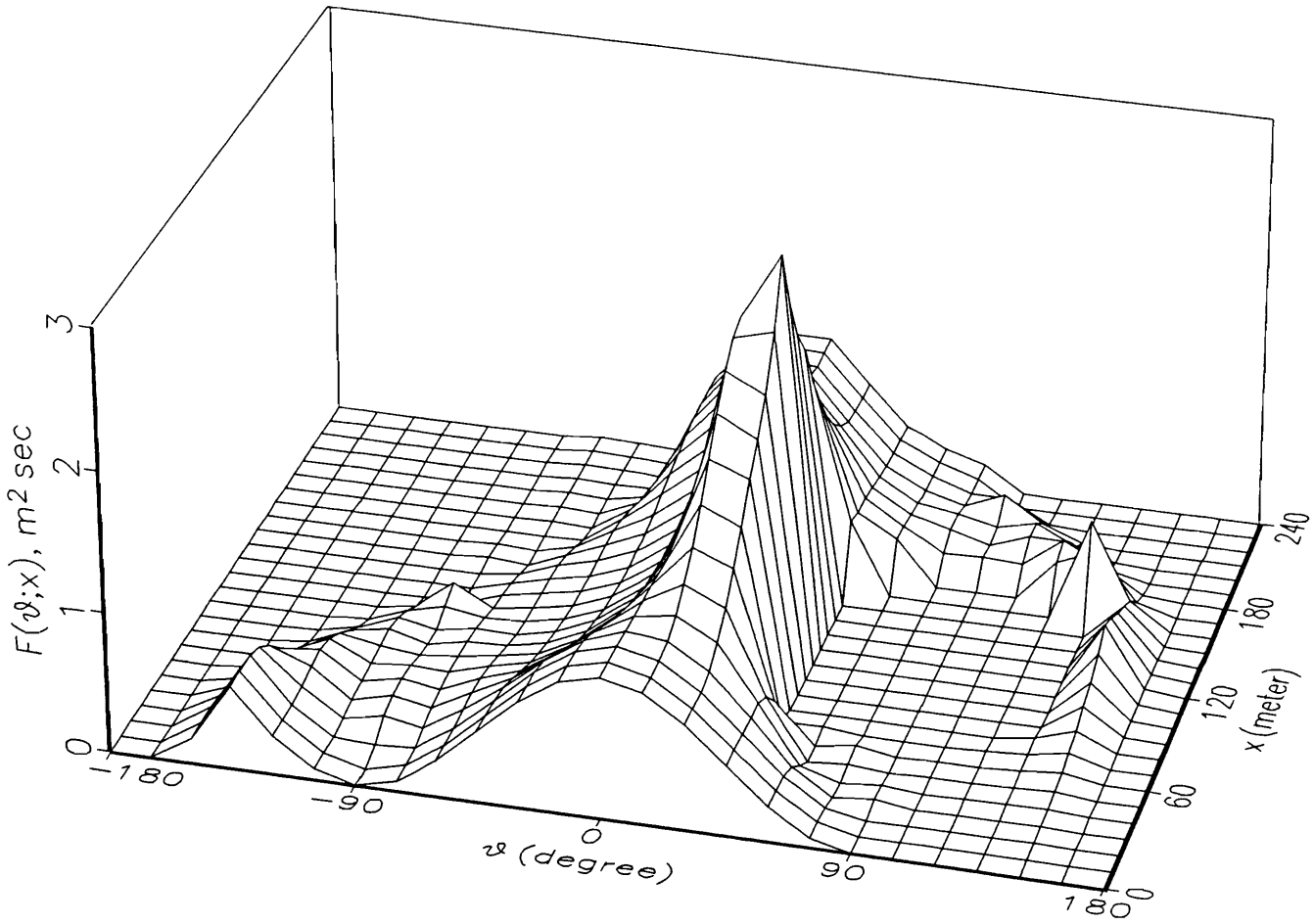

Figure 24. Case 1 - 24 × 24 grid; UP2C in x, LWG in θ

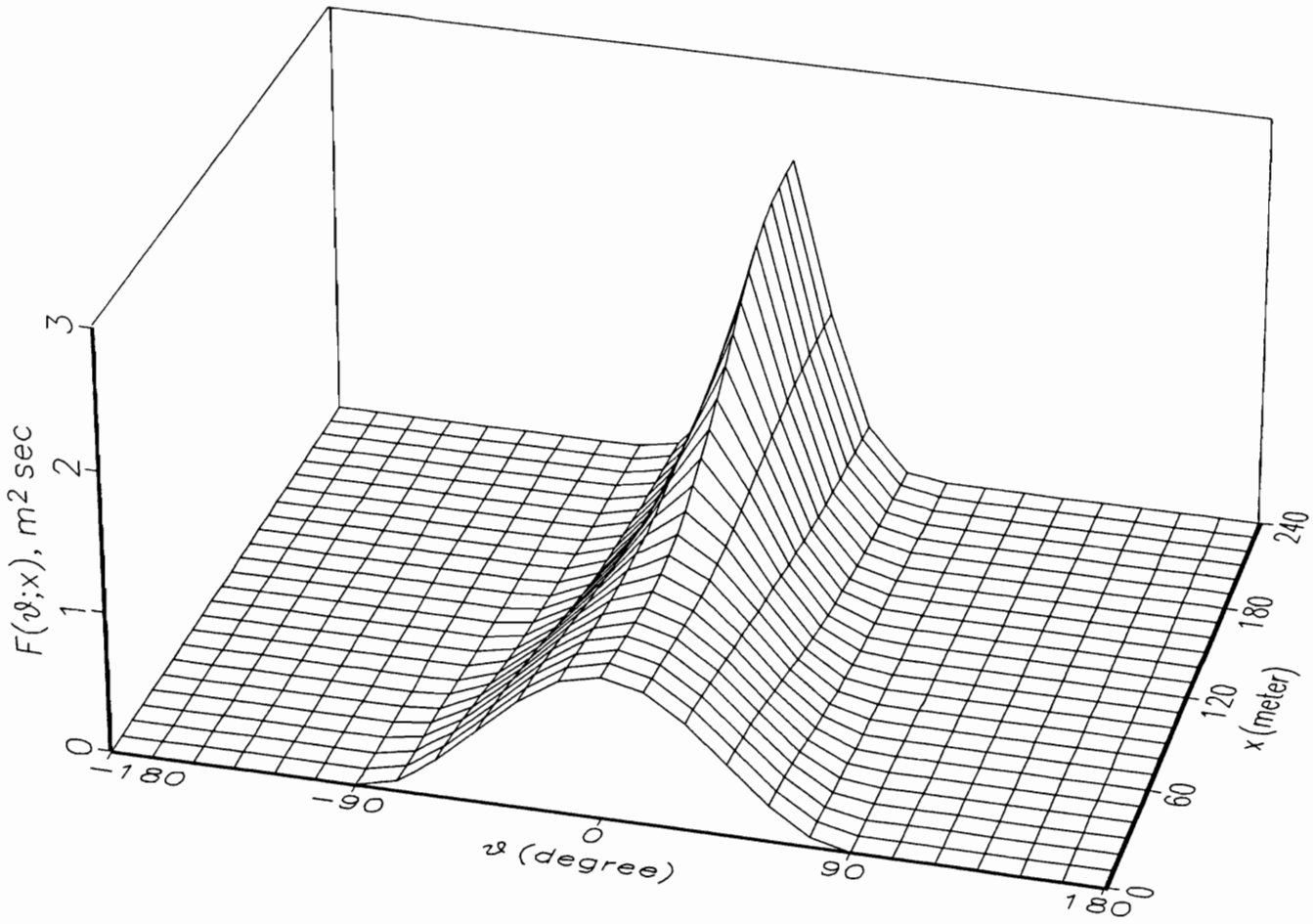

Figure 25. Case 2 - 24 × 24 grid; UP1C in x, UP1C in θ

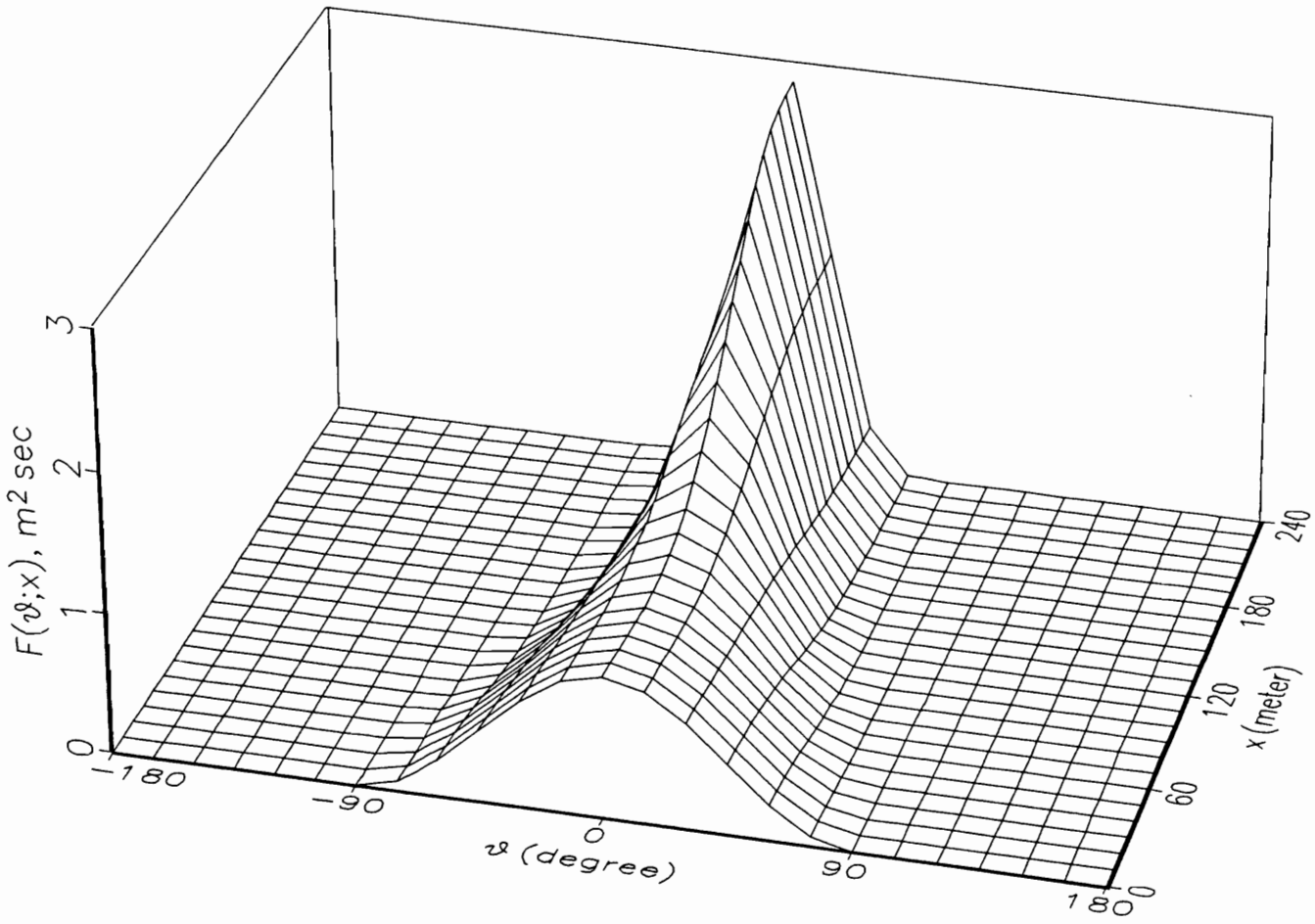

Figure 26. Case 2 - 24 × 24 grid; UP2C in x, UP2N in θ

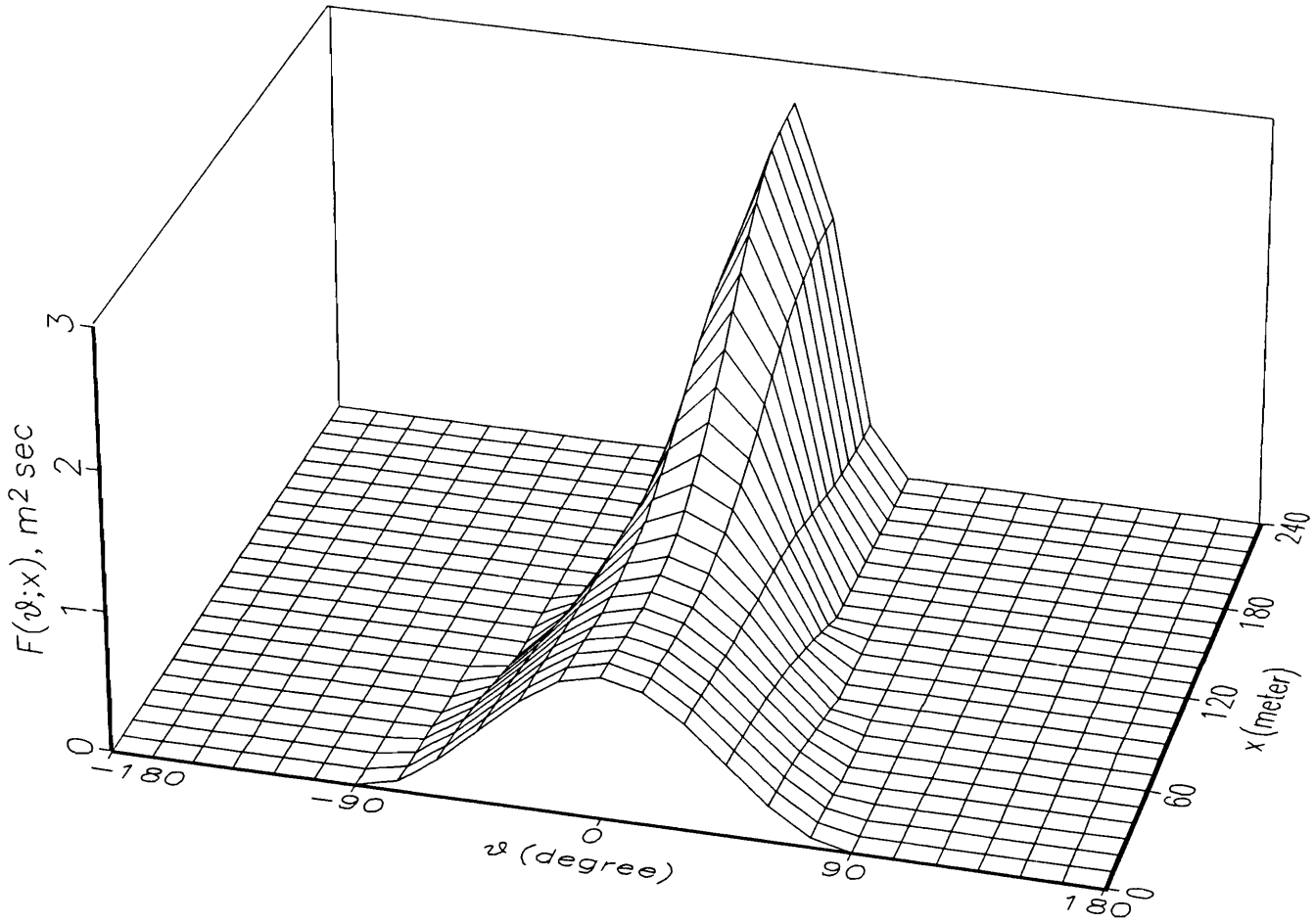

Figure 27. Case 2 - 24 × 24 grid; UP2C in x, LW in θ

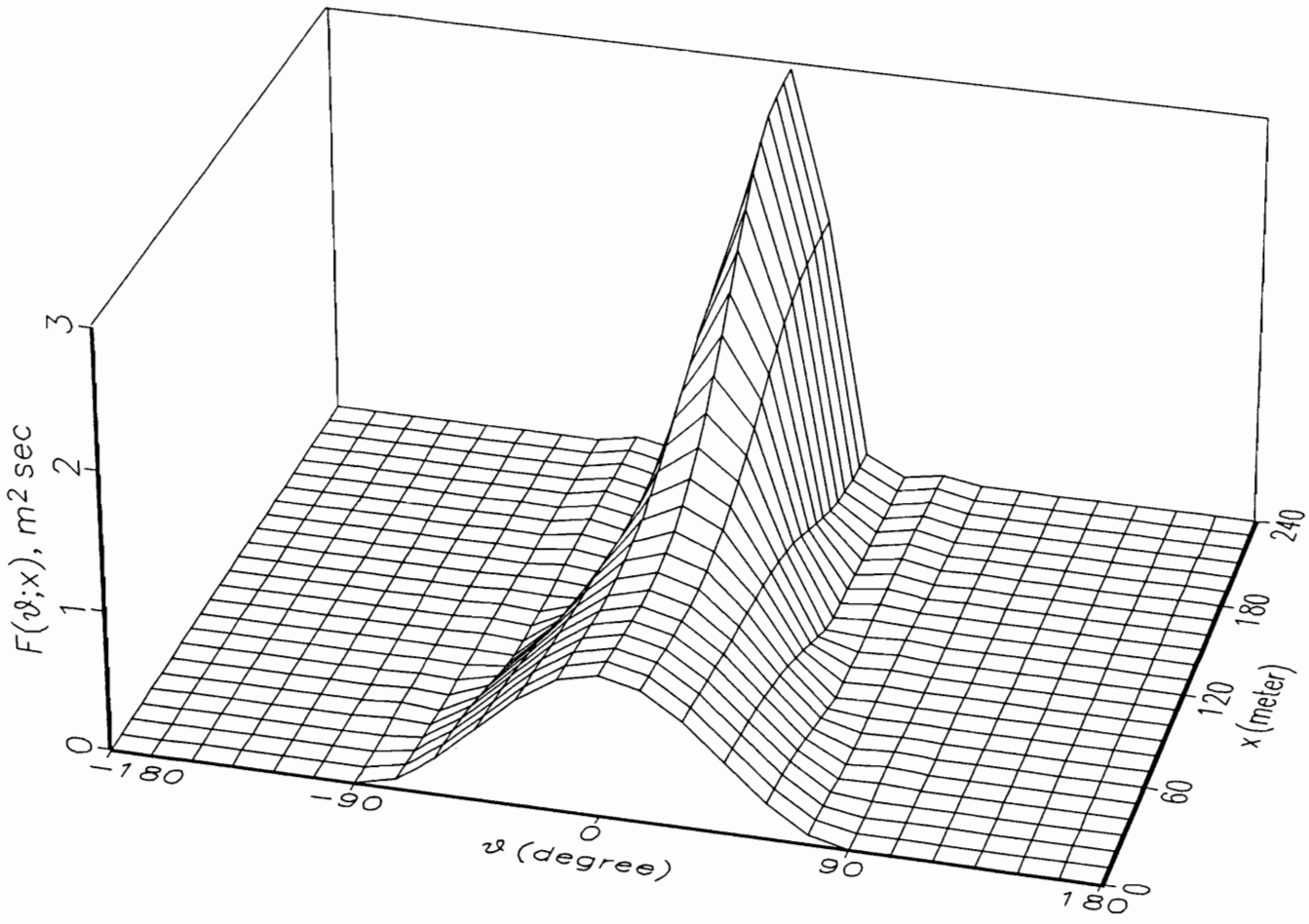

Figure 28. Case 2 - 24 × 24 grid; UP2C in x, LWG in θ

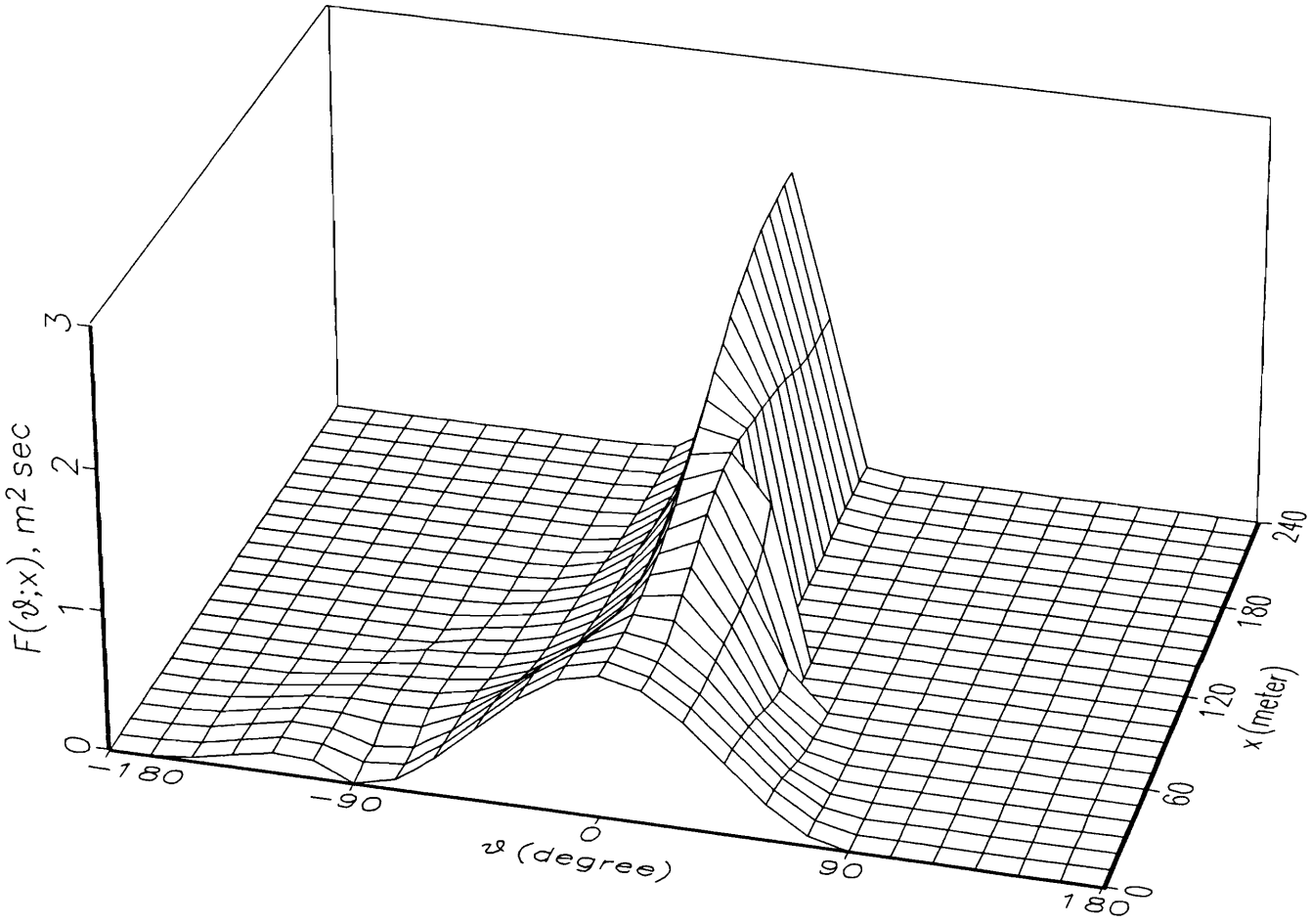

Figure 29. Case 3 - 24 × 24 grid; UP1C in x, UP1C in θ

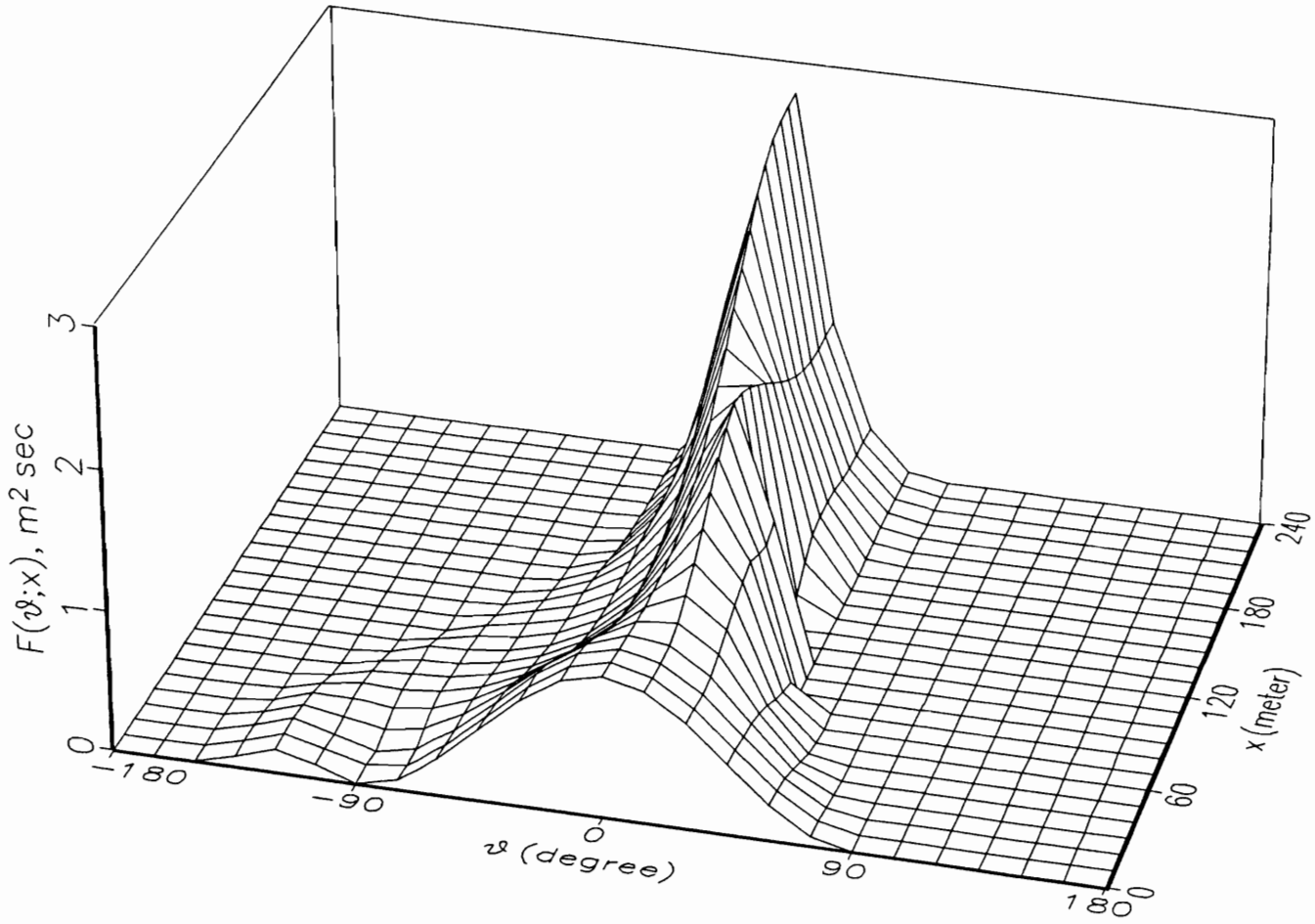

Figure 30. Case 3 - 24 × 24 grid; UP2C in x, UP2N in θ

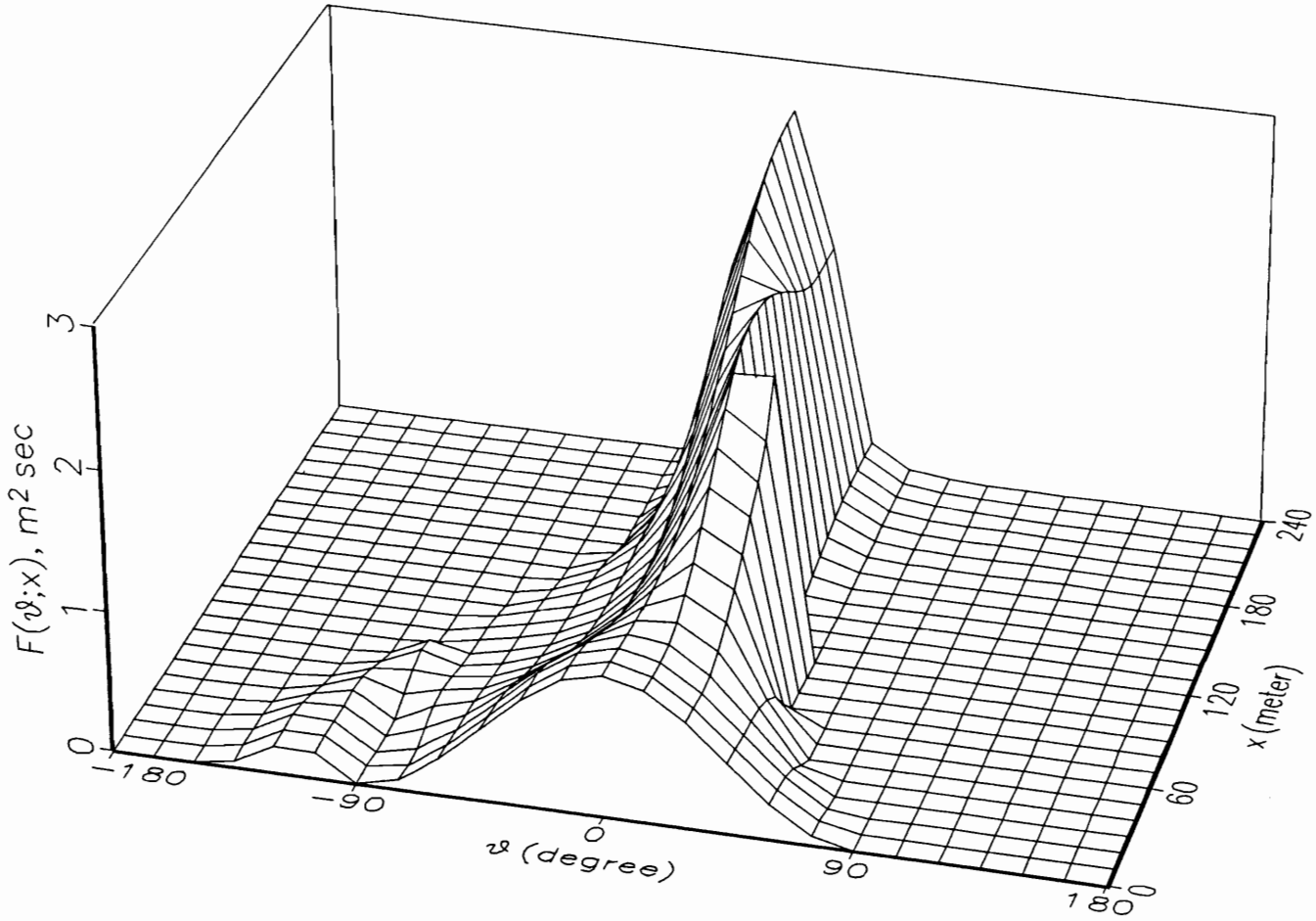

Figure 31. Case 3 - 24 × 24 grid; UP2C in x, LW in θ

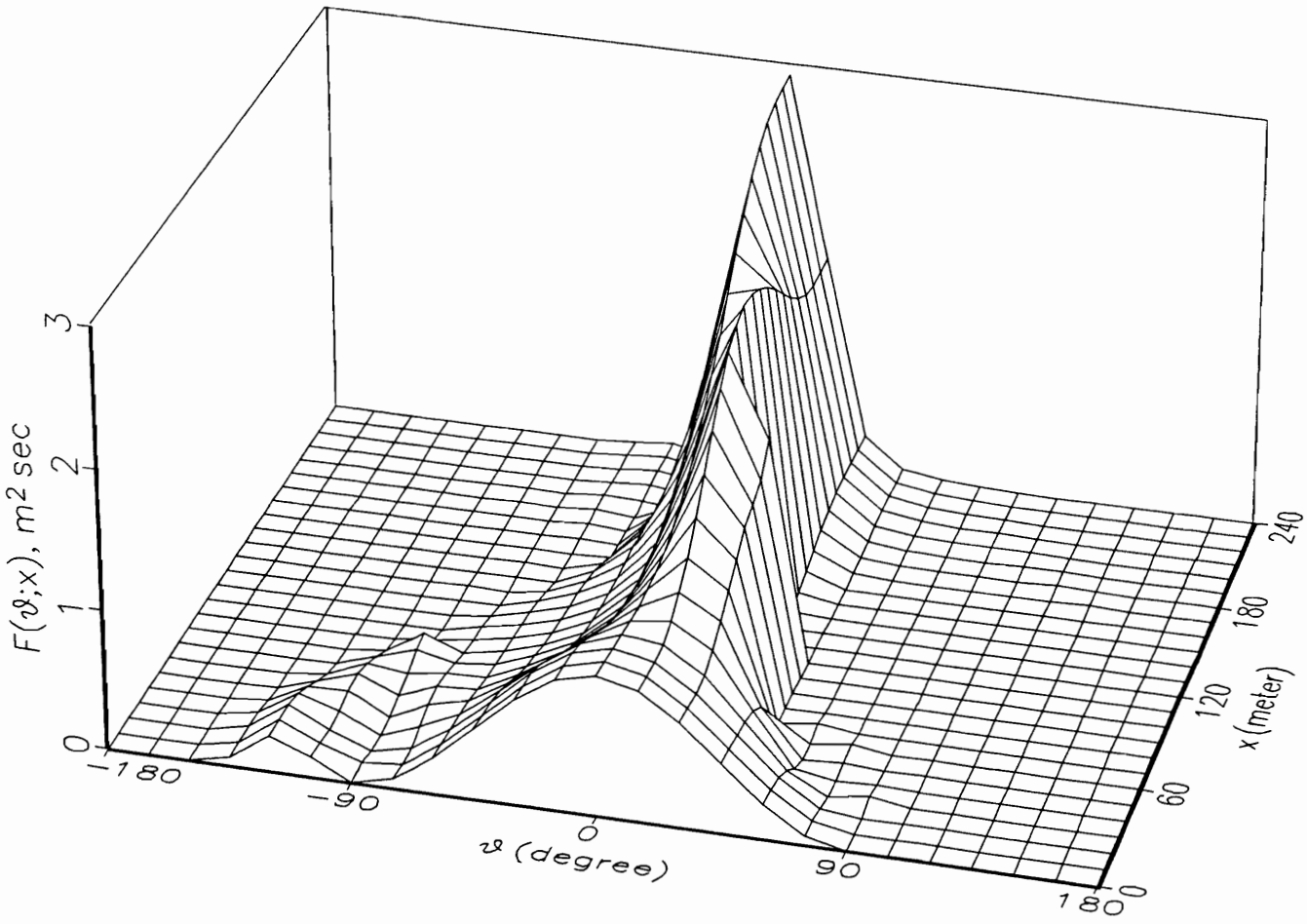

Figure 32. Case 3 - 24 × 24 grid; UP2C in x, LWG in θ

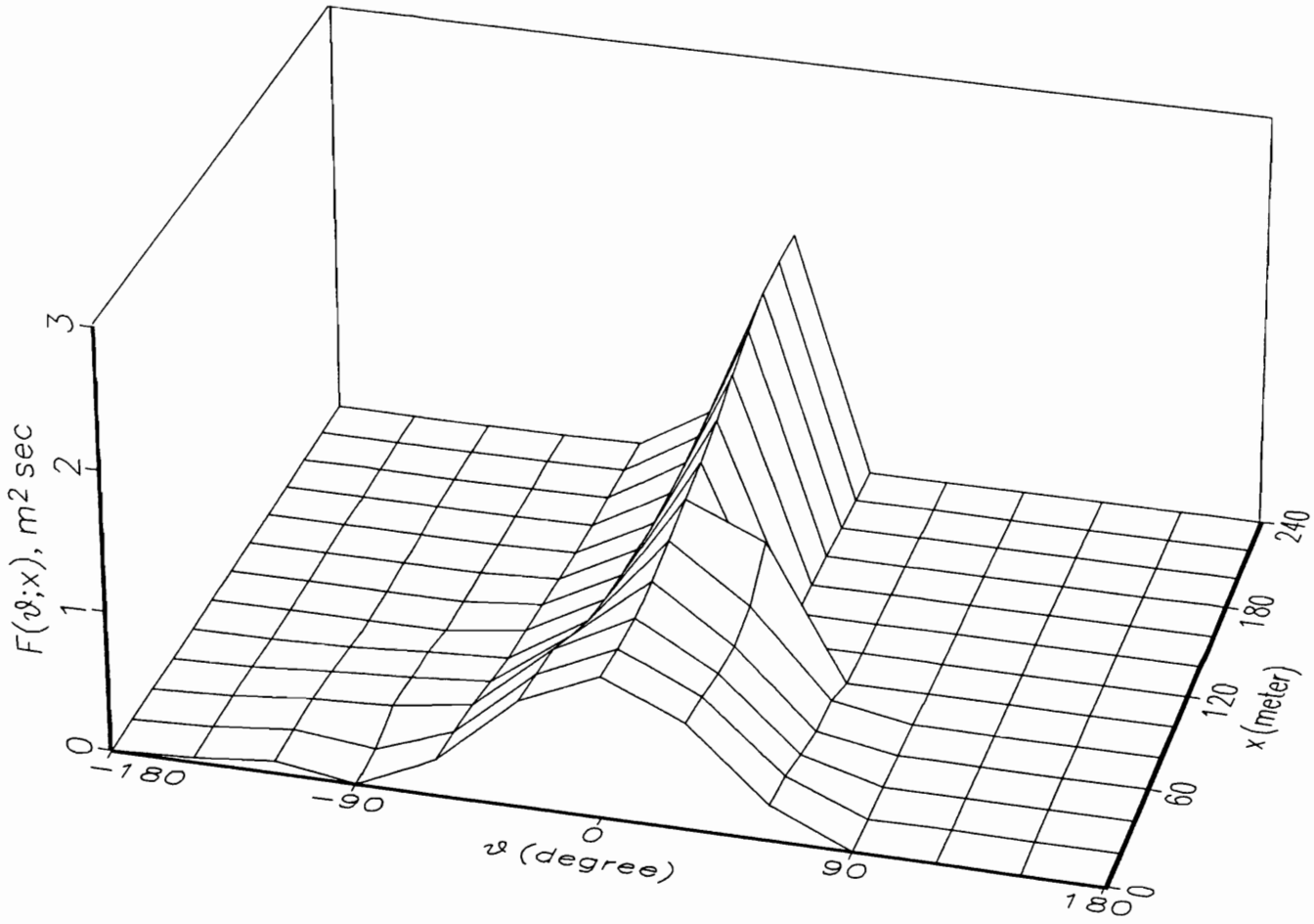

Figure 33. Case 3 - 12 × 12 grid; UP1C in x, UP1C in θ

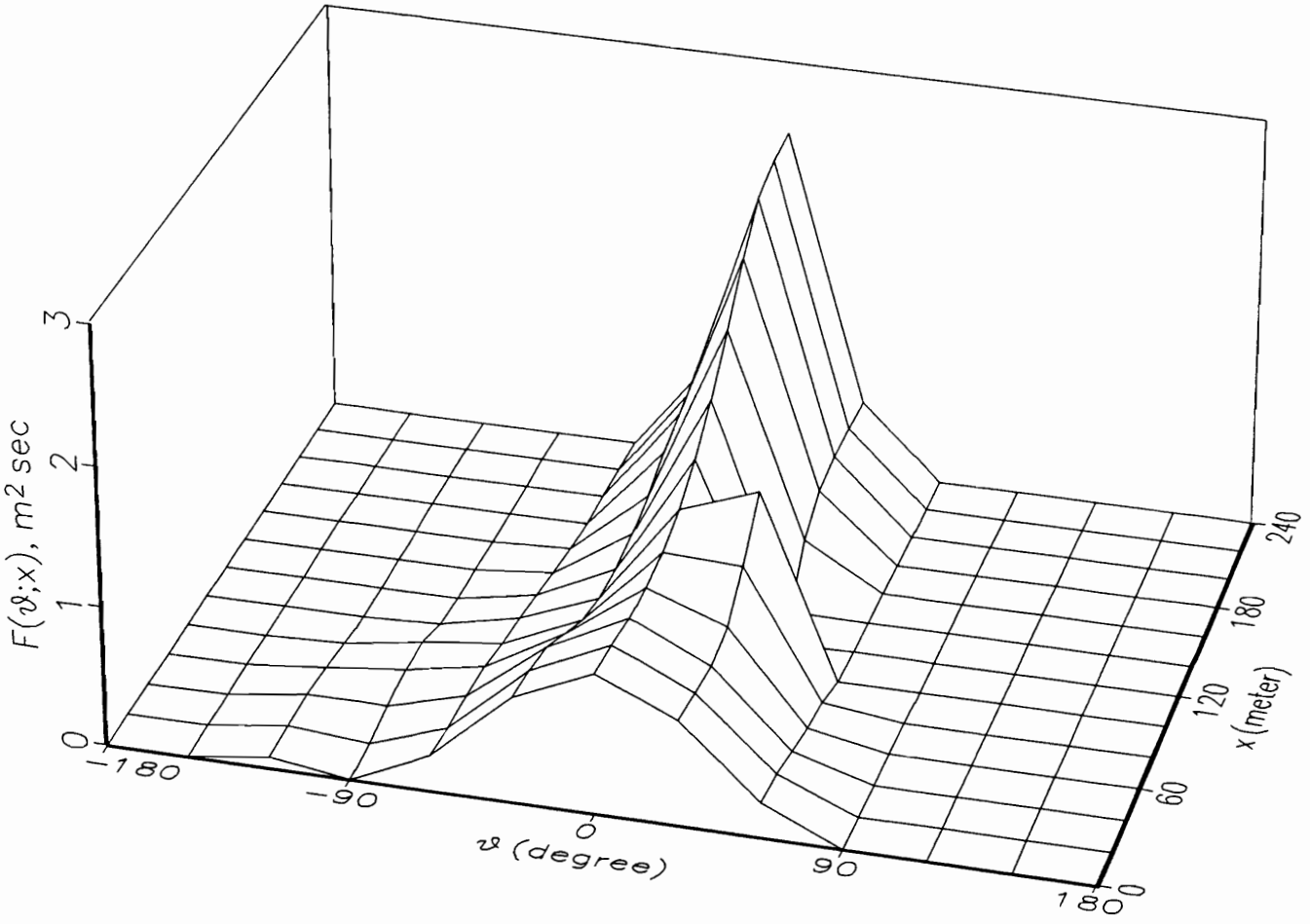

Figure 34. Case 3 - 12 × 12 grid; UP2C in x, UP2N in θ

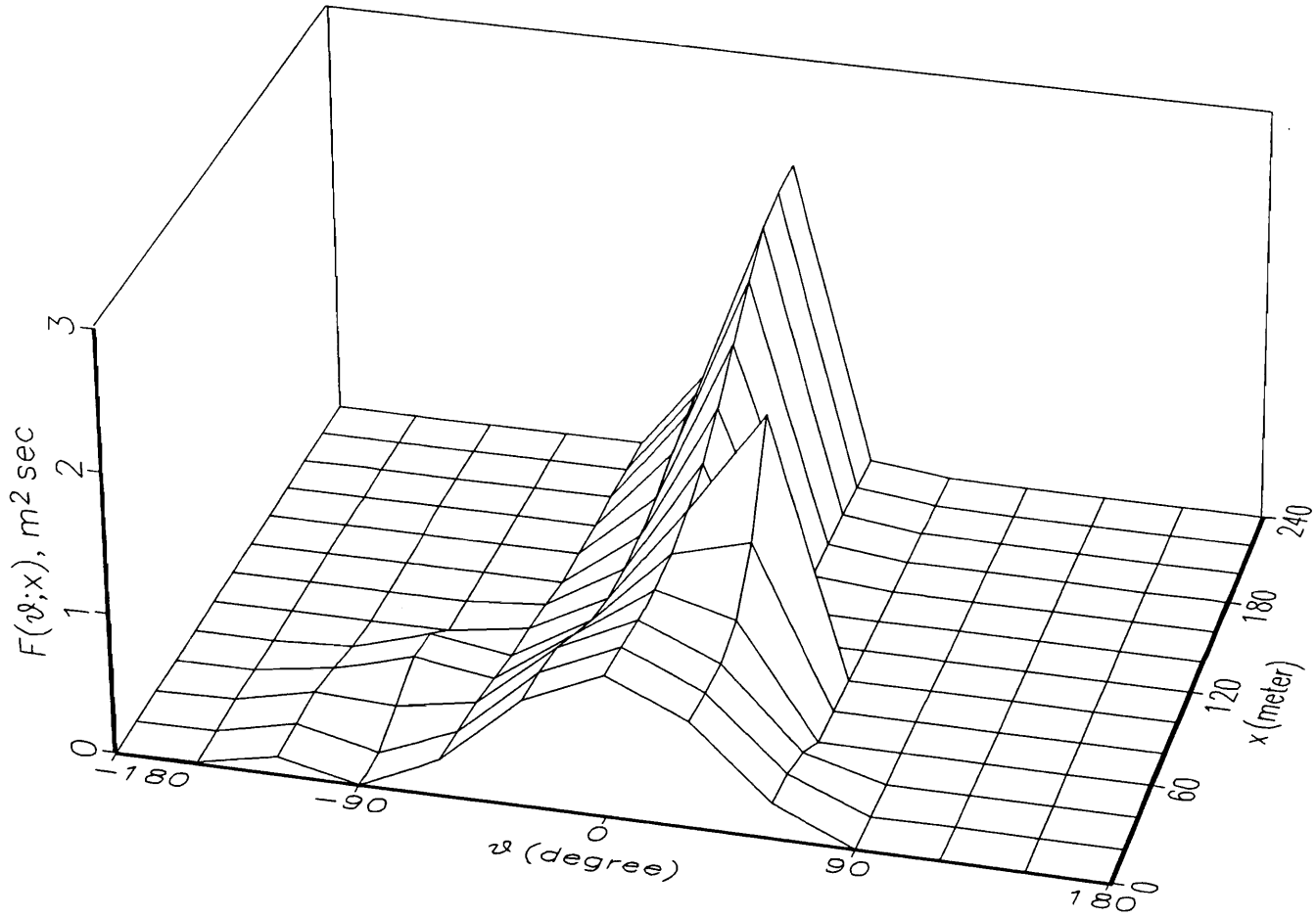

Figure 35. Case 3 - 12 × 12 grid; UP2C in x, LW in θ

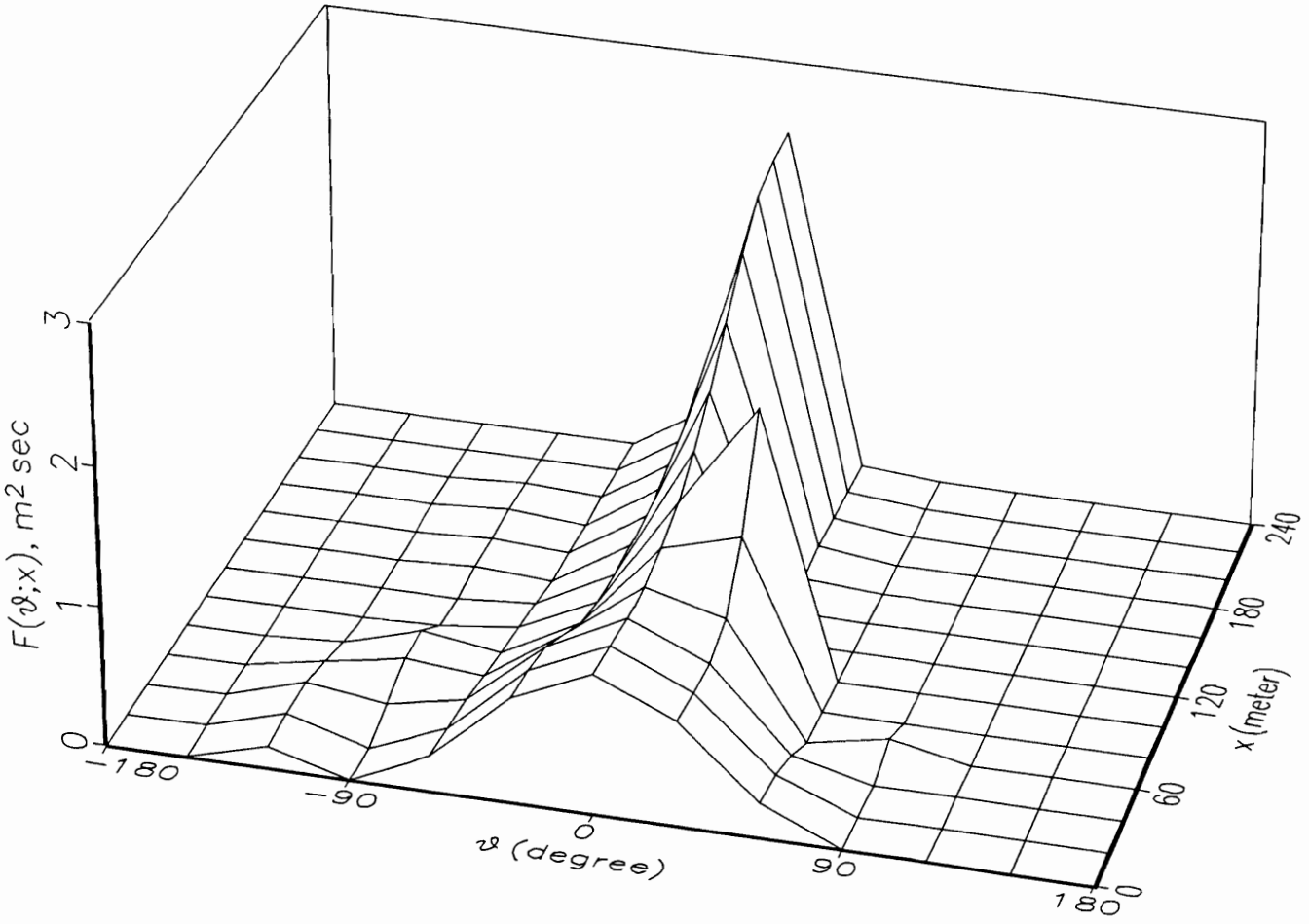

Figure 36. Case 3 - 12 × 12 grid; UP2C in x, LWG in θ

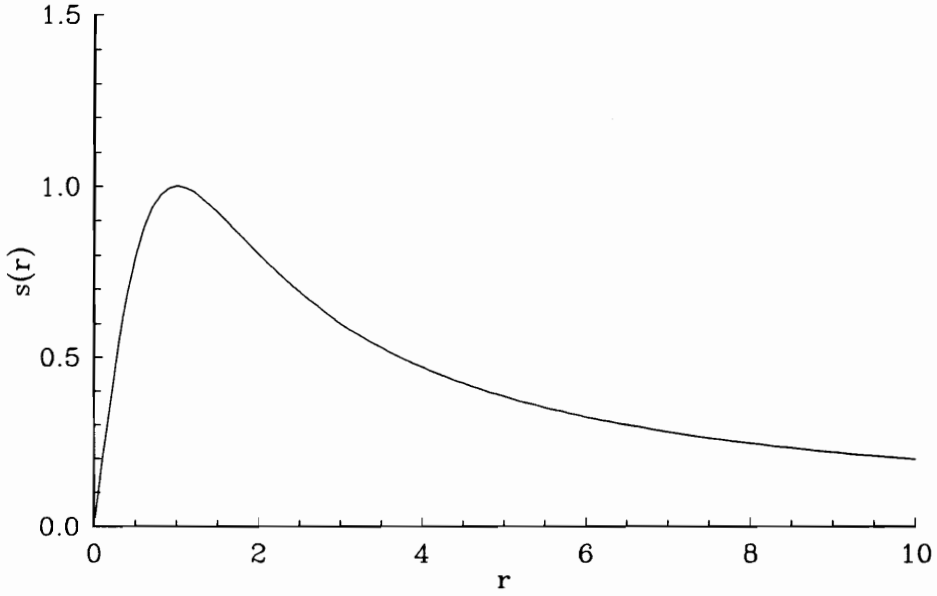

Figure 37. Continuous limiter

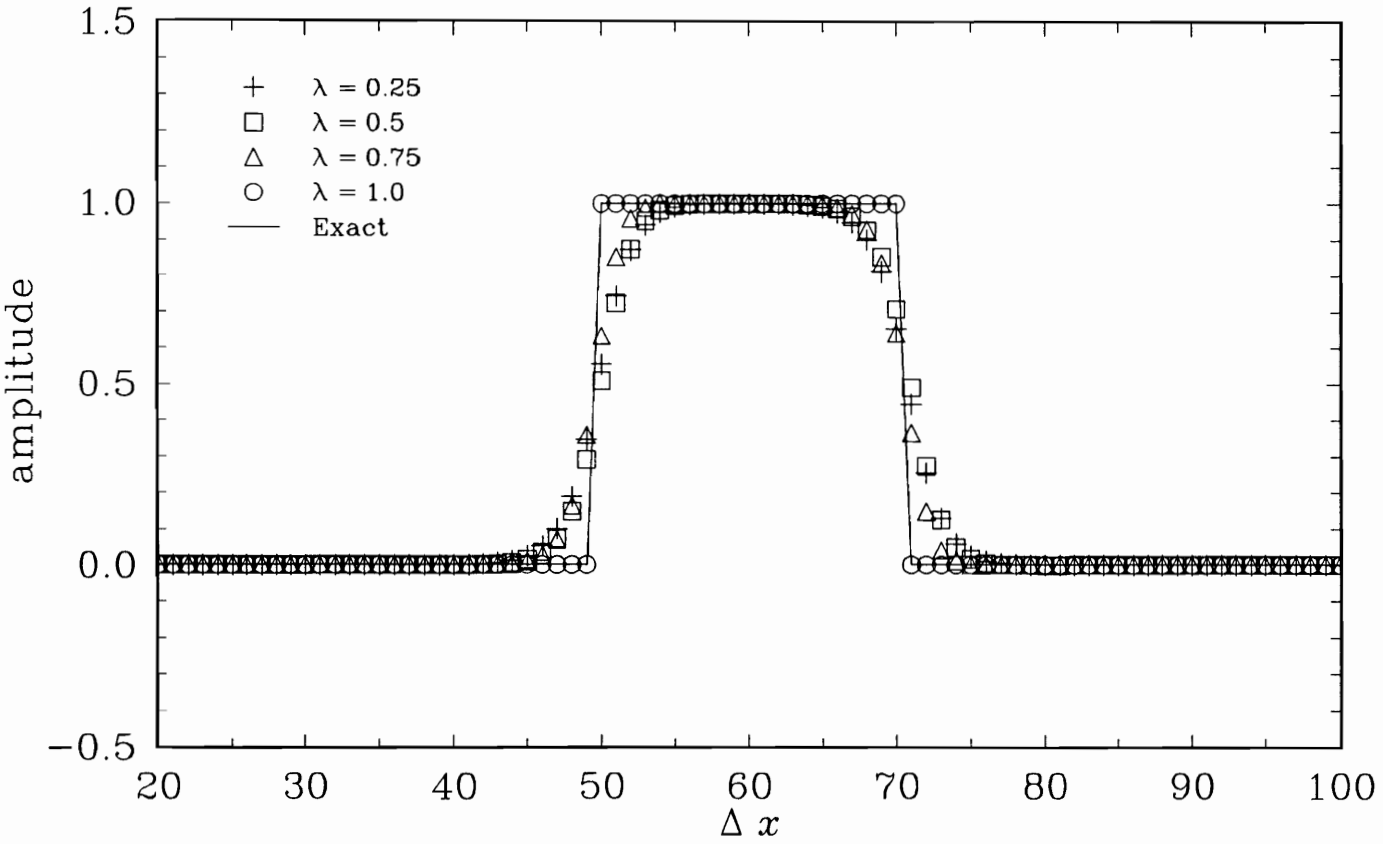

Figure 38. Square wave test for new scheme

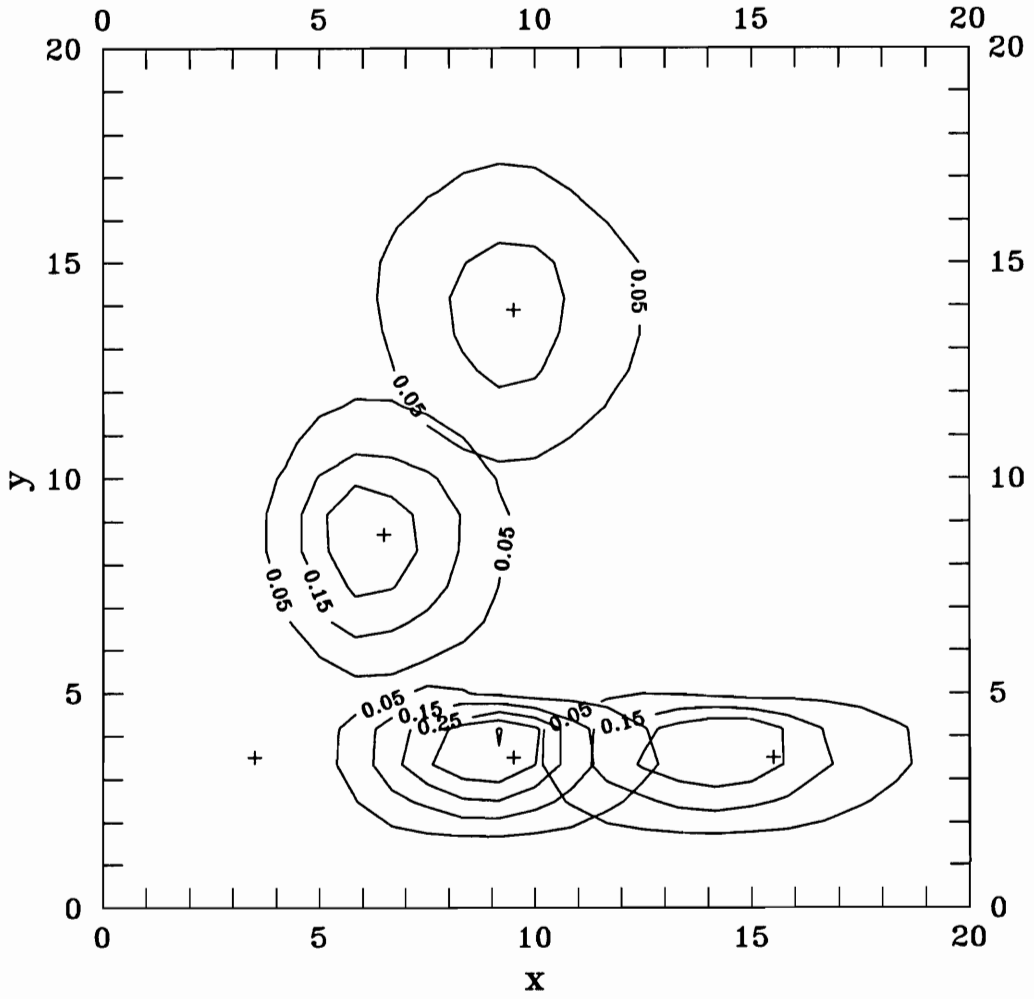

Figure 39. Unit pulse test for new scheme $(0°, 60°)$

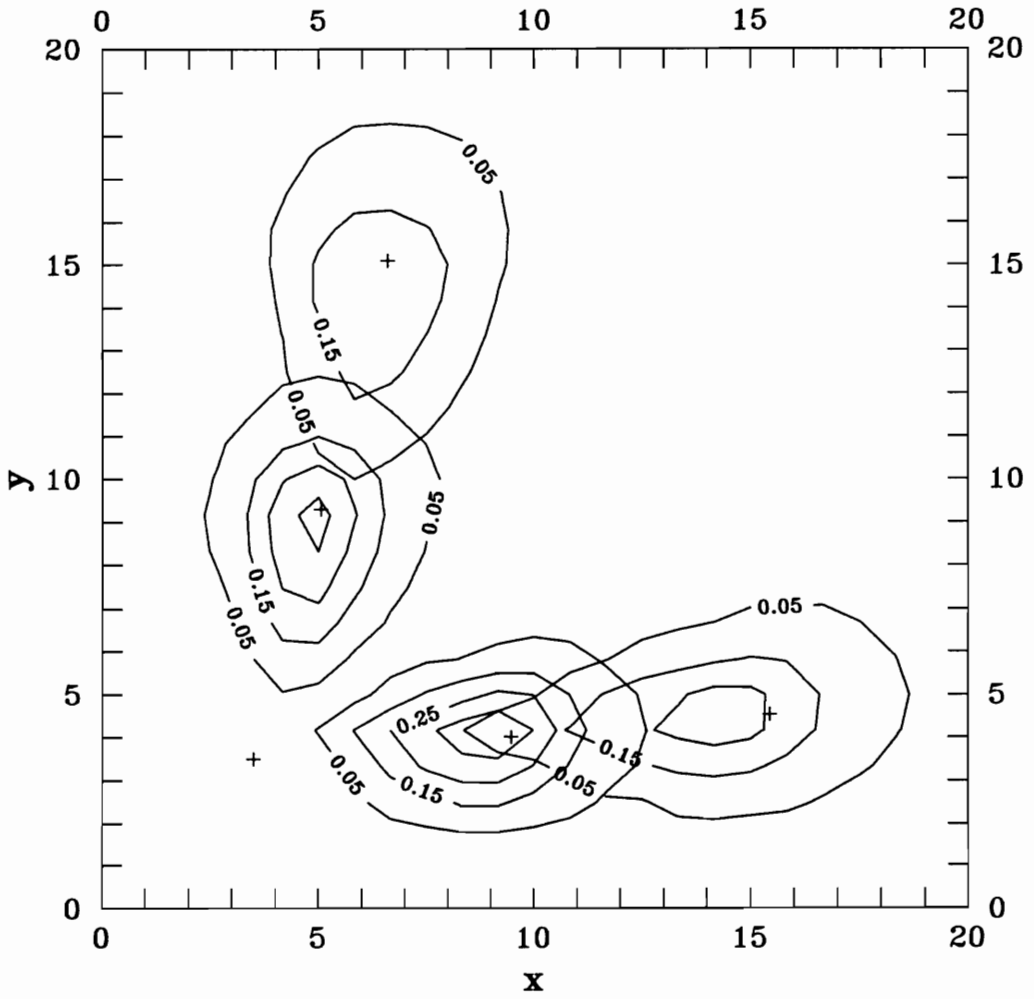

Figure 40. Unit pulse test for new scheme $(5°, 75°)$

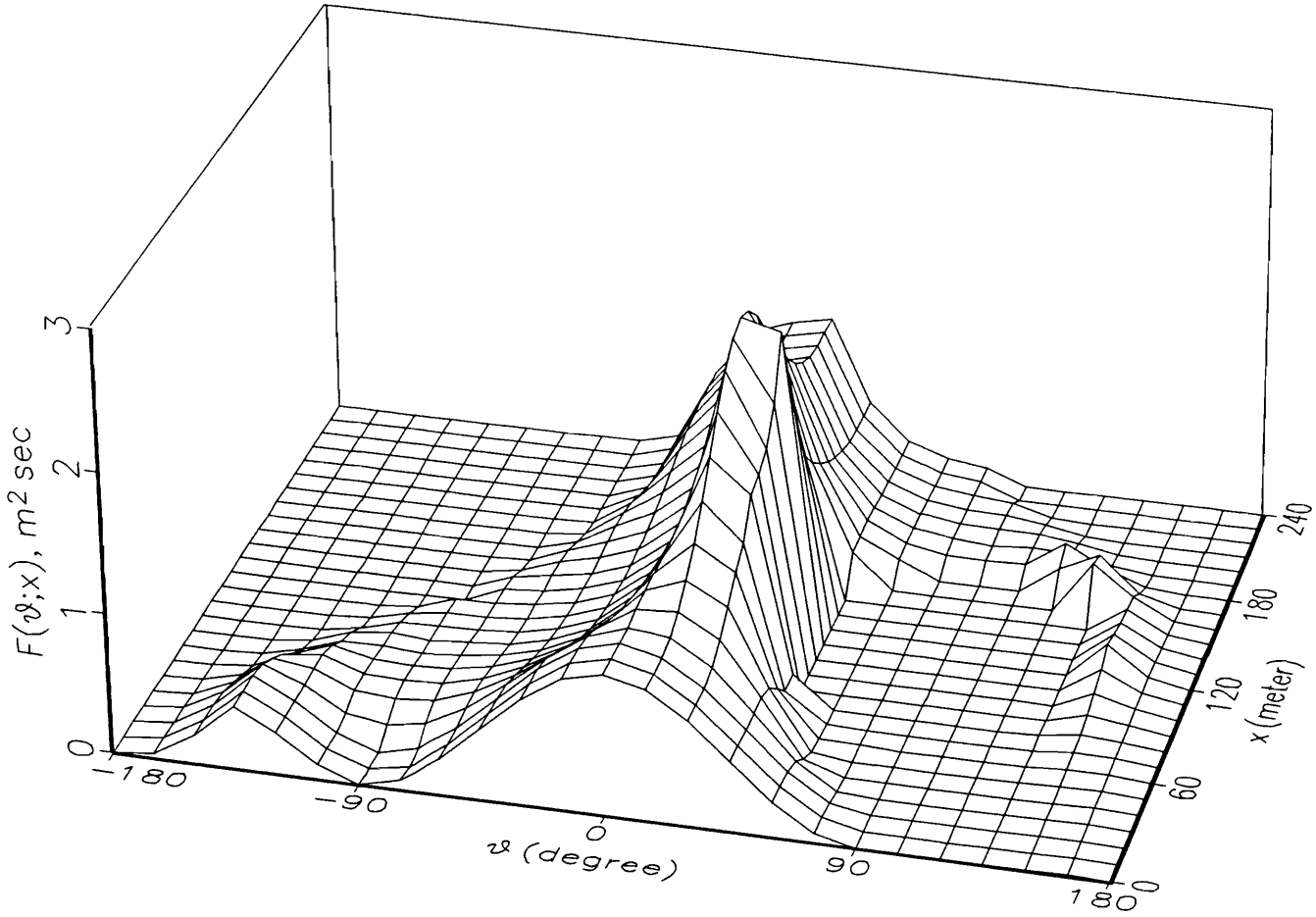

Figure 41. Case 1 - 24 × 24 grid; new scheme

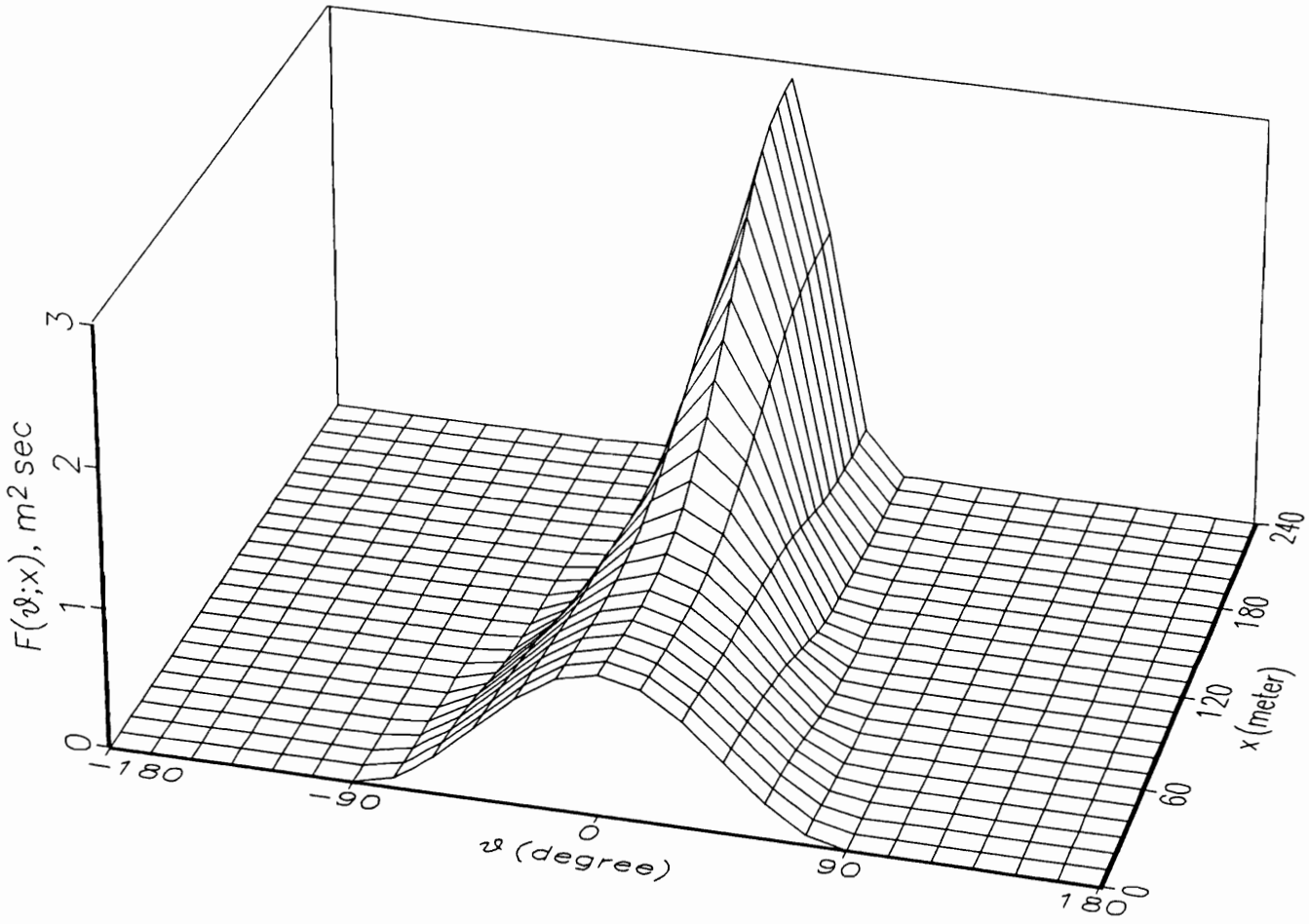

Figure 42. Case 2 - 24 × 24 grid; new scheme

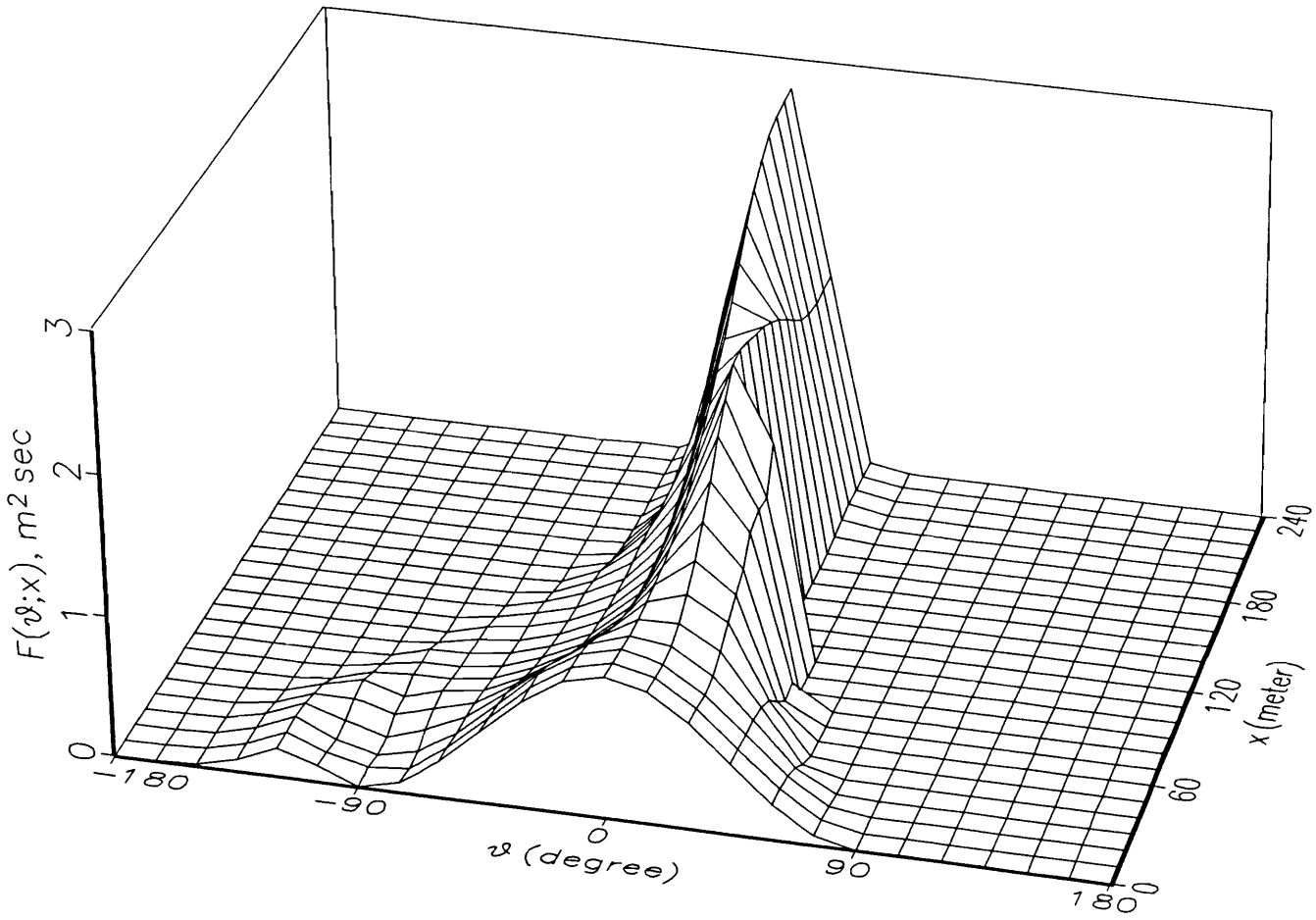

Figure 43. Case 3 - 24 × 24 grid; new scheme

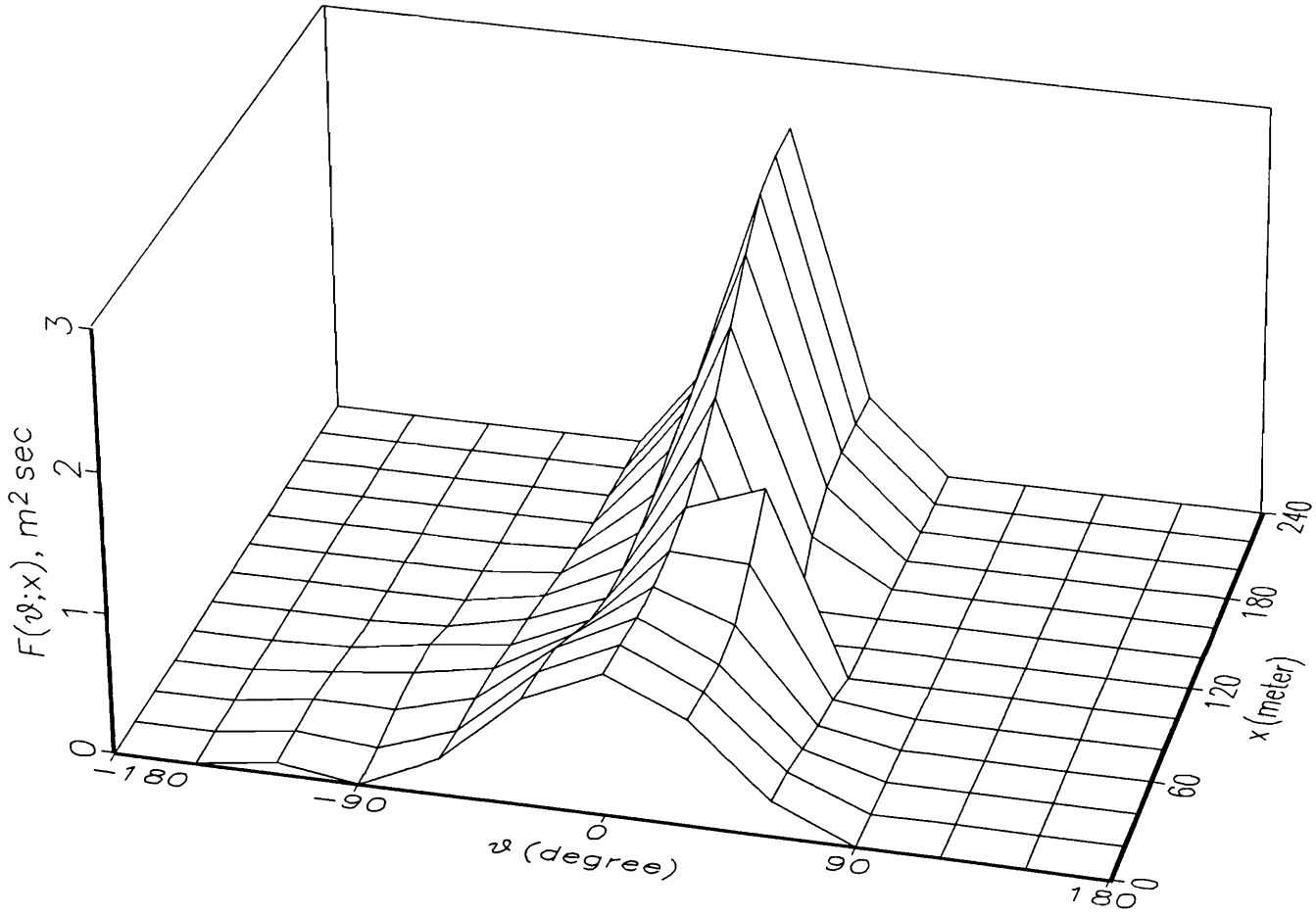

Figure 44. Case 3 - 12 × 12 grid; new scheme

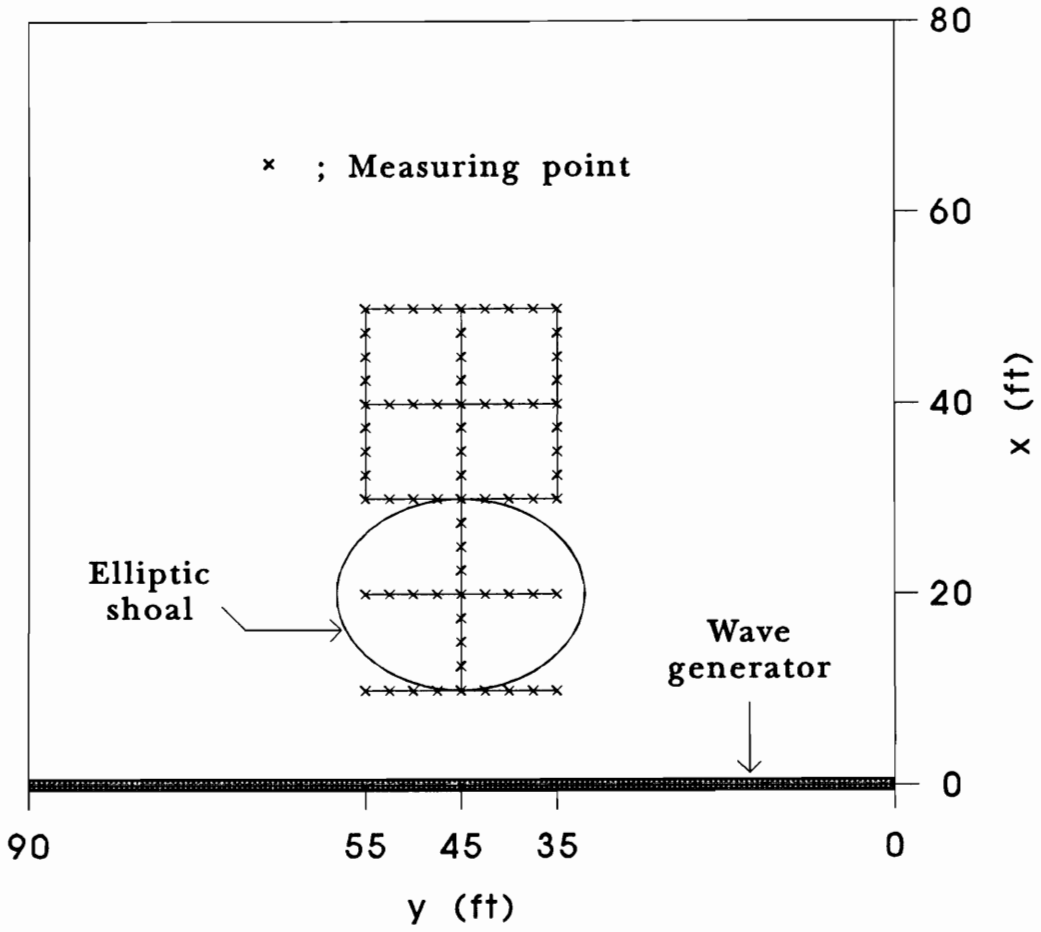

Figure 45. Layout of elliptic shoal test set-up

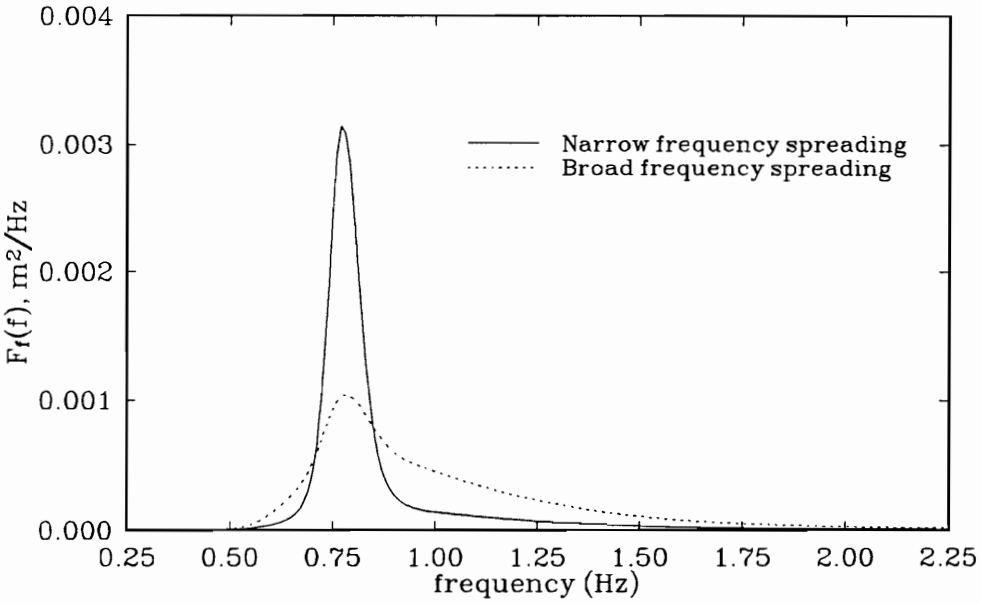

Figure 46. Frequency spreading function for elliptic shoal test

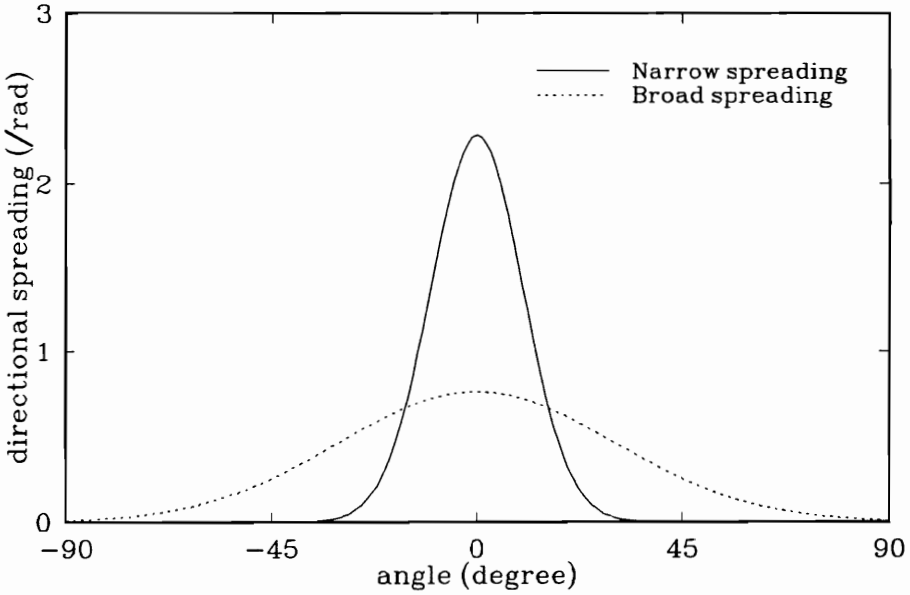

Figure 47. Directional spreading function for elliptic shoal test

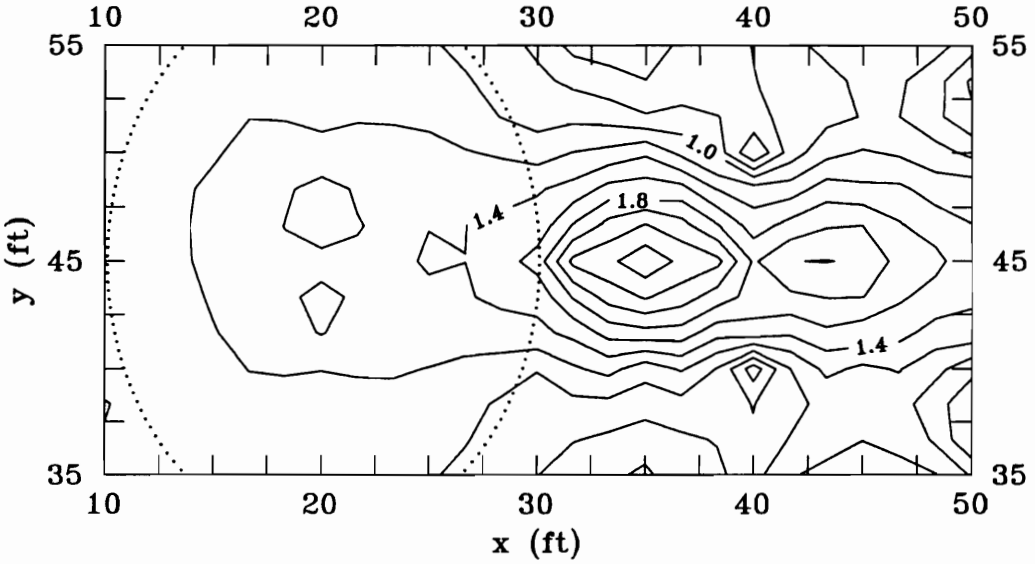

Figure 48. Model test results for monochromatic wave

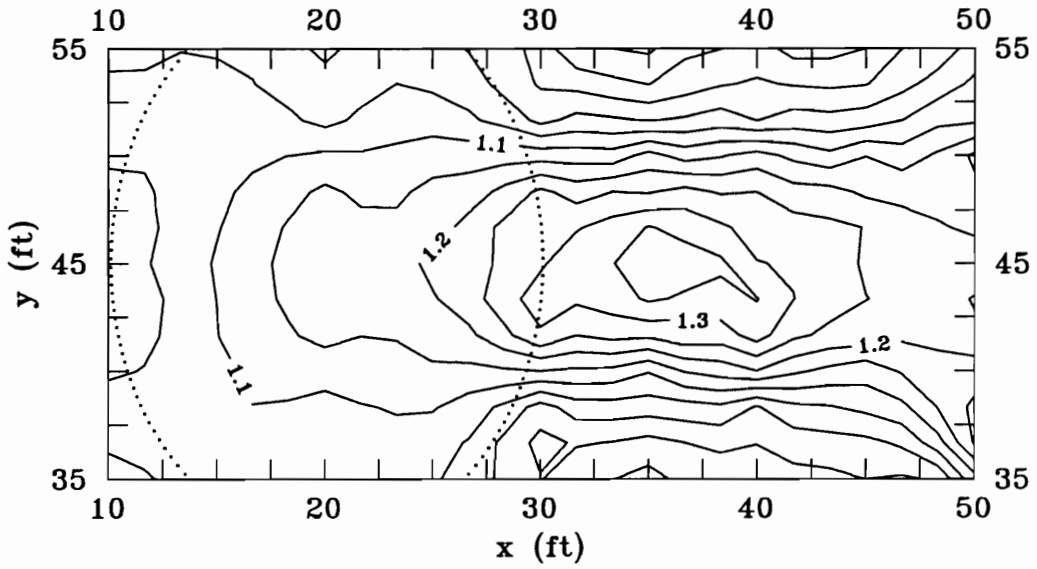

Figure 49. Model test results for narrow directional spreading wave

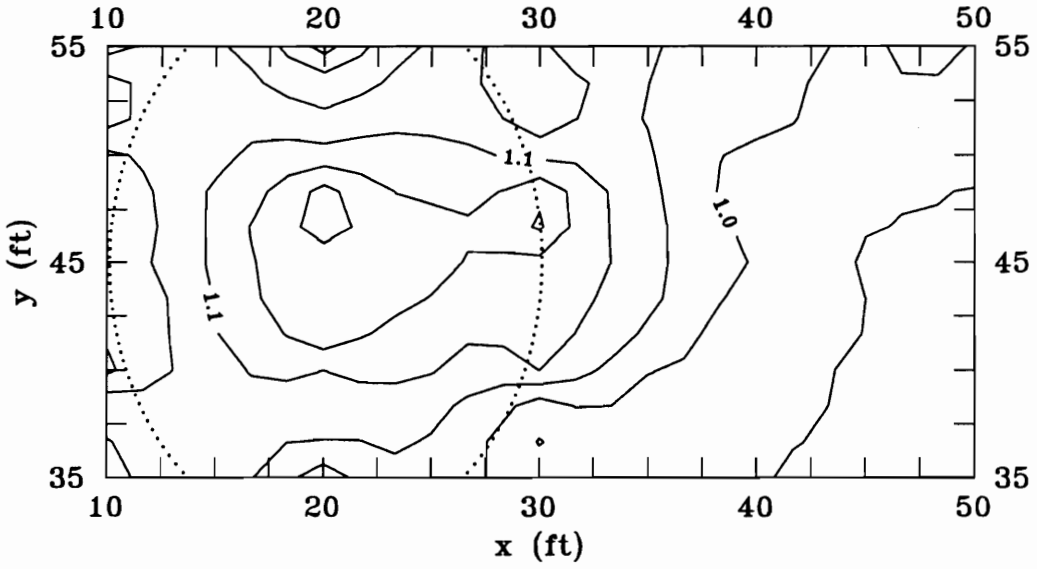

Figure 50. Model test results for broad directional spreading wave

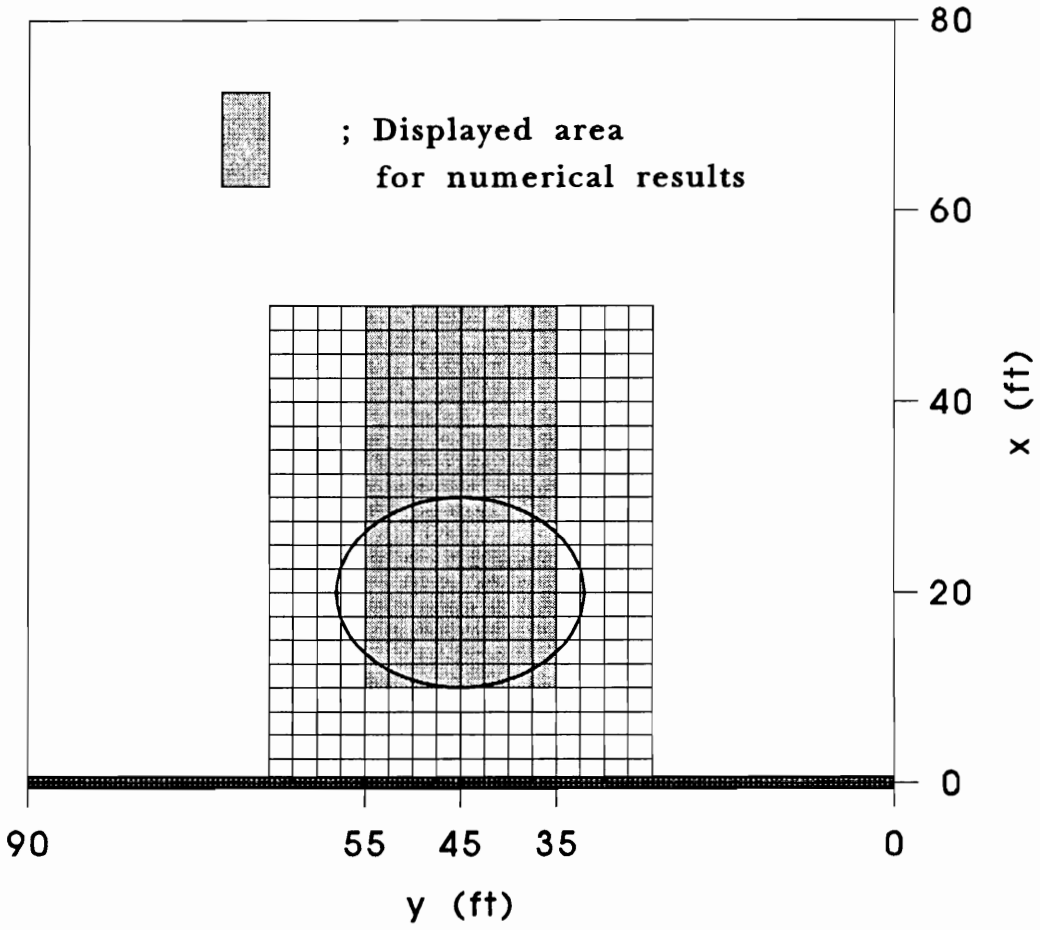

Figure 51. Grid for numerical calculation

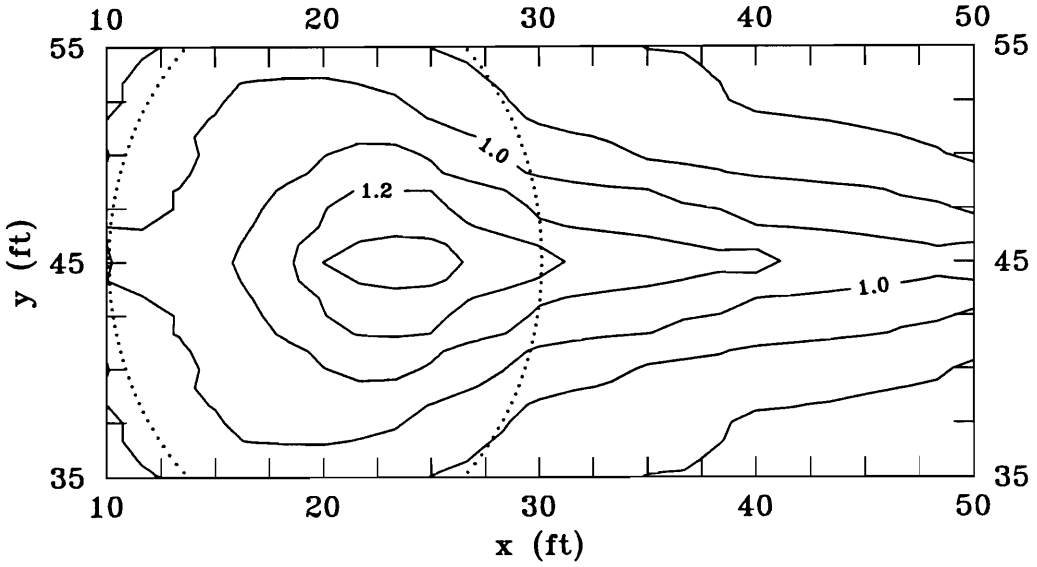

(a) 1st order upwind scheme

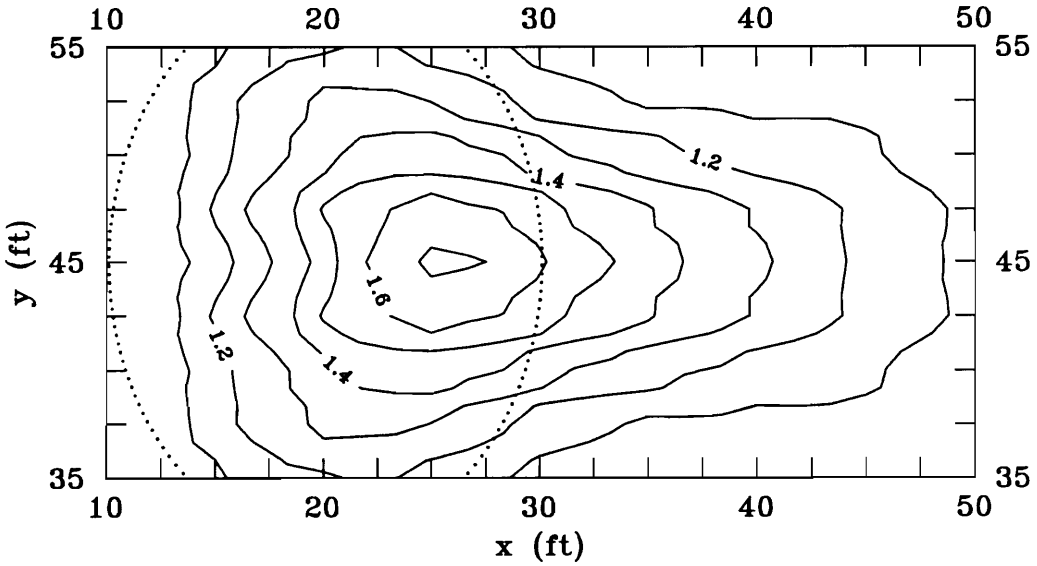

(b) new scheme

Figure 52. Monochromatic wave, 30° resolution

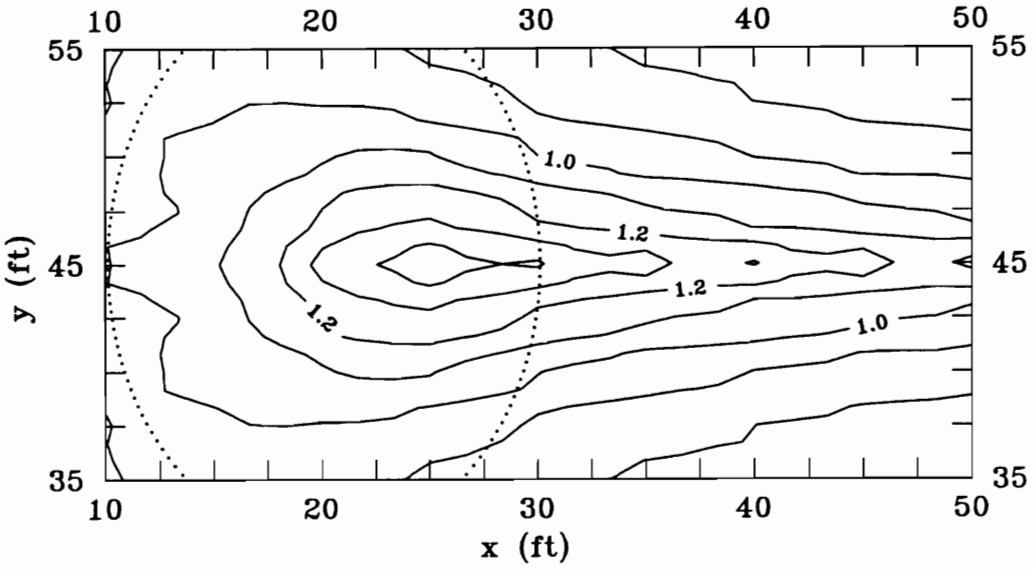

(a) 1st order upwind scheme

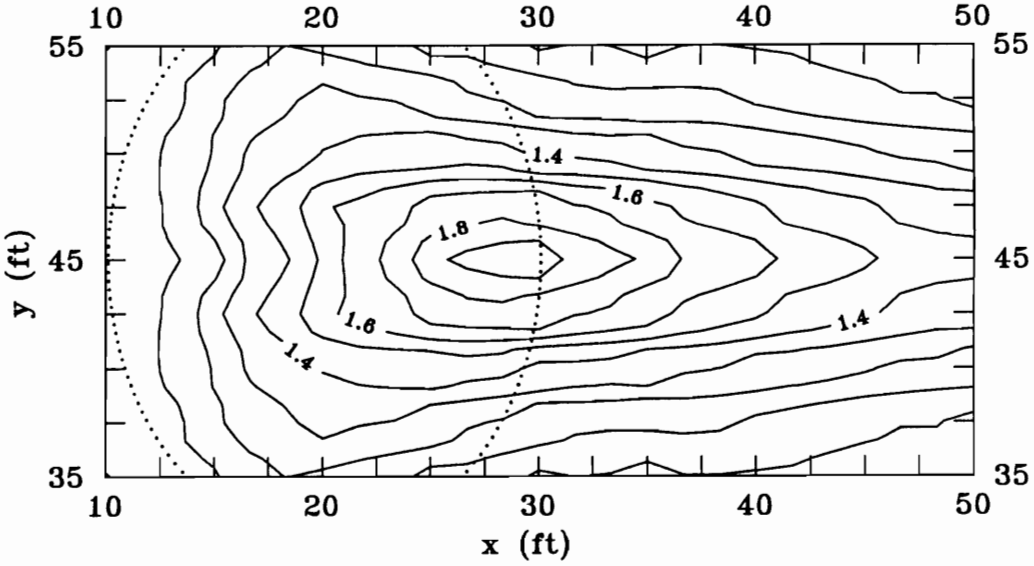

(b) new scheme

Figure 53. Monochromatic wave, 15° resolution

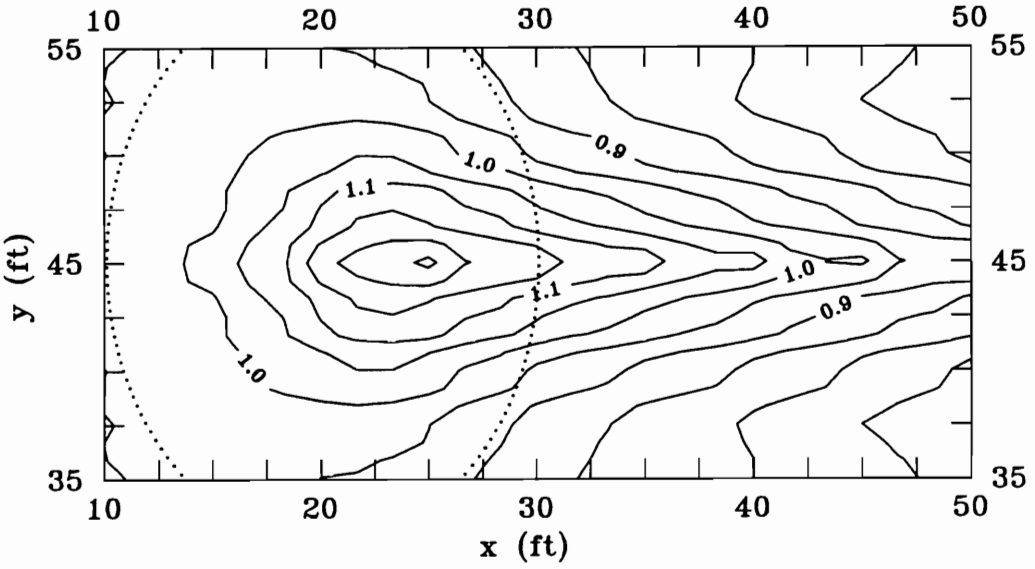

(a) 1st order upwind scheme

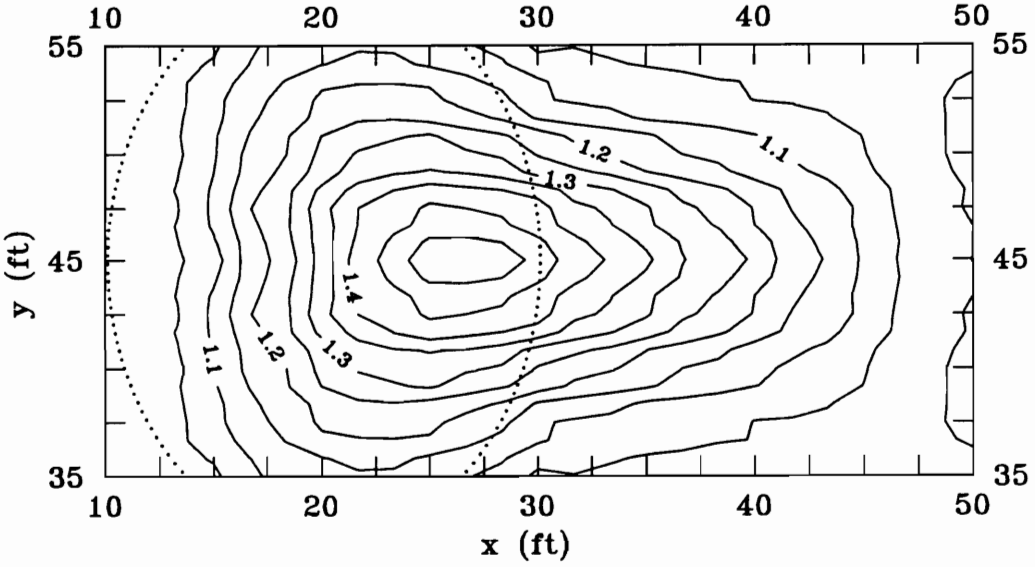

(b) new scheme

Figure 54. Narrow directional spreading wave, 30° resolution

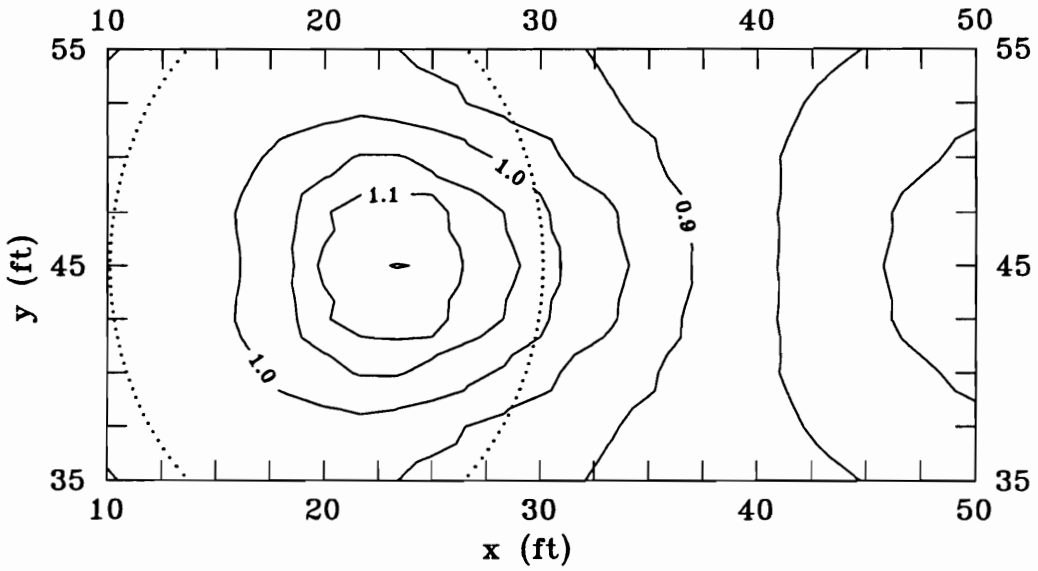

(a) 1st order upwind scheme

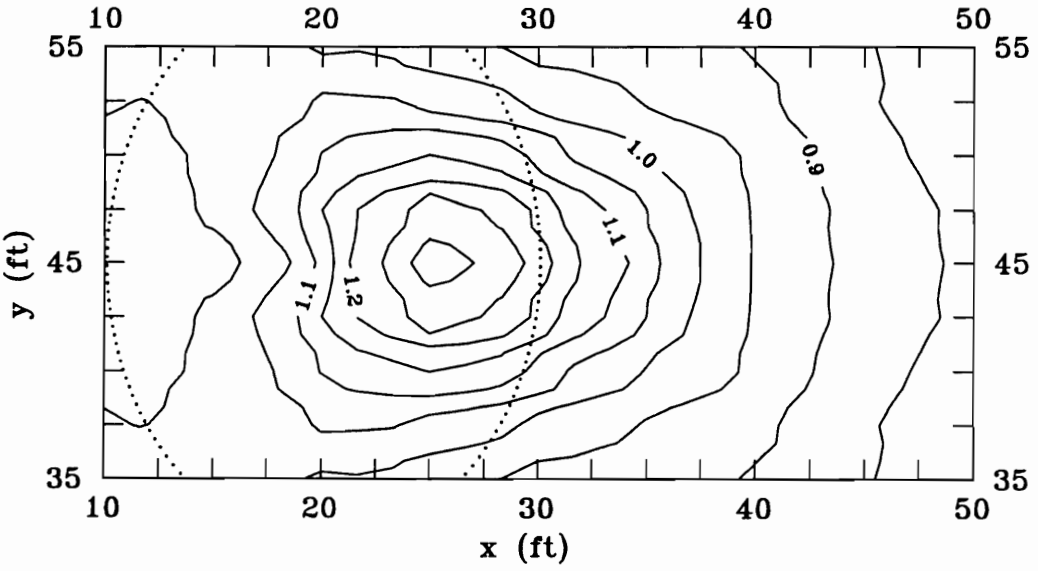

(b) new scheme

Figure 55. Narrow directional spreading wave, 30° resolution (misaligned grid)

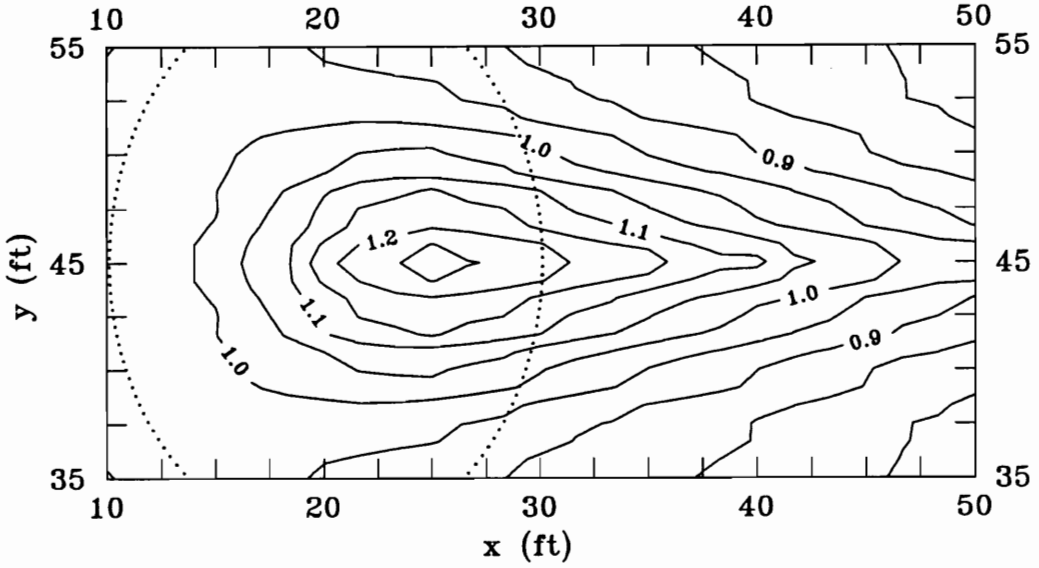

(a) 1st order upwind scheme

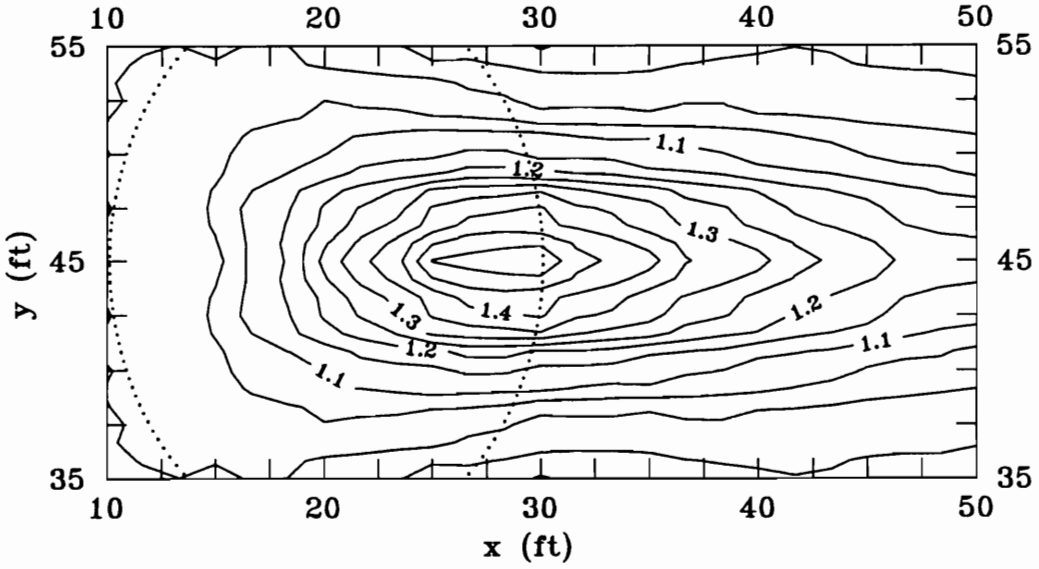

(b) new scheme

Figure 56. Narrow directional spreading wave, 15° resolution

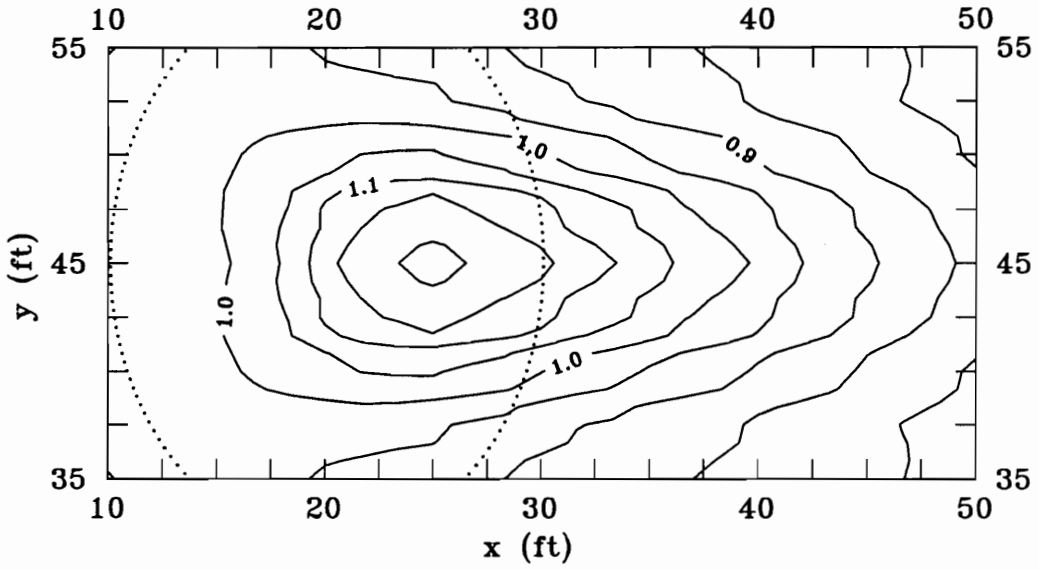

(a) 1st order upwind scheme

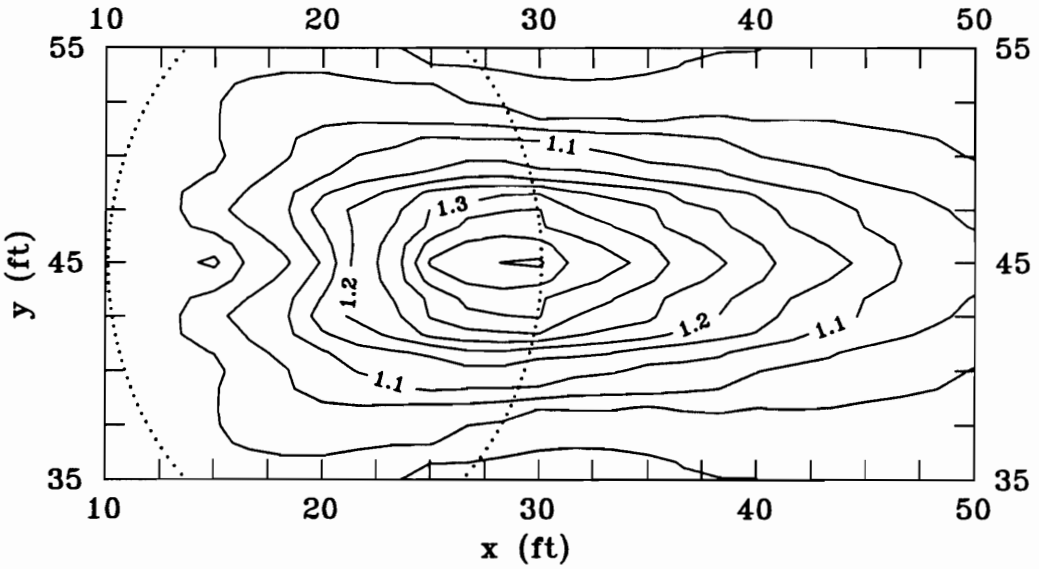

(b) new scheme

Figure 57. Narrow directional spreading wave, 15° resolution (misaligned grid)

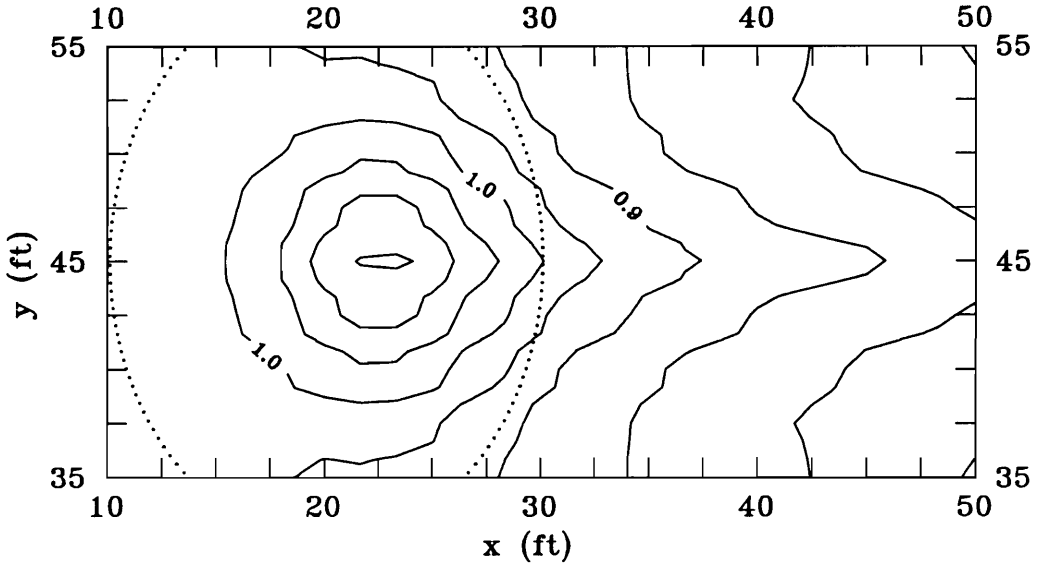

(a) 1st order upwind scheme

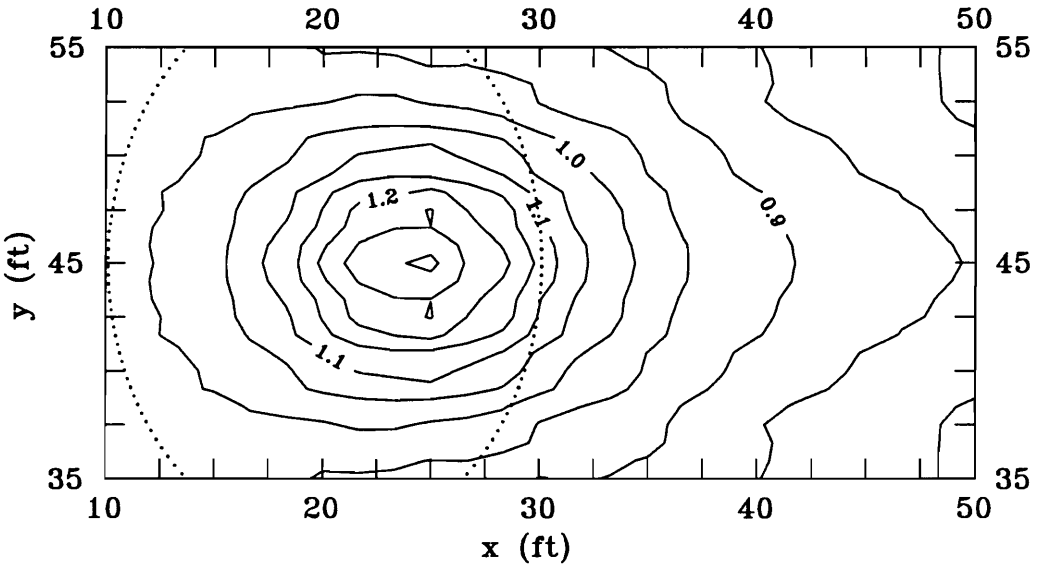

(b) new scheme

Figure 58. Broad directional spreading wave, 30° resolution

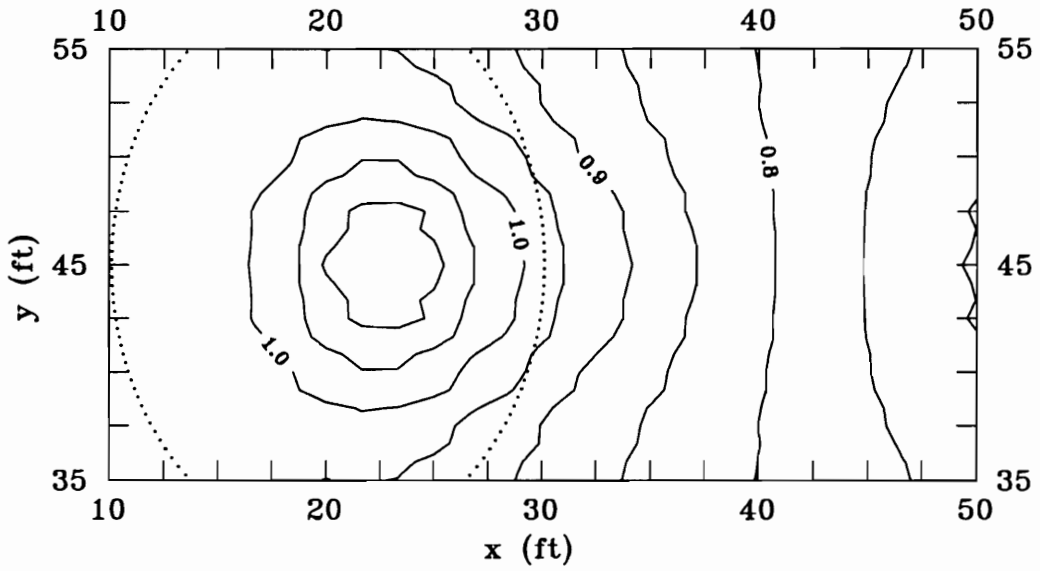

(a) 1st order upwind scheme

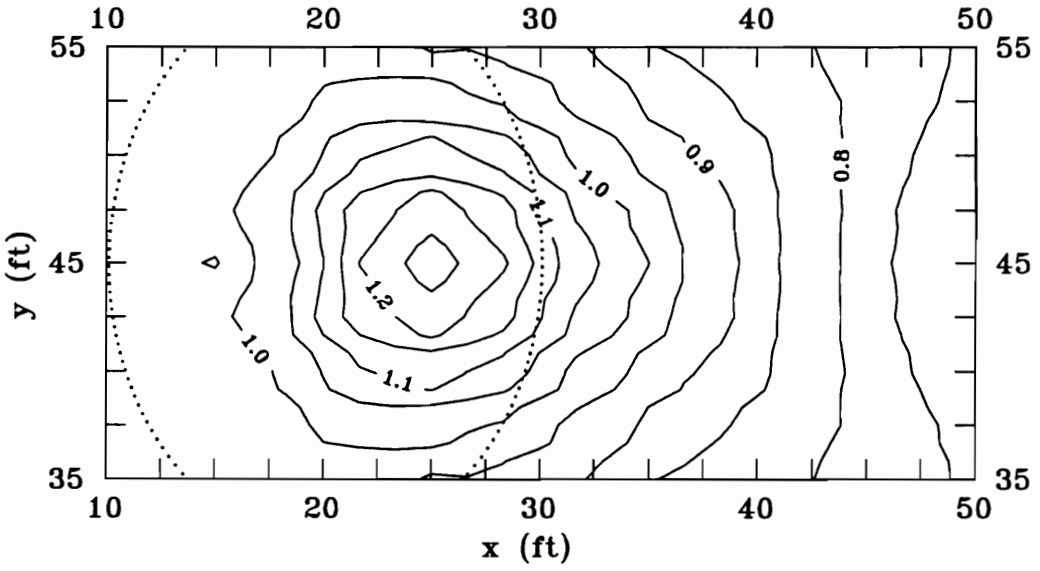

(b) new scheme

Figure 59. Broad directional spreading wave, 30° resolution (misaligned grid)

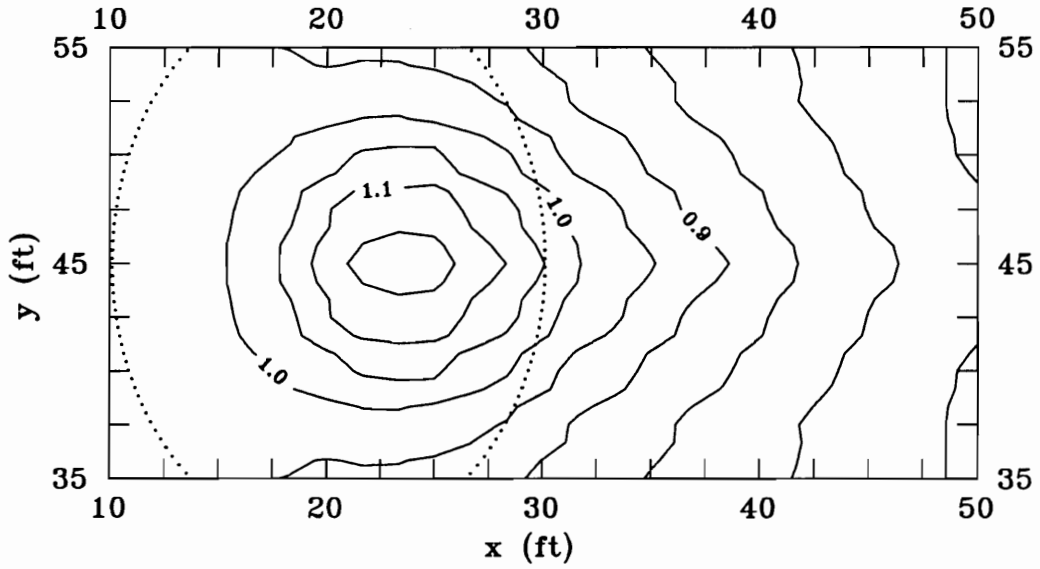

(a) 1st order upwind scheme

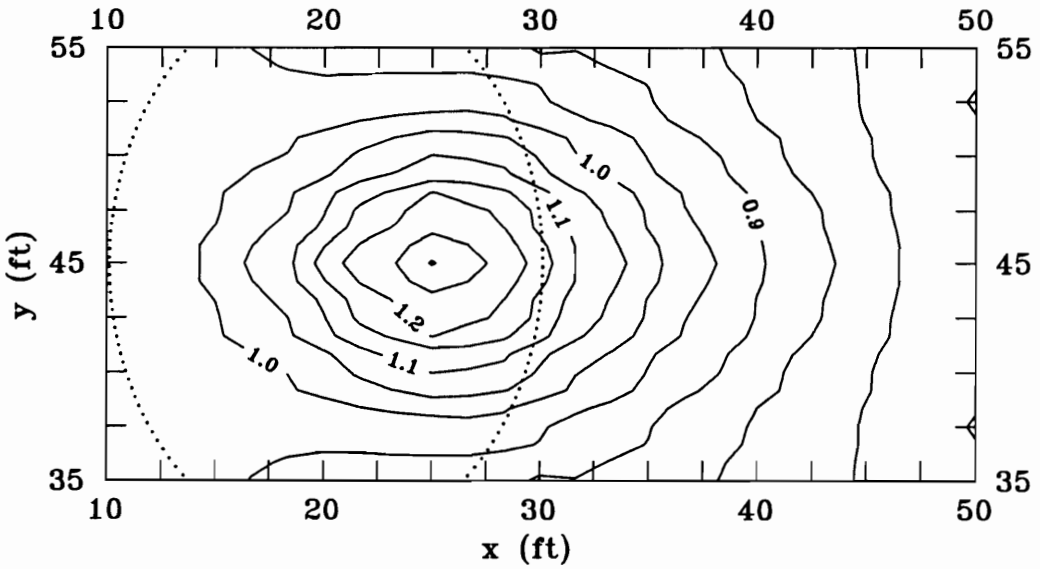

(b) new scheme

Figure 60. Broad directional spreading wave, 15° resolution

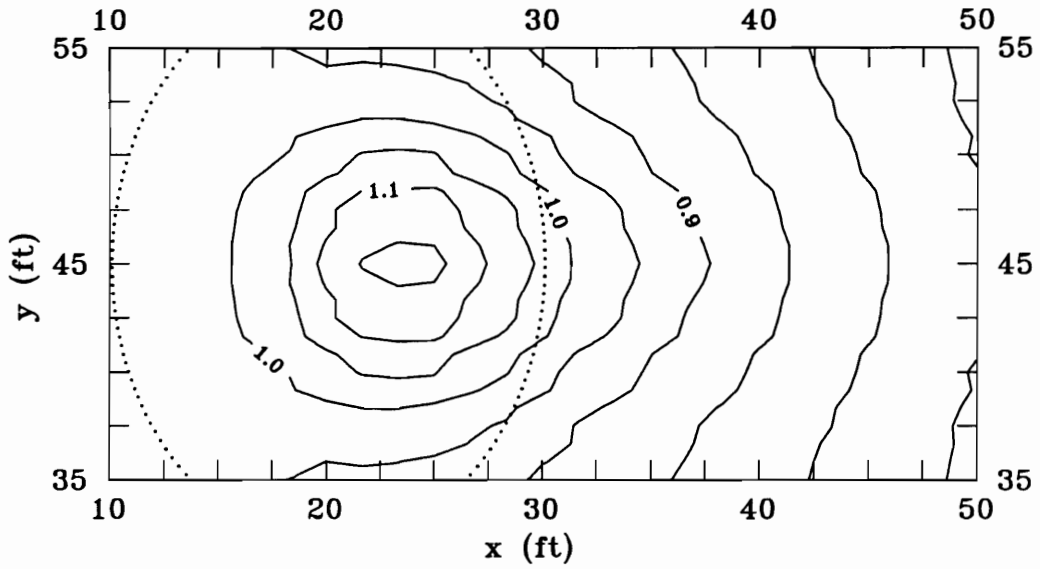

(a) 1st order upwind scheme

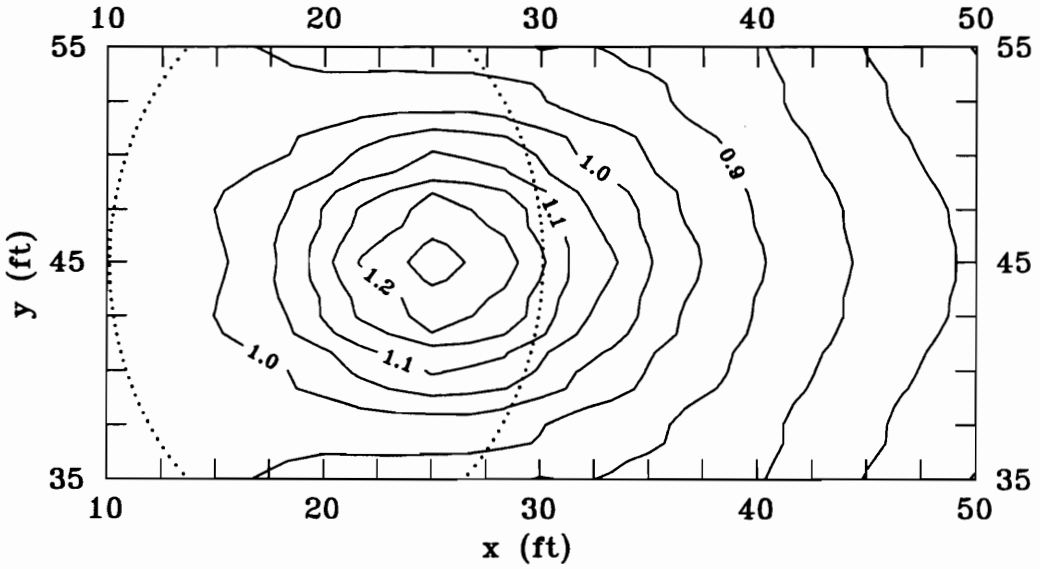

(b) new scheme

Figure 61. Broad directional spreading wave, 15° resolution (misaligned grid)

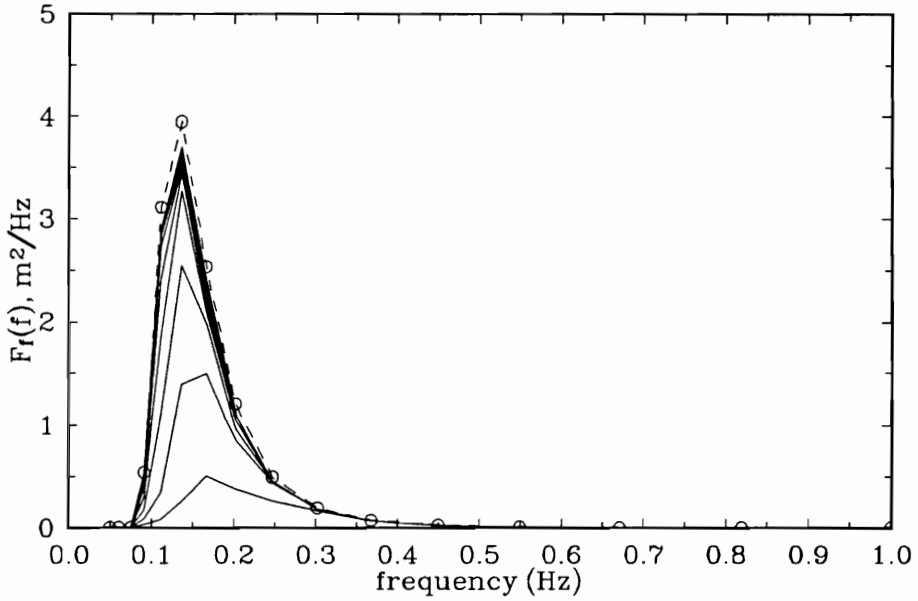

(a) point spectral growth

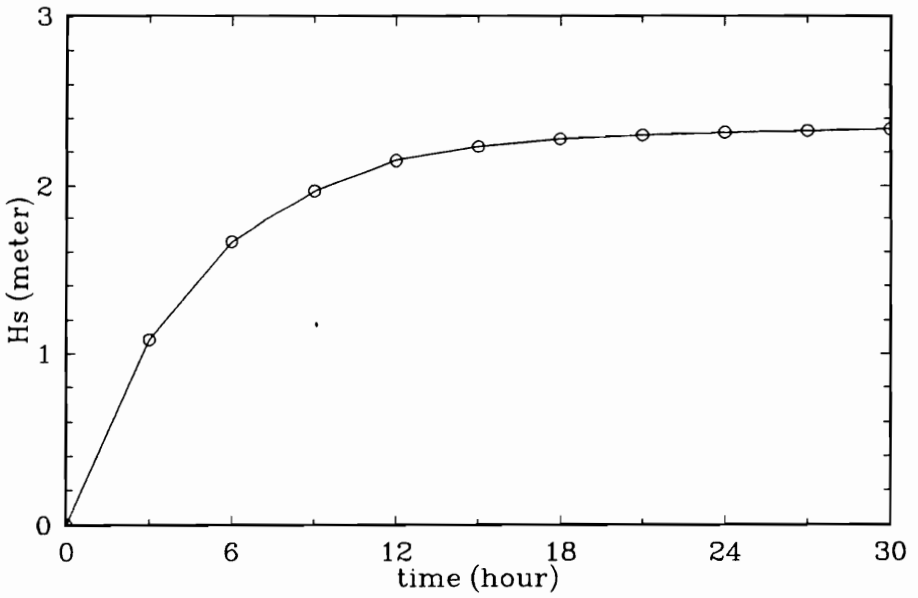

(b) significant wave height

Figure 62. Point spectral growth using VPINK model

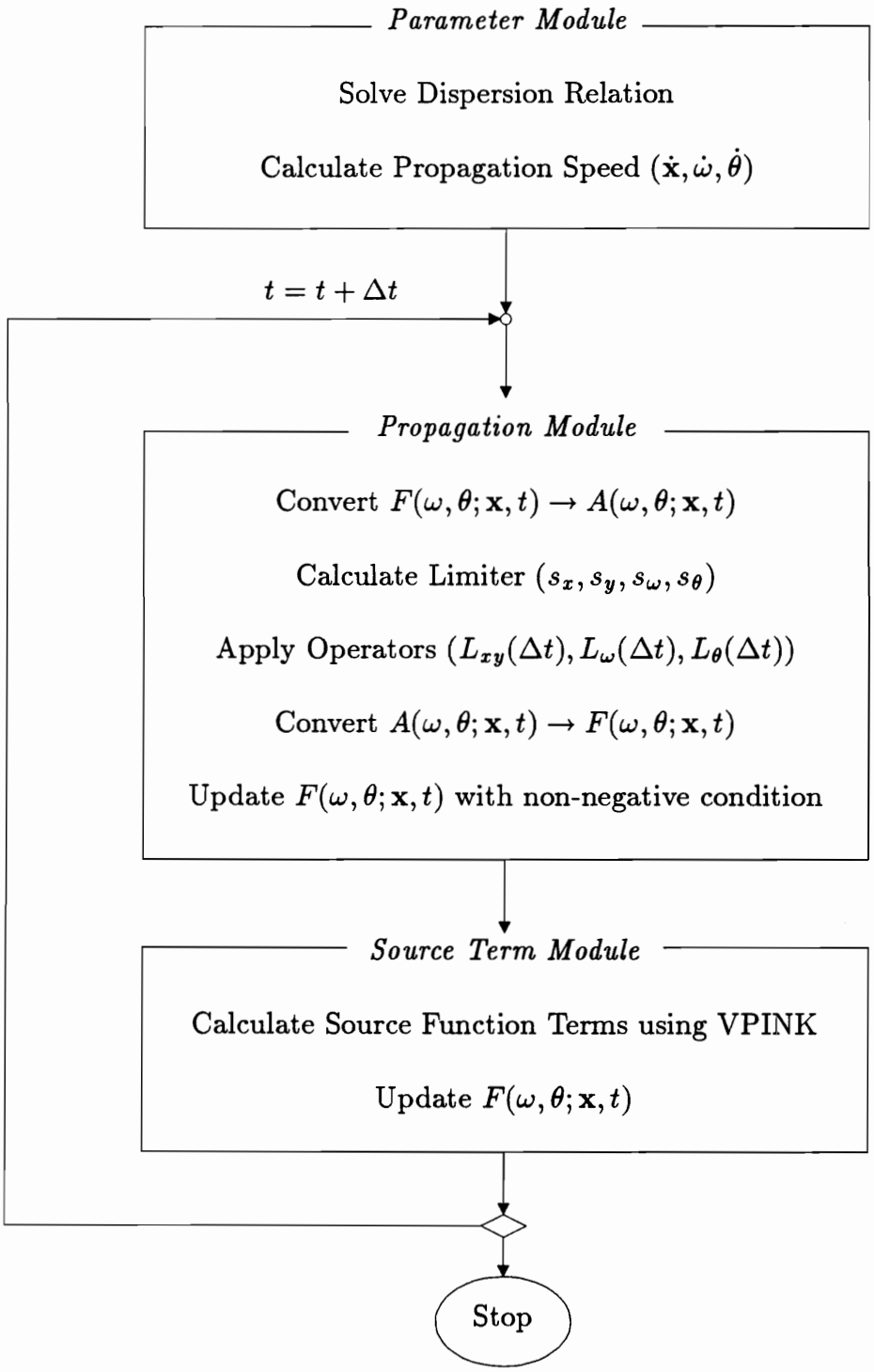

Figure 63. Flow chart of wind wave model

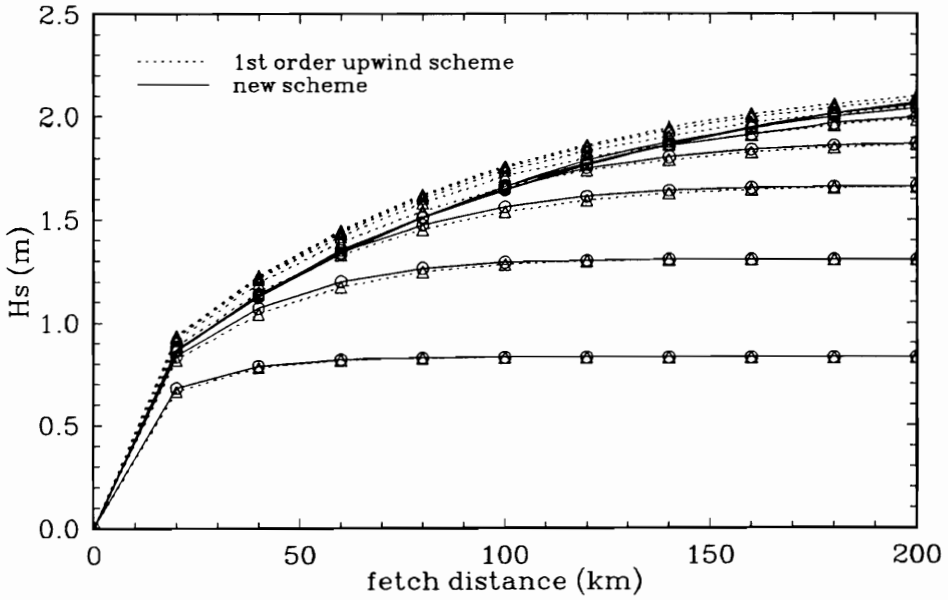

(a) aligned grid

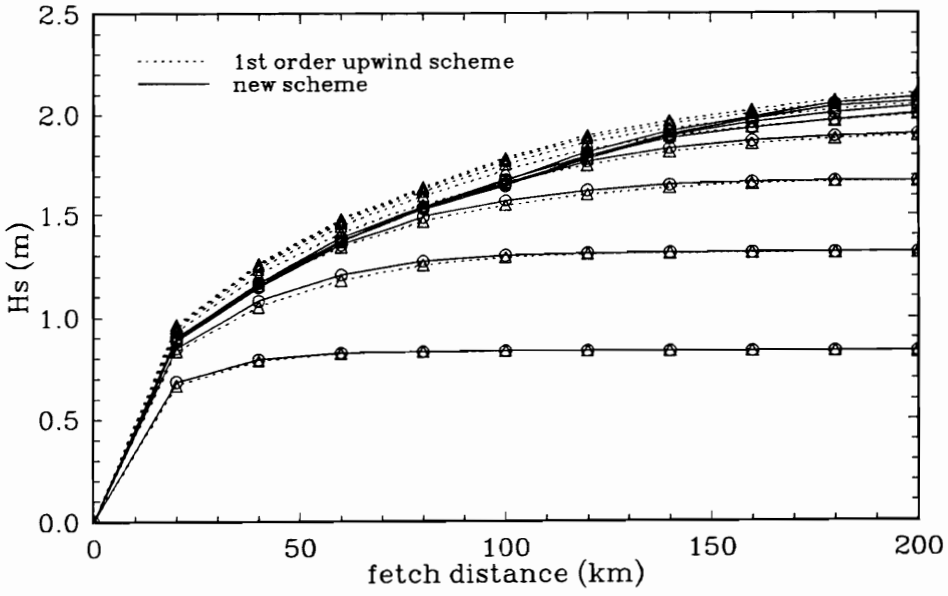

(b) misaligned grid by 15°

Figure 64. One-dimensional fetch limited growth; no refraction

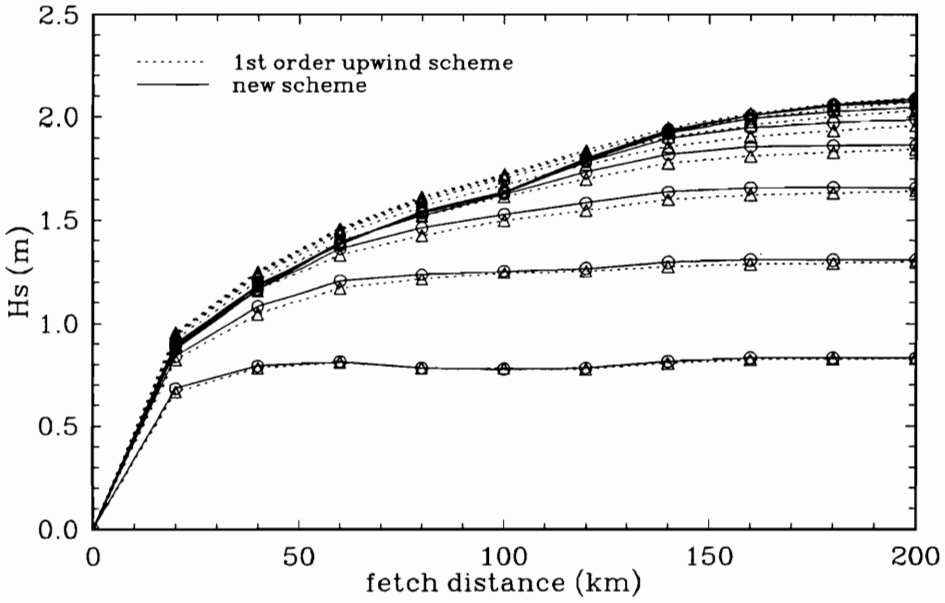

(a) aligned grid

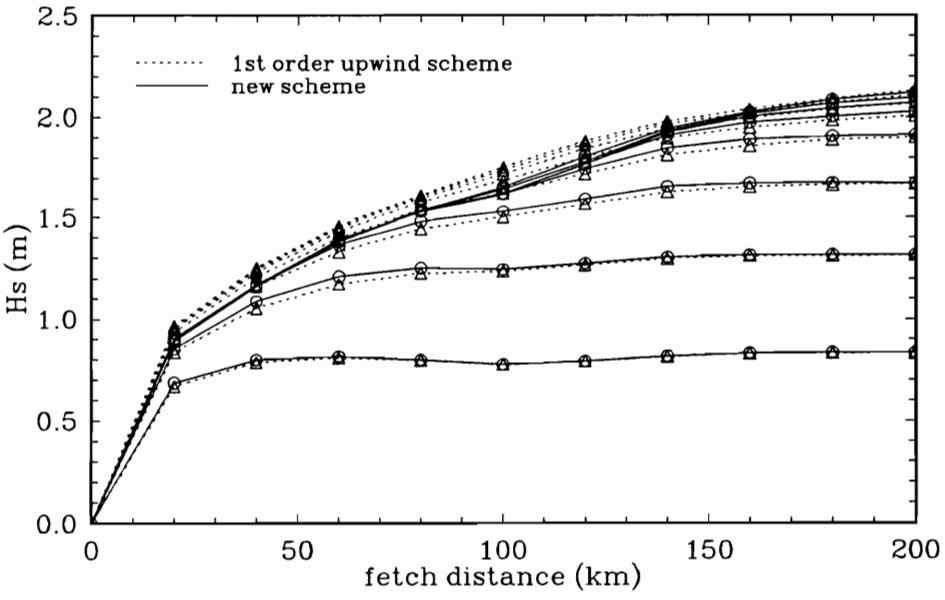

(b) misaligned grid by 15°

Figure 65. One-dimensional fetch limited growth; current refraction

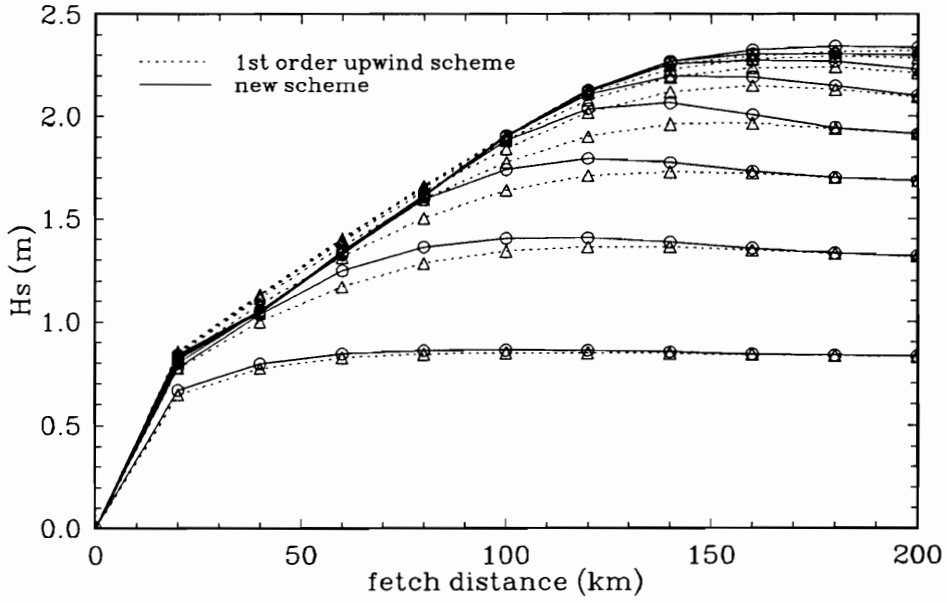

(a) aligned grid

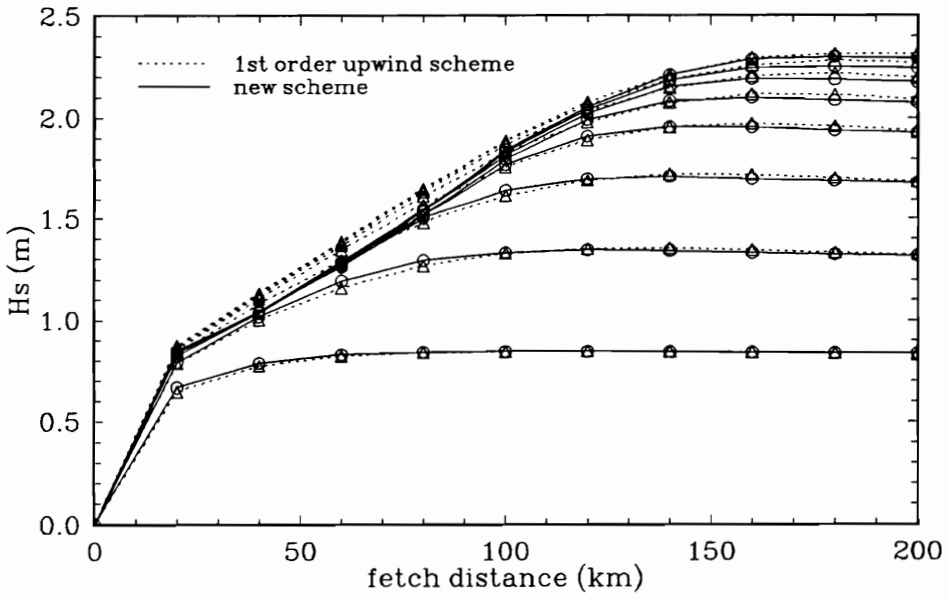

(b) misaligned grid by 15°

Figure 66. One-dimensional fetch limited growth; depth refraction

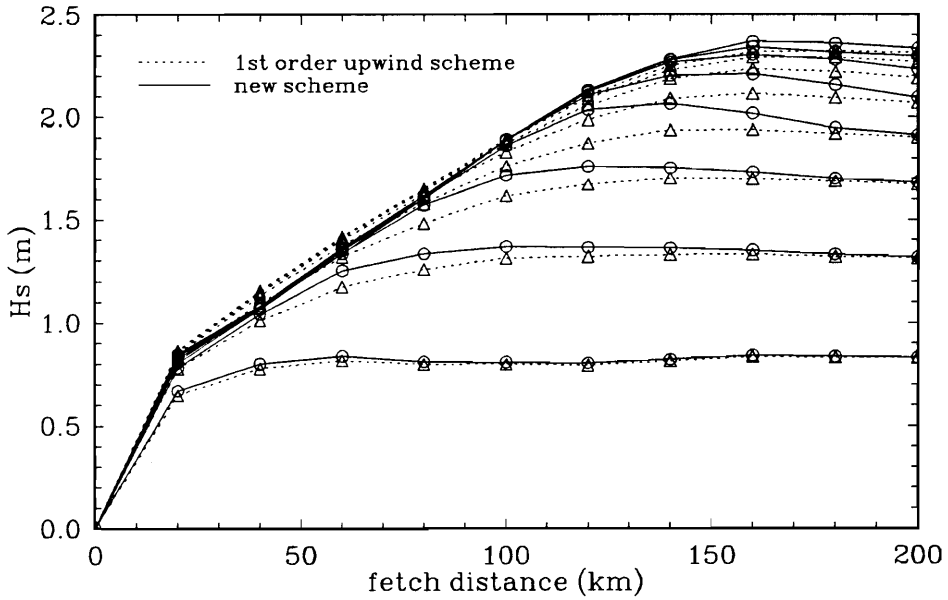

(a) aligned grid

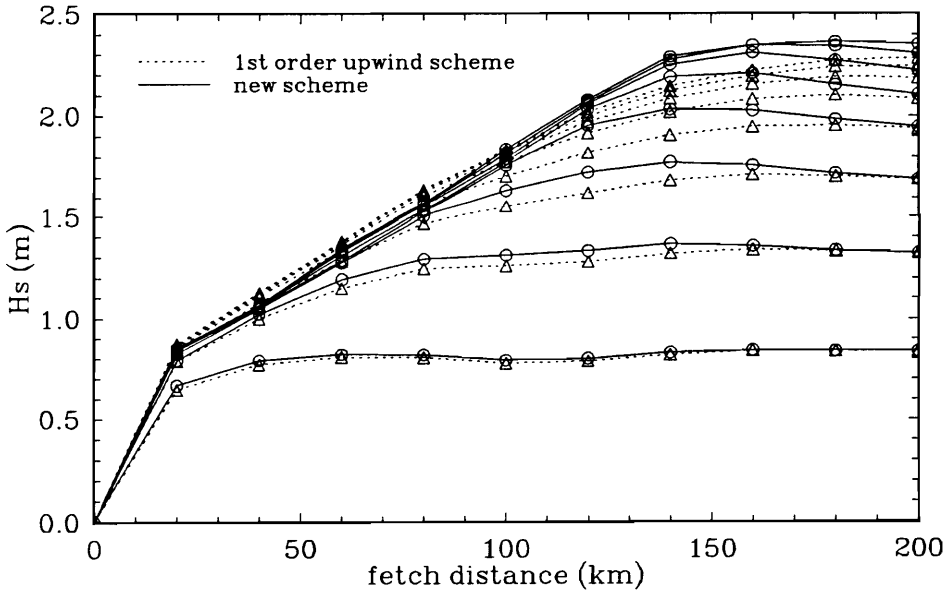

(b) misaligned grid by 15°

Figure 67. One-dimensional fetch limited growth; depth and current refraction

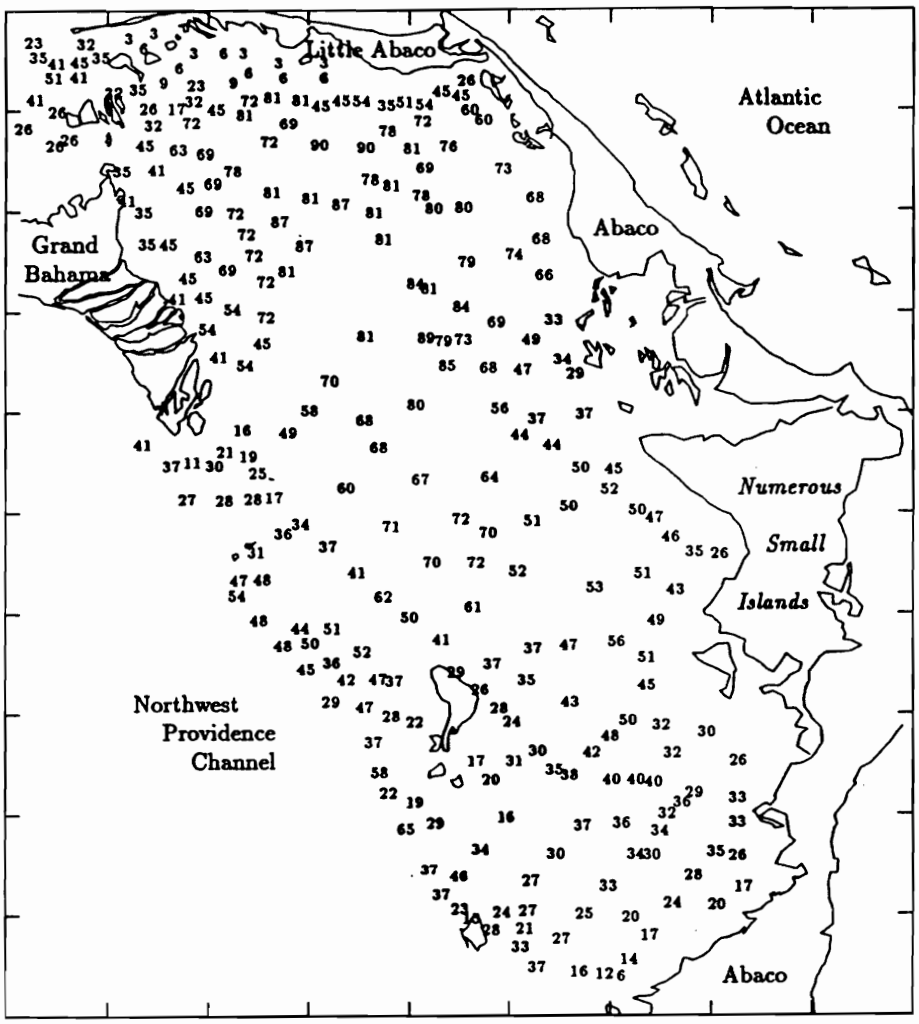

Figure 68. Geometry and bathymetry of the Bight of Abaco

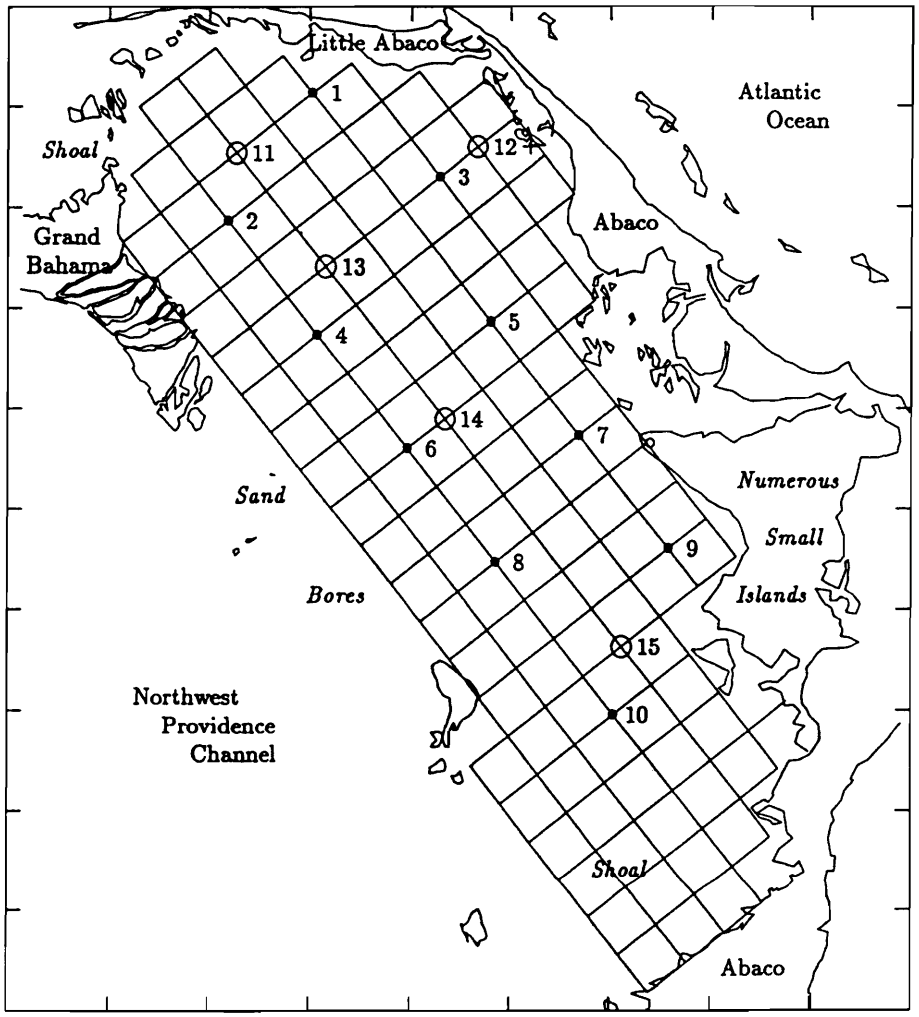

Figure 69. Abaco grid for wind wave model

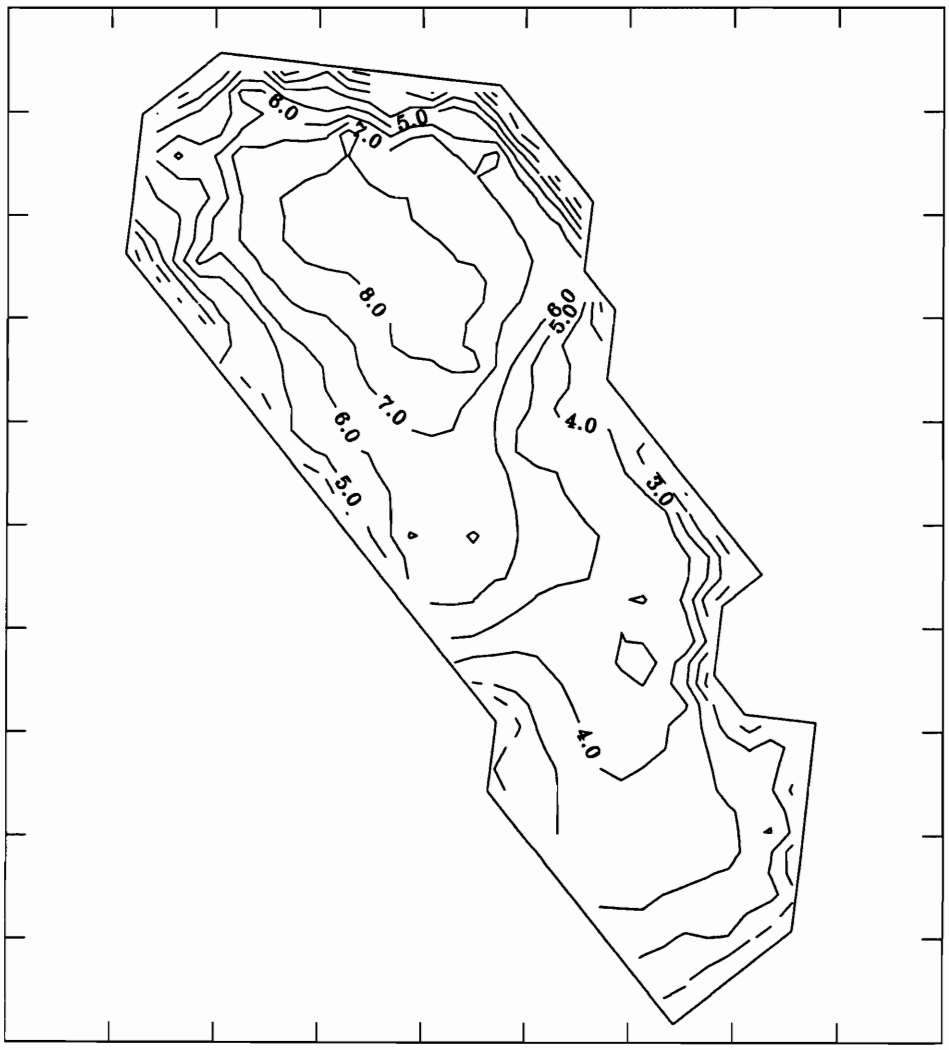

Figure 70. Depth contour map from numerical model (in meter)

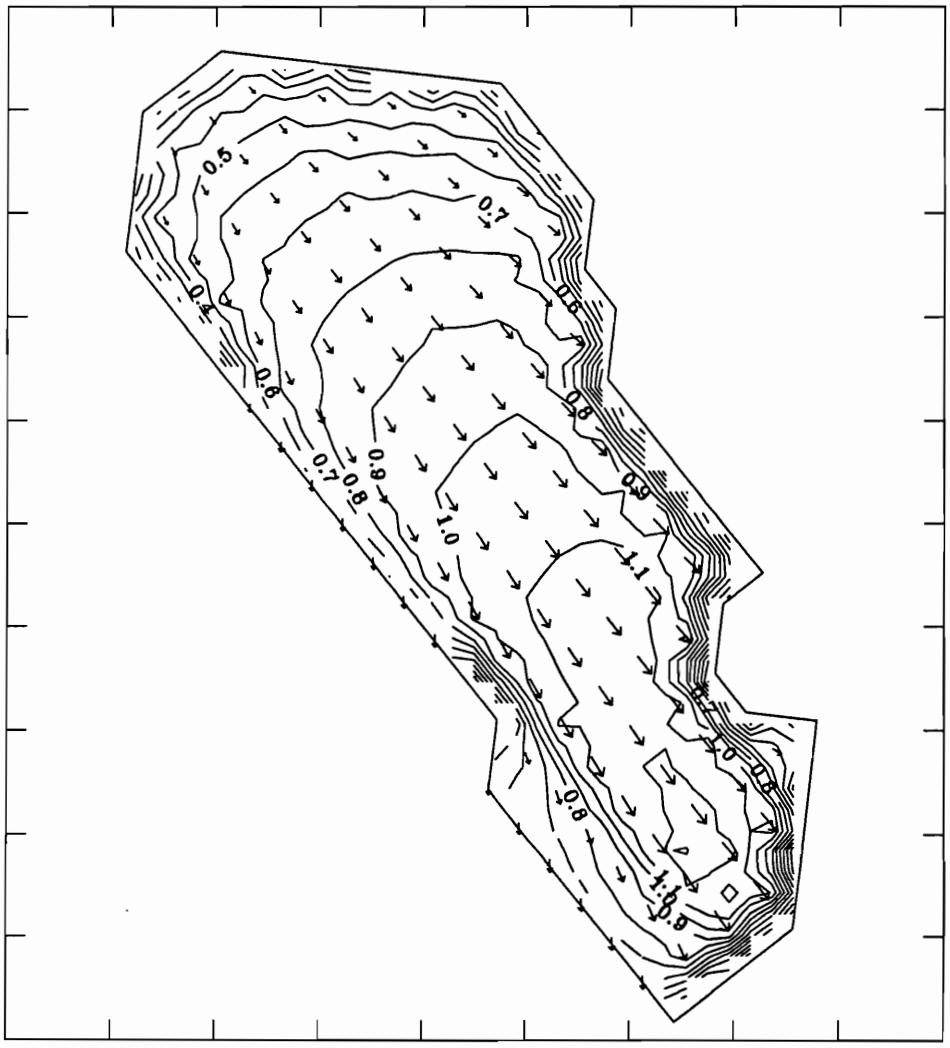

Figure 71. Northwest wind - deep water, 1st upwind scheme, aligned grid

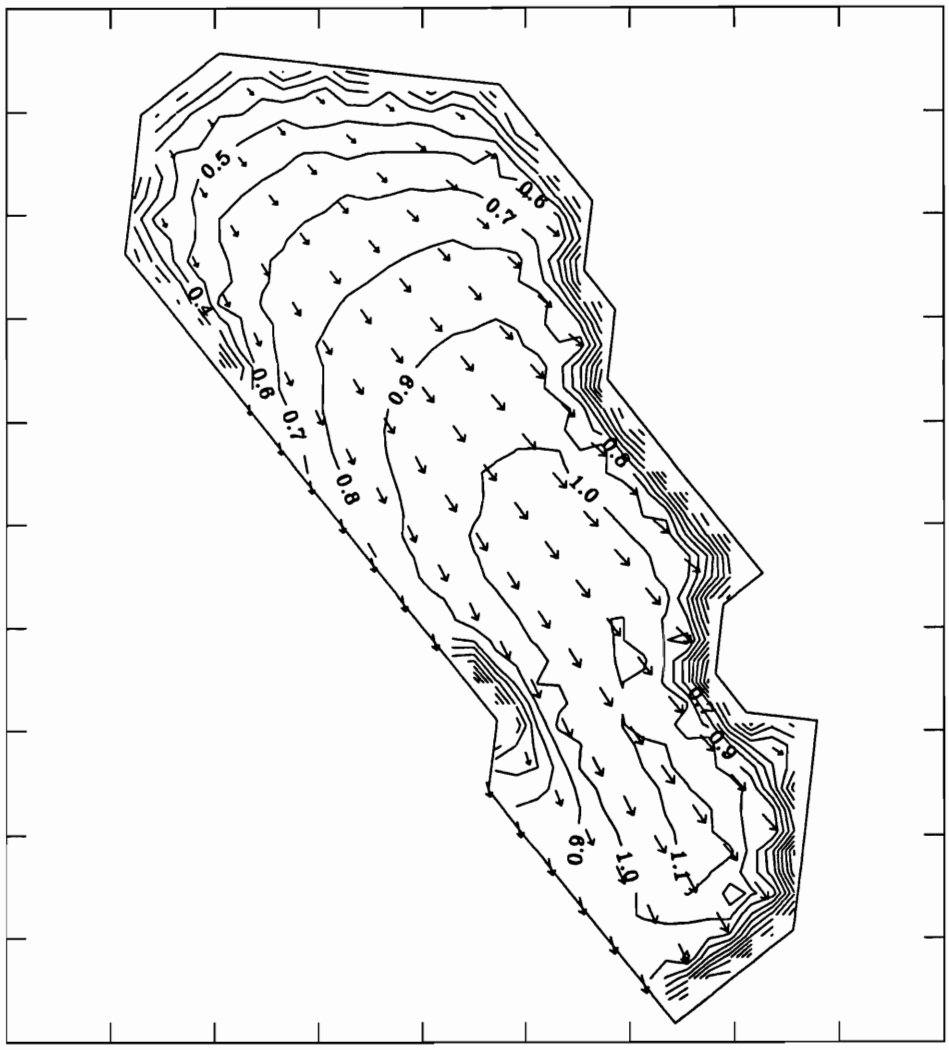

Figure 72. Northwest wind - deep water, 1st upwind scheme, misaligned grid

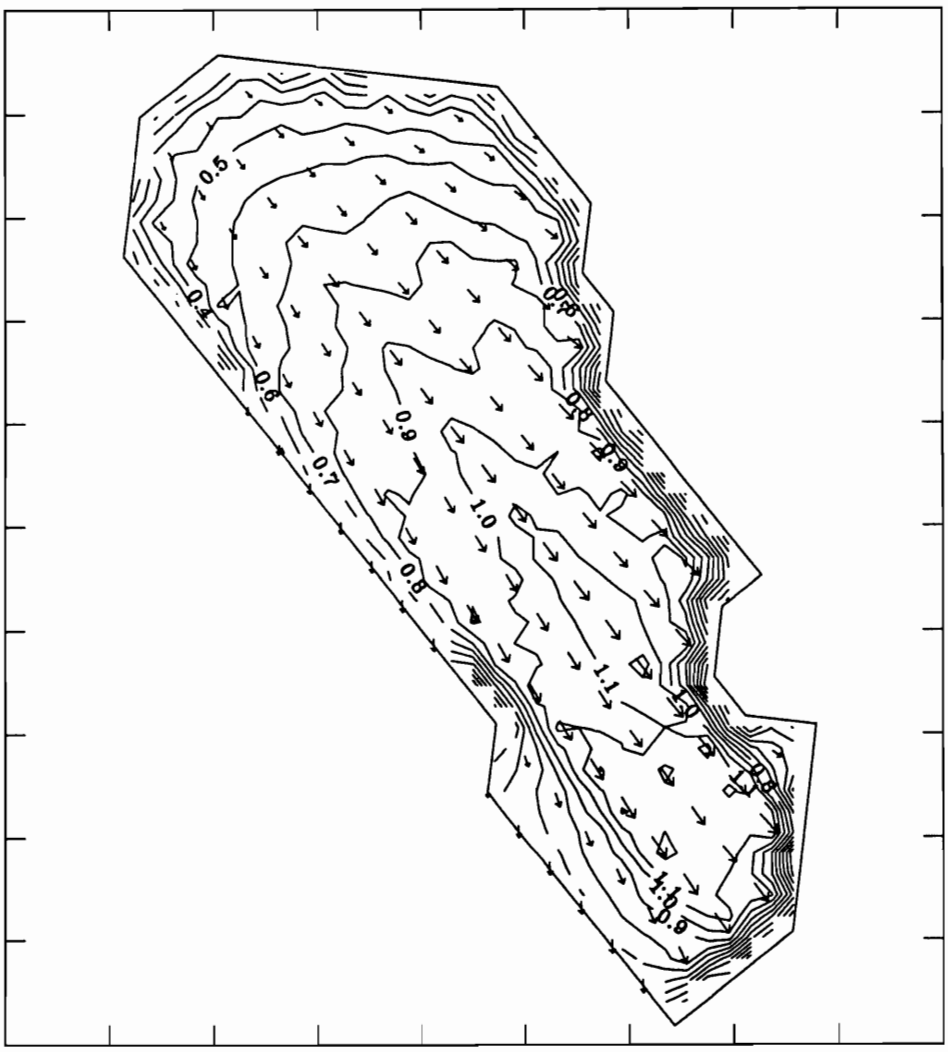

Figure 73. Northwest wind - deep water, new scheme, aligned grid

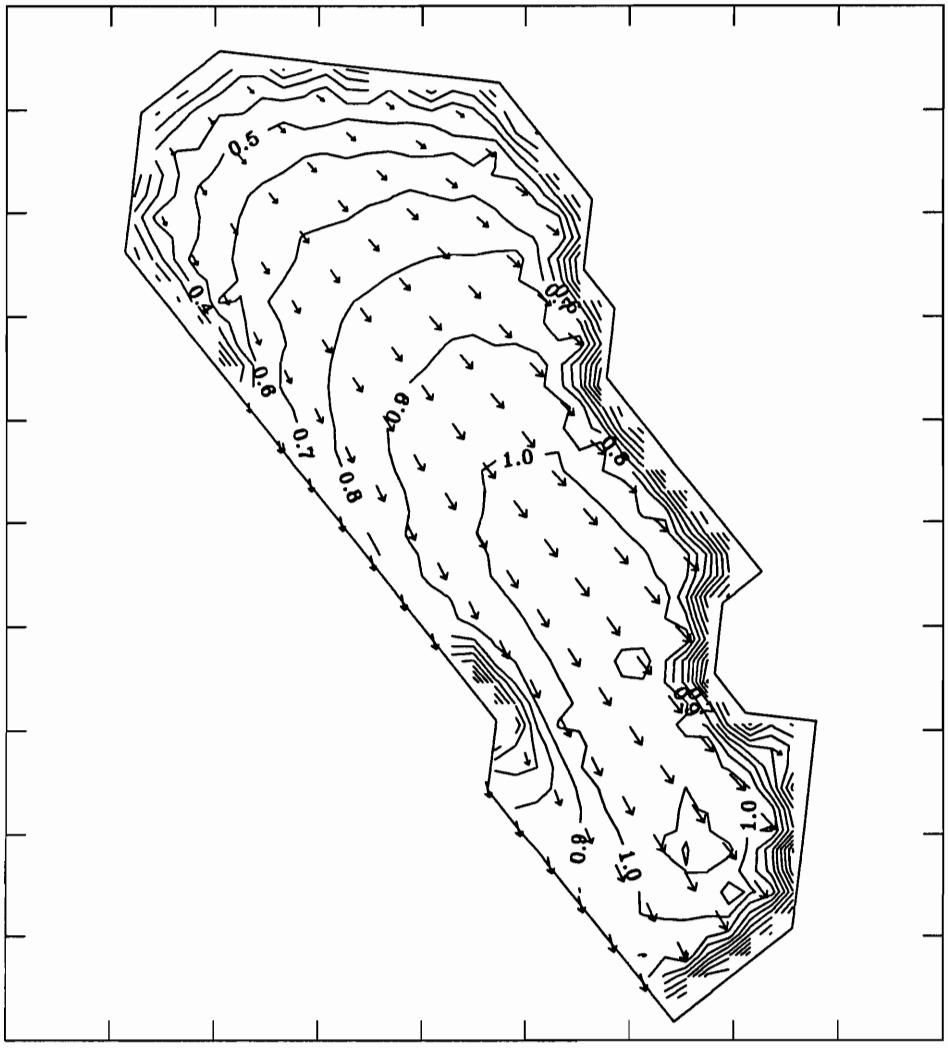

Figure 74. Northwest wind - deep water, new scheme, misaligned grid

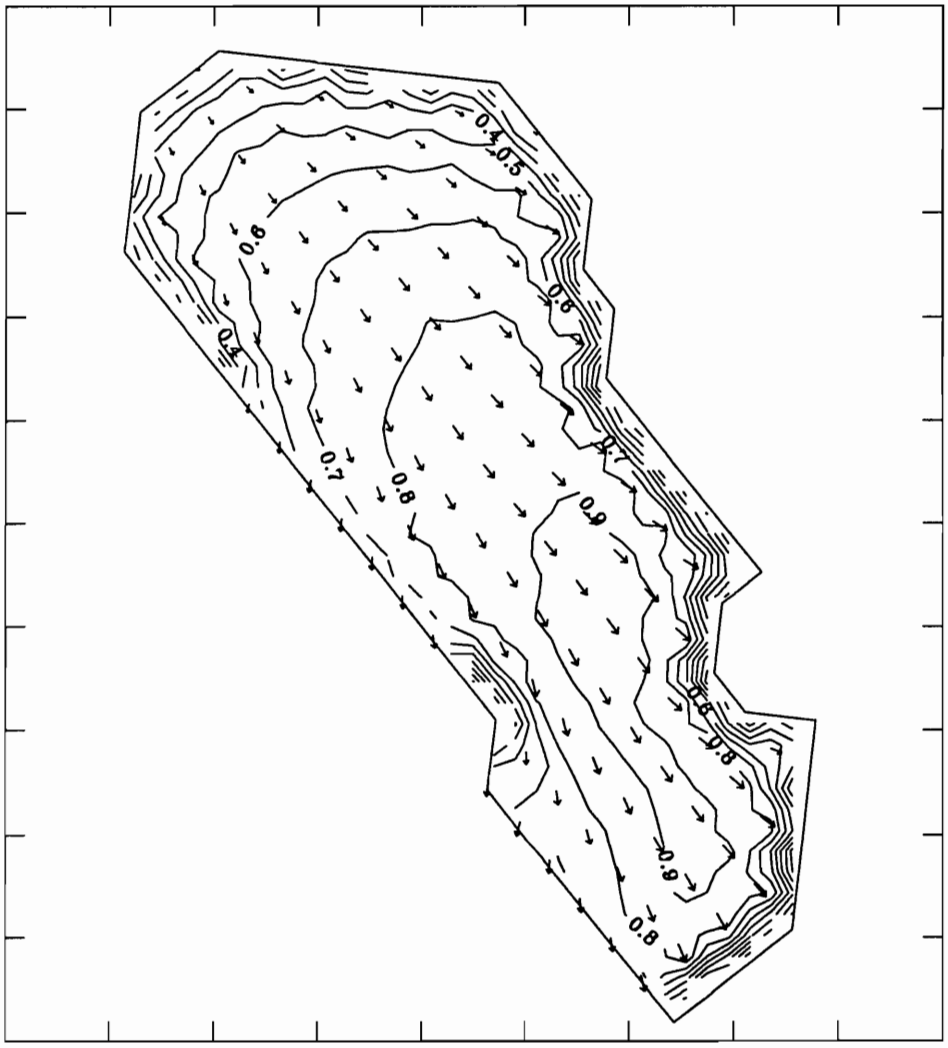

Figure 75. Northwest wind - depth refraction, 1st upwind scheme, misaligned grid

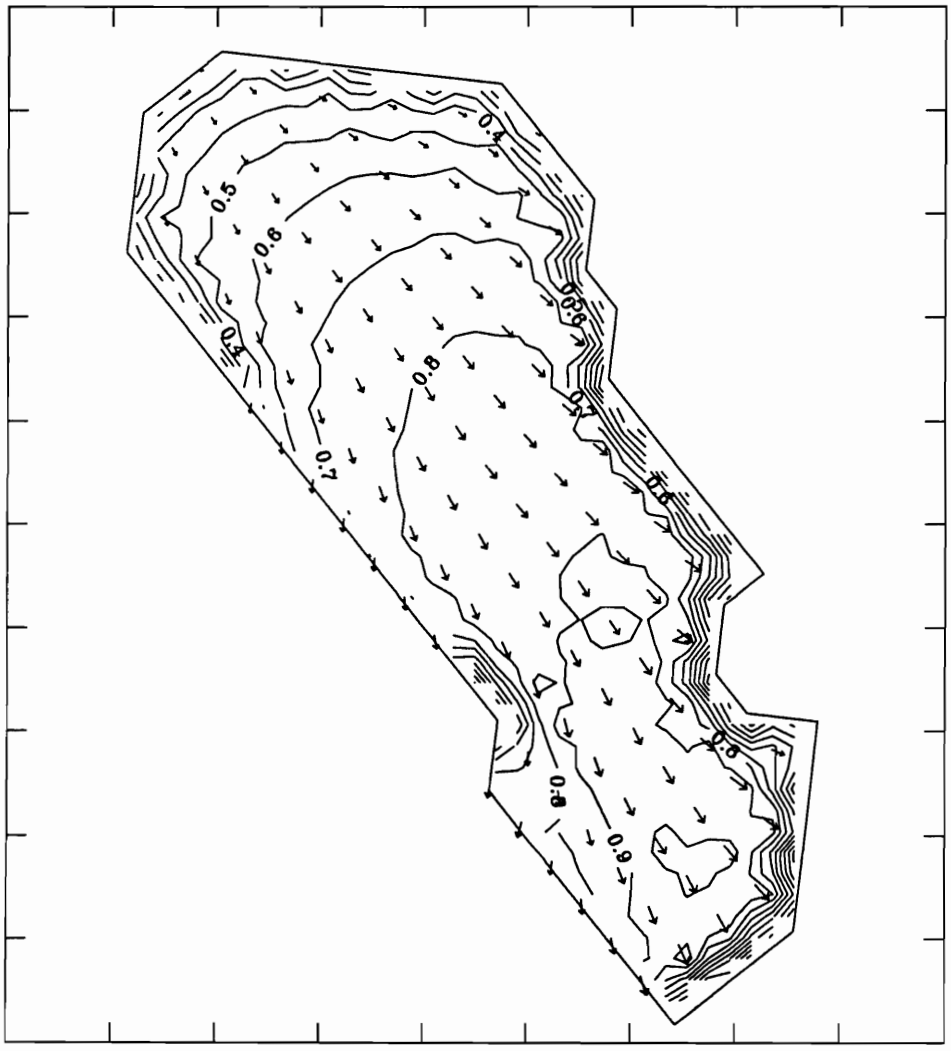

Figure 76. Northwest wind - depth refraction, new scheme, misaligned grid

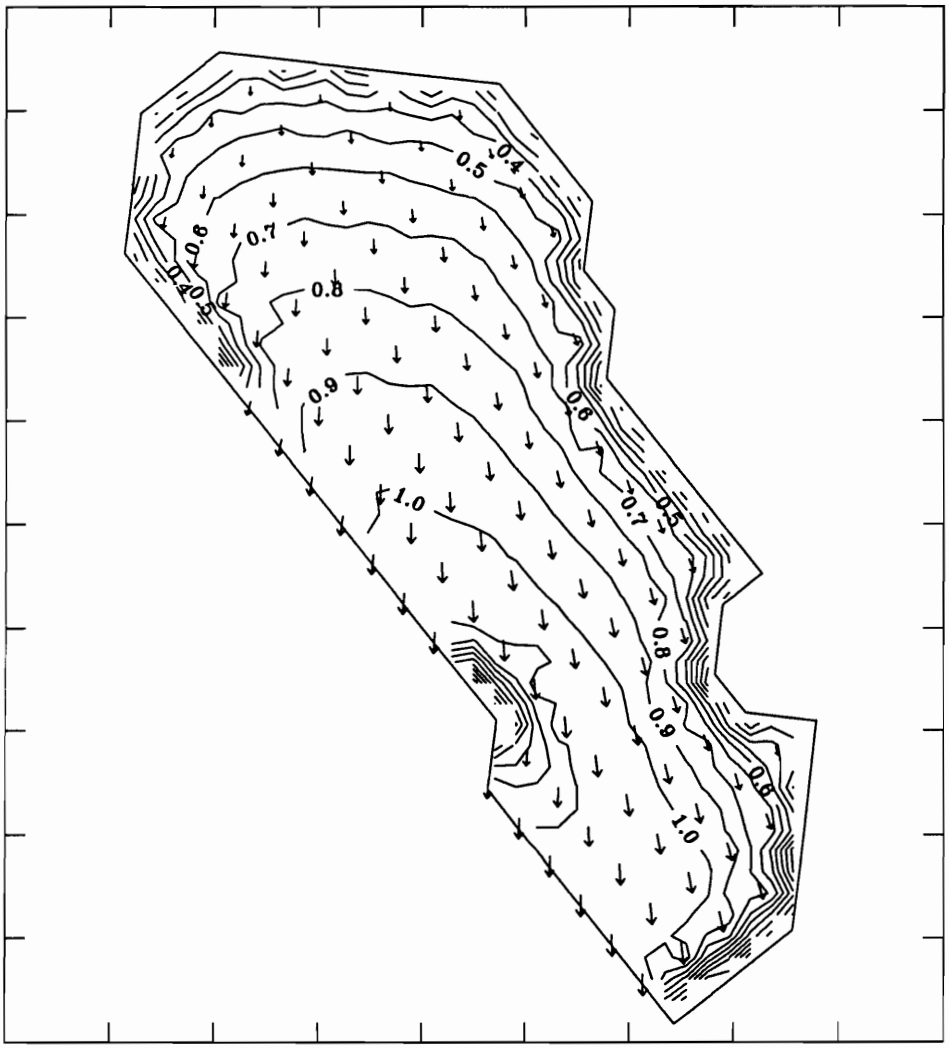

Figure 77. North wind - deep water, 1st upwind scheme, misaligned grid

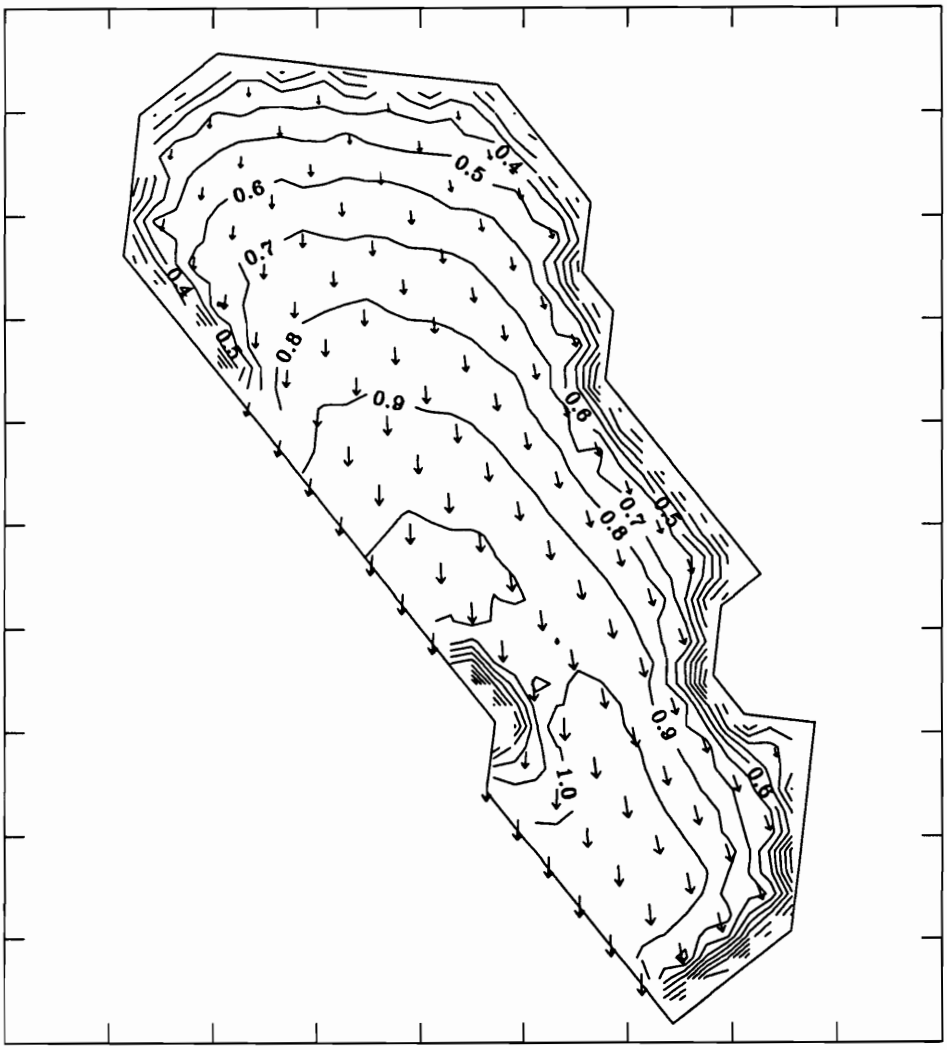

Figure 78. North wind - deep water, new scheme, misaligned grid

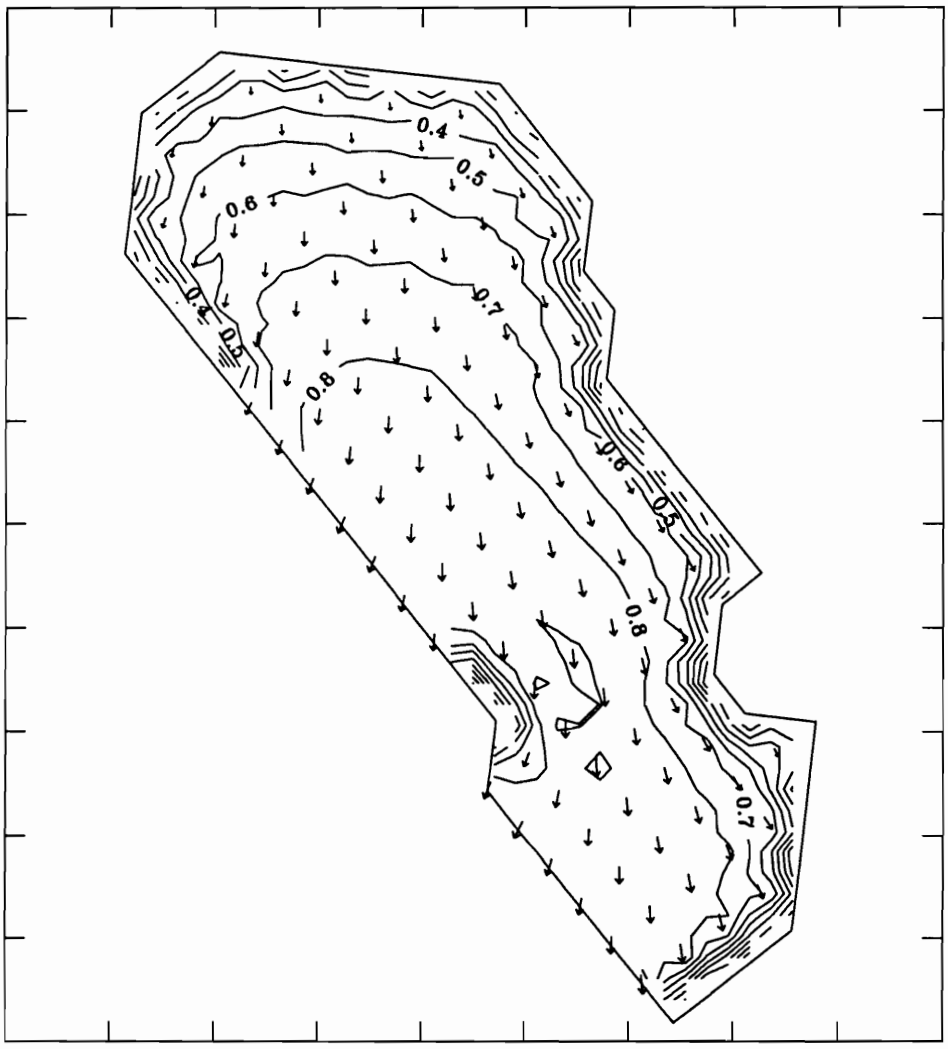

Figure 79. North wind - depth refraction, 1st upwind scheme, misaligned grid

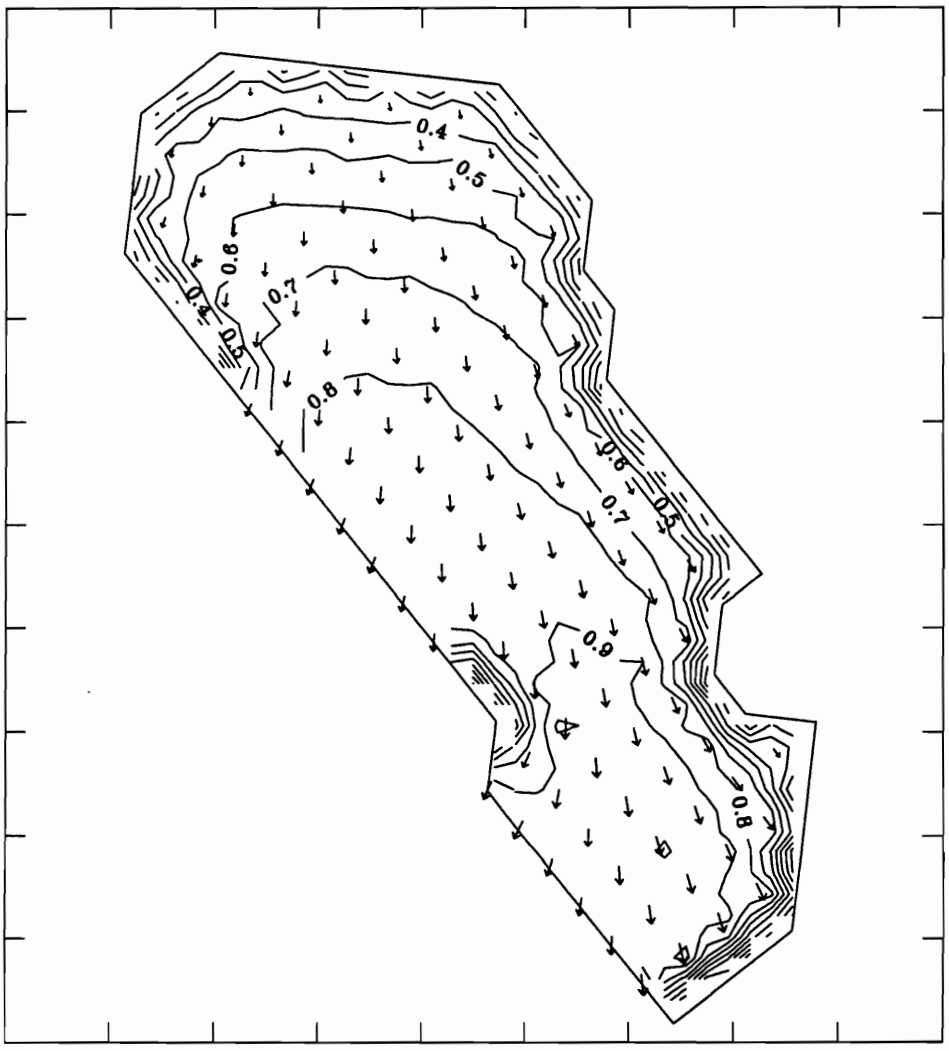

Figure 80. North wind - depth refraction, new scheme, misaligned grid

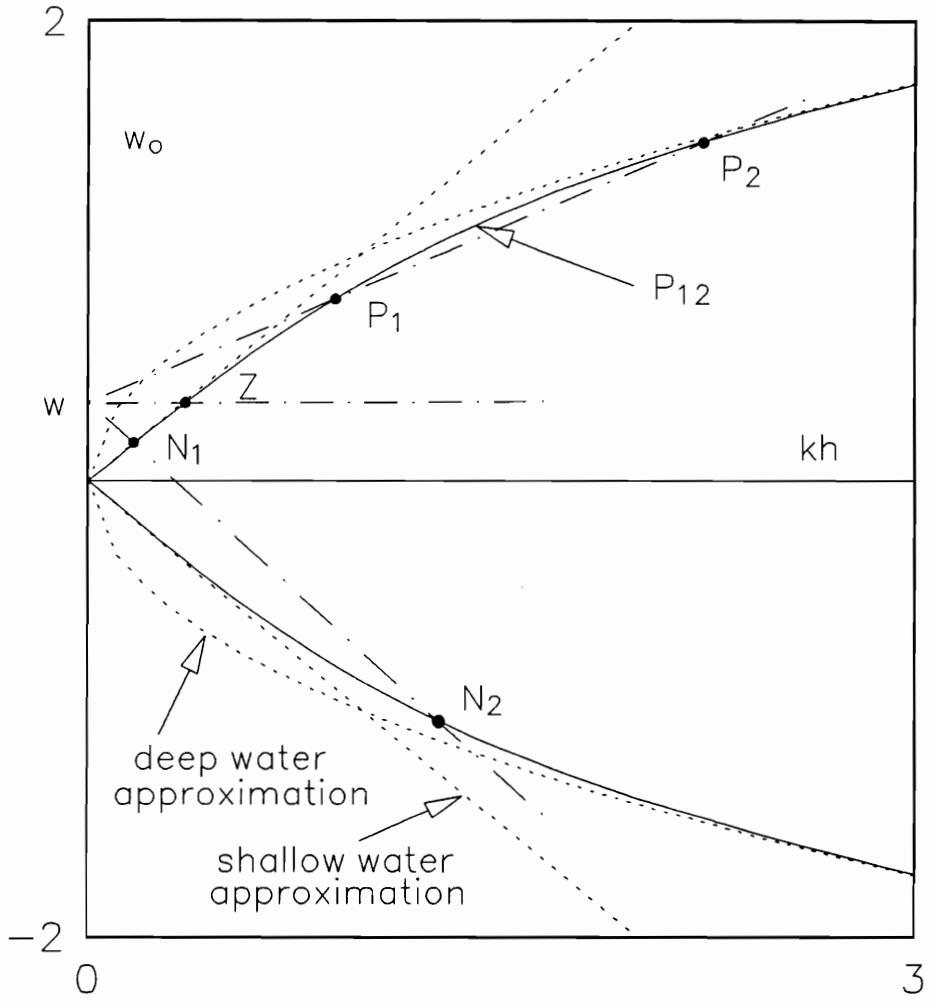

Figure 81. Graphic solution for dispersion relations

VITA

The author was born on October 16, 1957 in Seoul, Korea, where he graduated from the Kyunggi High school and attended the Seoul National University. After receiving his B.S. and M.S. degrees in Naval Architecture in 1980 and 1982, he joined the Hyundai Maritime Research Institute of Hyundai Heavy Industries company in Ulsan, Korea. He has worked as a research engineer for basic design and analyses of offshore structures. In August 1988, he came to America in pursuit of his Ph.D. degree at Virginia Polytechnic Institute and State University.